EVALUATING BONE BY ULTRASOUND

APPROVED BY SUPERVISORY COMMITTEE

Pietro P. Antich, Ph.D. (Mentor)

Liping Tang, Ph.D.

Matthew A. Lewis, Ph.D.

Edmond Richer, Ph.D.

Orhan K. Öz, M.D., Ph.D.

This dissertation is dedicated to my parents,

Ling Huang and Qiao Liu

EVALUATING BONE BY ULTRASOUND

by

Peiying Liu

DISSERTATION

Presented to the Faculty of the Graduate School of Biomedical Sciences

The University of Texas Southwestern Medical Center at Dallas

In Partial Fulfillment of the Requirements

For the Degree of

DOCTOR OF PHILOSOPHY

The University of Texas Southwestern Medical Center at Dallas

Dallas, Texas

May, 2008

Acknowledgments

I would like to express my deepest appreciation to my mentor, Dr. Peter P. Antich, for his great guidance, suggestion, patience and inspiration during the past four years. He introduced me into the field of bone study where my knowledge and interest in diagnostic ultrasound was extended, and has been very helpful in my study and in training me to be an experimentalist. It won't be possible for me to overcome many critical situations and finish this dissertation without his mentorship.

I would like to thank Dr. Matthew A. Lewis and Dr. Edmond Richer for their constant encouragement and guidance throughout my academic years. I've benefited a lot from the numerous discussions with them about my research. I would like to thank Dr. Liping Tang for serving as my committee chair, and thank Dr. Orhan K. Öz for contributing his time and offering valuable advices from the clinic perspective. I would also like to thank Dr. Robert C. Eberhart who has been very generous and encouraging, and always there to listen and advise me throughout my dissertation.

I thank Billy Smith for his help with the electronic devices that I have used, and thank Trung Nguyen for making the complicated phantoms that I have designed. I would also like to extend my sincere thanks to Mrs. Kay Emerson, for her concern, support and help with my life here.

I would like to thank all my friends here at UT Southwestern, especially Yi Guo.

Finally but most importantly, I would like to give my warmest thanks to my parents, Qiao Liu and Ling Huang, for their unconditional love and support all these twenty five years. I deeply appreciate all you have done to me. I dedicate this dissertation to you.

EVALUATING BONE BY ULTRASOUND

Peiying Liu, Ph.D.

The University of Texas Southwestern Medical Center at Dallas, 2008

Supervising Professor: Pietro Paolo Antich, Ph.D.

Bone fractures associated with osteoporosis, a major bone disease characterized by low density and high fracture risk, are common causes of disability and large medical care expenses around the world. Considering its low cost, high portability, and non-ionizing nature, non-invasive ultrasound techniques have been investigated as tools for evaluating bone quality and biomechanical competence. Quantitative ultrasound has been used clinically as a surrogate for the current gold standard measure in osteoporosis diagnosis - Bone Mineral Densitometry (BMD), which unfortunately utilizes ionizing radiation. This study proposes the application of a reflection ultrasound method to evaluate non-BMD properties of cancellous bone, including porosity and the microstructure of the trabecular network, all of

which are directly related to bone morphological changes caused by osteoporosis and could result in better predictions of fracture risk. Computer simulations and phantom studies were adopted to guide the measurement of bone properties. In the computer simulations, the cellular model and the wire model of cancellous bone predict the backscattering dependence on porosity from two different perspectives, but reach the same result. This leads to the first conclusion that reflection ultrasound is not sensitive to the shape of a scatterer of wavelength size but to the spacing between scatterers. The *in vitro* cancellous bone study demonstrated that the average porosity is correlated with the density, while the local porosity depends upon the heterogeneity of the cancellous bone. The average porosity of cancellous bone can be directly determined from ultrasound signals reflected from the bone. Results of the *ex vivo* and *in vivo* short bone studies in patella are in agreement with that of Ultrasound Critical-angle Reflectometry (UCR). Thus, the second conclusion of this dissertation is that reflection ultrasound can be an effective tool for assessing bone properties *in vivo*. During the short bone-mimicking phantom study, the first critical angle detected by UCR was shown to correspond to the solid ultrasound velocity and is independent of porosity, but its amplitude is strongly related to porosity; the second critical angle, corresponding to bulk ultrasound velocity, is strongly related to porosity, but the correlation between its amplitude and the porosity is weak.

TABLE OF CONTENT

LIST OF FIGURES

LIST OF TABLES

Chapter 1 Bone

Bone is an important organ as the human body is built on the skeleton system. It accounts for about 18 % of the total body components. Bone possesses three fundamental functions:

1. Providing mechanical support to the body and attachment site to muscles.
2. Providing protection to bone marrow and some soft organs.
3. Involved in mineral ion and phosphate homeostasis and reservation.

1.1 Bone: structure and biology

Bone is a rigid organ and has a complex structure which is closely related to its major functions of structure support and mineral ion homeostasis. It is fundamentally built up by cells and extracellular matrix. The extracellular matrix is composed of collagen fibers and noncollagenous proteins, with the former one contributing to the degree of elasticity of bone. Other physical properties of bone including the density are subject to change during physiological and pathological status in which the biology of bone changes.

1.1.1 Bone structure

Although bone tissue is rigid calcified tissue, it is not uniformly solid. There are two types of bone based on density, the cortical bone and cancellous bone. Cortical bone is also called compact bone. It is made up by densely packed osteons (Figure 1-1). The osteon is formed by

haversian canal, lamellae, lacunae and canaliculi. Lamellae are the sheets of mineralized collagen fibers which wrap around the central canal. Between the layers of lamellae, there're lacunae and canaliculi, which are the cavities containing bone cells and cell communication channels in the mineralized matrix, respectively. Cancellous bone, also called trabecular or spongy bone, is usually found inside the cortical layer of bones. Cancellous bone can be seen as a two phase material composed of pore walls and fatty marrow within the pores. The network of pore walls is made of the calcified materials of trabeculae and plates, which transfer stress in bones. According to the literature, about 80-90 % in volume of cortical bones are calcified, while only 15-25 % of the cancellous bones are calcified (Baron 2003).

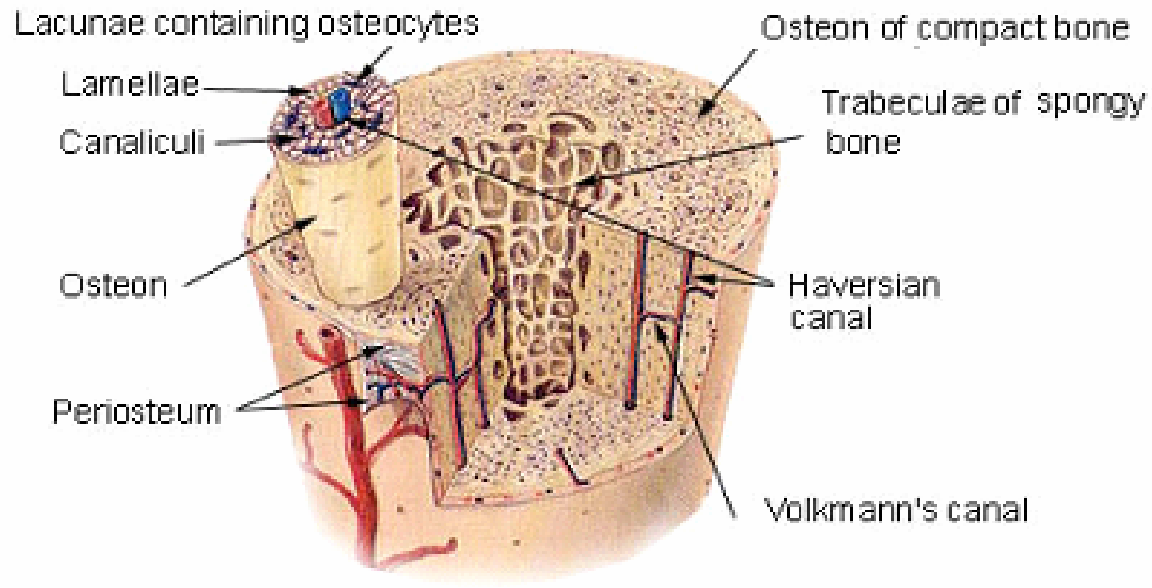

Figure 1-1 Illustration of Bone structure. (Adapted from http://en.wikipedia.org/wiki/Bone)

Bones in the human body can be divided into four types by shape: long bones, short bones, flat bones and irregular bones. Long bones have a long shaft called diaphysis and two articular surfaces called epiphyses. Femur and tibia of the leg, humerus and ulna of the arm, as well as radius, metacarpals and phalanges of the hand and foot, are all long bones. Short bones have a thin layer of compact bone outside of the spongy interior and are cube-shape alike. The wrist bones such as scaphoid, lunate, triquetral and pisiform, and the ankle (tarsal) bones such as calcaneus and talus, as well as the sesamoid bones such as patella, are all of this kind. Flat bones have two parallel layers of cortical bone and a layer of cancellous bone between them. They are thin and usually curved. The sternum and most skull bones are flat bones. Irregular bones, as indicated by its name, are irregular-shaped. Similar to short bones, they also have thin layers of cortical bone surrounding a spongy interior. The vertebra and sacrum are irregular bones.

1.1.2 Bone physiology

A. Bone Cells

There are three types of bone cells, which are osteoblast, osteoclast and osteocyte. These cells are embedded in the mineralized connective tissue sheets, i.e., matrix, which makes up the osseous tissue. Bone cells that form the matrix are called osteoblasts. As the development goes on, they get trapped within lacunae and are called osteocytes. Bone cells that resorb the matrix are called osteoclasts.

B. Bone formation

Bone development can proceed in at least two distinct ways, which are intramembranous

ossification and endochondral ossification. Most of the bones of the skeleton, include the long bones, short bones, and irregular bones, are formed in manner of endochondral ossification, while flat bones always undergoes intramembranous ossification.

At the beginning of intramembranous osteogenesis, collagen fibers and ground substance form in sheets at sites where flat bones will eventually be. These connective tissue sheets are highly invested with blood vessels. Some of the local mesenchymal stem cell (bone marrow stromal stem cell or connective tissue mesenchymal stem cell) in the collagen sheets differentiate into osteoblasts. These osteoblasts begin lining the layers of bone extracellular matrix, forming cancellous bone. As time goes on, more and more osteoblasts form from the connective tissue sheets. Instead of entering the existing cancellous bone, the newer differentiated osteoblasts begin to accumulate on the edges of the cancellous bone, where they lay down harder matrix, as cortical bone. Then, they get trapped within this matrix and are become either flat lining cell or osteocytes.

For endochondral ossification which occurs in most of the bones of the skeleton including the long, short and irregular bones, bone forms by replacing hyaline cartilage. The growth plate of long bone includes different cartilage zones in the order of development. Close to the epiphysis is the reserve zone, which is an area of typical juvenile hyaline cartilage. Moving towards the diaphyseal region is the proliferation zone, which is a zone of active cellular division, resulting in an increase in the number of chondrocytes and growth of the cartilaginous model. Moving further into the developing diaphyseal region is zone of maturations where mitotic division no longer occurs. The next zone is the hypertrophy zone. The early part of this area undergoes calcification, with a gradual deposition of mineral salts

into the intercellular cartilage matrix which make it harder. The chondrocytes near the region of active ossification have enlarged (hypertrophied) and lined up more or less in columns. Finally it is the zone of ossification or osteogenesis. The chondrocytes degenerate and die, while the calcified cartilaginous matrix is invaded by osteogenic cells and capillaries from the bone marrow cavity. Osteogenic cells gather on calcified spicules of cartilaginous matrix and begin to deposit bone matrix. Osteoblasts are then recruited to form trabecular bone that is subsequently remodeled by osteoclasts and maintained by the opposite but coordinated activities of bone-forming osteoblasts and bone-resorbing osteoblasts.

C. Bone resorption

Bone resorption is carried out by osteoclasts, the other type of bone lining cells. Osteoclast is a giant multinucleated cell derived from hemopoietic stem cells of the bone marrow. It is usually found in contact with the calcified bone surface.

Osteoclast secrets protons through the proton-pump on its ruffled-border membrane, resulting in an acid environment to the extracellular matrix. With the low pH environment and essential lysosomal enzymes synthesized by the osteoclast, the collagen fibers are then digested and the matrix is degraded. The calcium deposited in the matrix is also released during this process.

D. Remodeling dynamics

The bones of adult skeleton is in a dynamic state, where it is continuously broken down by osteoclast and remodeled by osteoblast on trabecular surface of cancellous bone or Haversian systems of cortical bone. The process of bone growth and turnover together is called bone remodeling. For bones of normal adults, bone formation occurs only at the place where bone

resorption has previously occurred. A complete remodeling cycle contains the activation-resorption-formation processes occurring consequently, and takes about 3 – 6 months at each microscopic site.

In physical and most pathological circumstances, there's a coupling of bone resorption and bone formation in the same remodeling cycle, which means the amount of bone being removed when bone resorption are faithfully recreated during bone formation (Mundy, Chen et al. 2003). However, because of aging, hormonal changes and other factors, the coupling could fail and bone loss occurs as the packets of bone being broken down by resorption can no longer be fully replaced by formation. According to literatures (Mundy, Chen et al. 2003), cortical bone loss probably begins to take place after the age of 40. For women, this loss accelerates for 5 to 10 years after menopause (Lindsay 1988), due to the sudden drop of estrogen level after ovarian function ceases (Riggs, Khosla et al. 1998).

Since cancellous bone composes of over 66 % of human lumbar spine, it is the cancellous bone loss that largely determines the risk of spinal osteoporotic fracture. However, the start point of cancellous bone loss is quite controversial. Some studies suggested that the decline of cancellous bone mass occurs earlier than that of cortical bone mass, beginning in early adult life around the age of 30, while some studies suggested that for women the cancellous bone loss begins after ovarian function ceases (Mundy, Chen et al. 2003).

1.1.3 Bone diseases

All bone diseases are caused by the abnormal of the remodeling process. In diseases such as hyperostosis, there is an excessive or abnormal thickening or growth of bone tissue. On the

other hand, excessive bone loss and abnormal calcium deposit are responsible for diseases including osteoporosis, osteromalacia and Paget's disease.

Osteoporosis is a systemic bone disease characterized by low bone density and disrupted bone microarchitecture, resulting in increased fragility and susceptibility to fracture (Cooper 2003). It is the most common bone disease. The United states Department of Health and Human Service has reported in 2004 that 10 million Americans over the age of 50 have osteoporosis, while another 34 million are at risk for developing osteoporosis. And each year, about 1.5 million people suffer from osteoporosis related bone fracture. The government report also predicted that "by 2020, one in two Americans over age 50 will be at risk for fractures from osteoporosis or low bone mass" due primarily to the aging of the population and the previous lack of focus on bone health; and the projected number of hip fractures in the United States could double or even triple by 2020 (2004). Therefore, diagnosing osteoporosis and predicting the risk of bone fracture become extremely important.

Measurement of bone mineral density (BMD) by bone densitometry is currently the gold standard for the diagnosis of osteoporosis. "The relationship between BMD and fracture is stronger than the relationship between cholesterol and heart attack, and as strong as the relationship between blood pressure and stroke" (Marshall, Johnell et al. 1996; 2004). BMD is commonly measured using single-energy X-ray absorptiometry (SEXA) and dual-energy X-ray absorptiometry (DEXA). Dual energy is used to remove soft tissue contributions to attenuation.

The World Health Organization (WHO) provided a simple stratified definition of osteoporosis in 1994, as summarized in table 1-1.

Table 1-1 Diagnostic criteria for osteoporosis from WHO (1994).

Category	Definition by bone density
Normal	A value of BMD that is no more than 1 SD below peak bone mass*
Osteopenia	A value of BMD that is between 1 and 2.5 SD below peak bone mass
Osteoporosis	A value of BMD that is more than 2.5 SD below peak bone mass
Severe osteoporosis (established)	A value of BMD that is more than 2.5 SD below peak bone mass with the presence of fragility fracture

*: Peak bone mass: 20-year-old sex-matched healthy person average.

There're two forms of osteoporosis, the primary and secondary forms. Primary osteoporosis is seen mostly in postmenopausal women and aging man, and accounts for 80 – 90 % of cases. Studies have showed that estrogen deficiency causes primary osteoporosis in postmenopausal women and contributes to bone loss in aging man (Riggs, Khosla et al. 1998). Secondary osteoporosis results from or occurs in association with a variety of identifiable conditions, such as hormonal imbalances (e.g., glucocorticoid excess), endocrine diseases (e.g., diabetes mellitus), medications (e.g., corticosteroids), drugs (e.g., ethanol, tobacco and heparin) and miscellaneous conditions (e.g., chronic renal failure and liver disease).

Besides of the increasing incidence of osteoporosis in elder people, pediatric osteoporosis is also an emerging problem in many countries (Brown 2003). Its causes include the inherited conditions from birth or early infancy, environmental influences, inadequate mineralization and abnormal bone remodeling processes during the rapid skeletal growth and maturation in puberty (Magarey, Boulton et al. 1999; Norman 2003).

1.2 Bone quality and biomechanics

As indicated before, bone plays an important role in the human body. Among its three fundamental functions, the first two are biomechanical roles of the bone, which are support and protection. Therefore bone must be rigid to resist deformation, and also have some degree of elasticity to absorb energy by deforming. For example, the ends of long bones are broadened to reduce stress at the joints. Cancellous bones in the sandwich-like structure of flat bones and short bones help diminishing pressure from side to side to protect the soft tissues. The quality of bone affects the biomechanical performance of the skeleton.

1.2.1 Bone quality

Bone quality is also called bone strength, which is determined by its material composition and structural design (Seeman and Delmas 2006). Bone mineral density (BMD), measured by X-ray absorptiometry in clinic, is the most widely used predictor of bone quality. Bone density or porosity is also used to indicate the bone strength.

In addition to density and porosity, there are other qualitative factors, such as elasticity, fatigue damage, and trabecular microarchitecture. They all contribute to bone strength. These

factors could be used to explain the failure of BV/TV for some individuals to precisely predict bone strength (Fyhrie 2005).

1.2.2 Bone material properties

The elasticity of bone can be learned from the stress-strain curve obtained by *ex vivo* mechanical measurement. By definition, stress is the load per unit area and strain is the fractional change in length under stress. Based on the stress-strain curve, materials can be characterized as weak and strong, stiff or compliant, elastic or rigid.

When the stress is small, bone can recover to its original shape and length after the stress is removed; this stress region is called elastic region on the curve. Young's modulus (E), the measurement of stiffness of the material, is defined by the slope of elastic region. The area under the stress-strain curve indicates the amount of energy the bone tissue can strand before break, called the modulus of toughness. The tougher a bone is, the more it is resistant to fracture. The degree of mineralization greatly affects the material properties of bone. Bones with higher degree of mineralization have smaller elasticity (Young's modulus) (Burr and Turner 2003).

Anisotropy is an important structural property of cancellous bone. As shown in figure 1-4, the trabecular network of cancellous appears totally differently on the three orthogonal planes, and so does the pore shape. The degree of anisotropy defines the variations of trabecular orientation, and is related to the biomechanic performance and fracture pattern of the trabecular bone. This parameter makes the model and measurement of cancellous bone difficult.

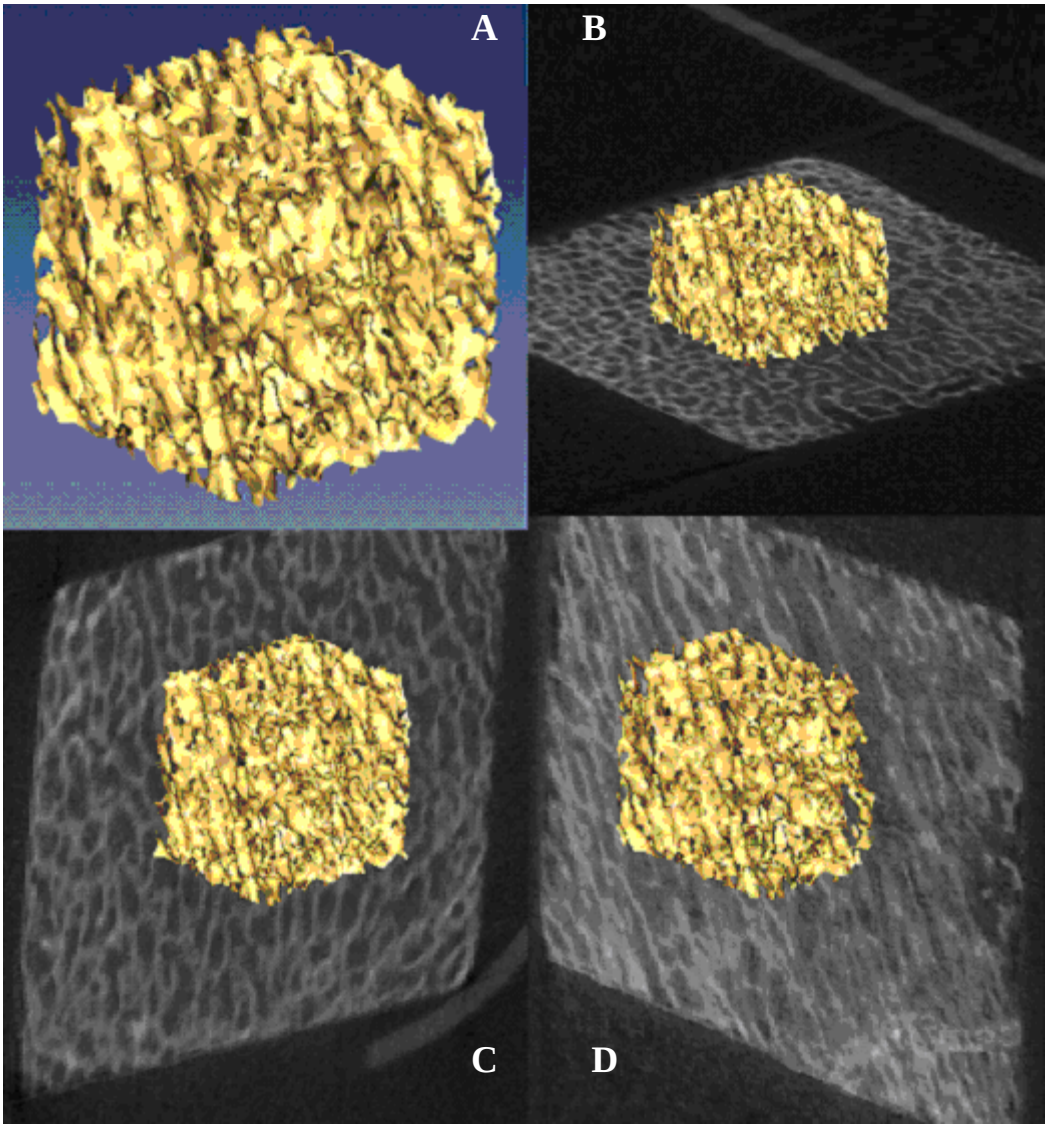

Figure 1-2 MicroCT images of cancellous bone sample showing the anisotropy of trabeculae orientation and distribution. A) 3-D image of the cancellous bone sample. The sagittal (C), axial (C) and coronal (D) slice views of the sample clearly show the anisotropy of the trabeculae network.

Another parameter used to describe the geometrical property of bone and other porous media is tortuosity. Originally, tortuosity is used to describe the property of a curve being tortuous (marked by repeated twists, bends, or turns), and the most simple mathematic evaluation of tortuosity is given by calculating the ratio of the length of the curve (L) to the distance between the ends of it (C), which also called the arc-chord ratio:

$$\tau = \frac{L}{C}$$

In acoustics (Zwikker and Kosten 1949; Attenborough 1982; Fellah, Berger et al. 2003; Roh and Yoon 2004), tortuosity is indicated as a geometrical parameter that describes sound propagation in fluid-saturated porous materials following initial works by Biot in 1956 (Biot 1956; Biot 1956). It is said to interpret the interaction between the fluid filled in the pores and the structure of the porous material in high frequency range (Fellah, Berger et al. 2003). In such kind of media, the viscous effect can be ignored when the sound wave frequency is high enough, and therefore the velocity of sound propagation in the fluid in the pores is non-dispersive. Compared with that in the free fluid, the value of the velocity of sound in this case is reduced by a ratio equal to the square root of the tortuosity. This relationship has been used for some applications including the study of materials for acoustic isolation. But this parameter won't be discussed here; instead, this dissertation is mainly focusing on cancellous bone porosity.

Chapter 2 Ultrasound

2.1 Basics of Ultrasound

Ultrasound is a longitude wave whose frequency is beyond the audible range, and has been used in medical purpose since 1950s. Based on its application, there are two types of ultrasound being studied: diagnostic ultrasound and therapeutic ultrasound. As indicated by its name, diagnostic ultrasound is used to detect disease and assess treatment, while therapeutic ultrasound is used to cure. As an example of therapeutic ultrasound, high-intensity focused ultrasound (HIFU) as a noninvasive method has been utilized to treat tumors (Chapelon, Ribault et al. 1999) and to stop internal bleeding (hemostasis) (Vaezy, Andrew et al. 2001). Ultrasound devices have also been used to induce thrombolysis (Rosenschein, Furman et al. 2000) and lithotripsy (Haupt and Haupt 2003).

Basically, diagnostic ultrasound imaging systems include A-line (Amplitude), M-mode (Motion), B-mode (Brightness, including 2D, 3D and even 4D imaging), as well as the Doppler system. A handful example of diagnostic ultrasound imaging is the widely used sonograms. Another diagnostic ultrasound non-imaging technique being heavily studied in recent years is the targeted contrast ultrasound (Christiansen and Lindner 2005). However, in this study, I will only focus on diagnostic ultrasound method, particularly its application in the detection of bone quality.

2.2 Diagnostic ultrasound for bone

Bone mass can be evaluated in many ways. As the earliest imaging technique, plain radiographs has been reported to be very insensitive until the loss of bone mass reaches approximately 30 % (Epstein, Dalinka et al. 1986), not to mention the relatively high radiation dose. Measurement of Bone Mineral Ddensity (BMD) by Dual Energy X-ray Absorptiometry (DEXA) is the established technique for the diagnosis of osteoporosis. But there're still many problems remain. First, both SEXA and DEXA use ionizing radiation, which is not good for frequent monitoring although it is relatively low (~20 mrem). Second, since bone densitometry depends on the photoelectric absorption by calcium, BMD as a predictor of bone strength is based on the assumption that amount of mineral is a good indicator of bone matrix volume. However, according to literature (Boivin and Meunier 2002), the degree of bone mineralization can vary up to 10%, which makes the prediction less precise. A newer technique, Quantitative Computed Tomography (QCT) is excellent in determining actual volumetric BMD (vBMD) as well as distinguishing trabecular from cortical bone. But the use of high radiation dose (50 to 100 mrem) also limits the application of this method, especially in pediatrics (Speiser, Clarson et al. 2005).

Ultrasound techniques provide an alternative way to access bone quality non-invasively. Diagnostic ultrasound has been used in almost all medical fields and become the preferred imaging modality in a variety of clinical situations due to its advantages including portability, low-cost, non-ionizing and non-invasive nature. For example, many clinic studies showed that the results of Quantitative Ultrasound (QUS) bone measurement correlate very well with that of the more established method of BMD measurement by bone densitometry (Prins,

Jorgensen et al. 1998), while QUS doesn't use ionizing radiation. The diagnostic ultrasound methods for bone include the interpretation of ultrasound parameters after its interaction with bone, as well as the direct ultrasound imaging of bones.

2.2.1 Parameter detection

Among all ultrasound techniques, QUS is the one that has been studied most extensively and applied widely in clinic studies. QUS parameters being measured include the Broadband Ultrasound Attenuation and the Speed of Sound in bone. Another kind of ultrasound system that has been studied recently and has the potential to be used in clinic is the reflection ultrasound, in which the backscattered ultrasonic signals from the bone are used to assess its quality. Parameters such as the Broadband Ultrasound Backscatter and Apparent Integrated Backscatter have been introduced to characterize the reflected ultrasound waveforms.

Speed of Sound (SOS)

There are two types of velocity that are usually used to describe a wave, which are the phase velocity and the group velocity. Phase velocity, normally denoted by v, refers to the propagation of crests and troughs of the wave, while group velocity, denoted by U or u, refers to the propagation of energy. The magnitudes of phase velocity and group velocity are different in wave motions of which the phase velocity varies with different frequency; and the directions of the two types of velocities could also be different when propagating in anisotropic medium.

The sound velocity in cancellous bone is usually calculated from Time of Flight (TOF) measurement by transmission ultrasound methods (Njeh, Boivin et al. 1997). The TOF

method measures the sound travel time through coupled medium (gel or water), soft tissue and bone sample, between fixed ultrasound transducer separations (Figure 2-1).

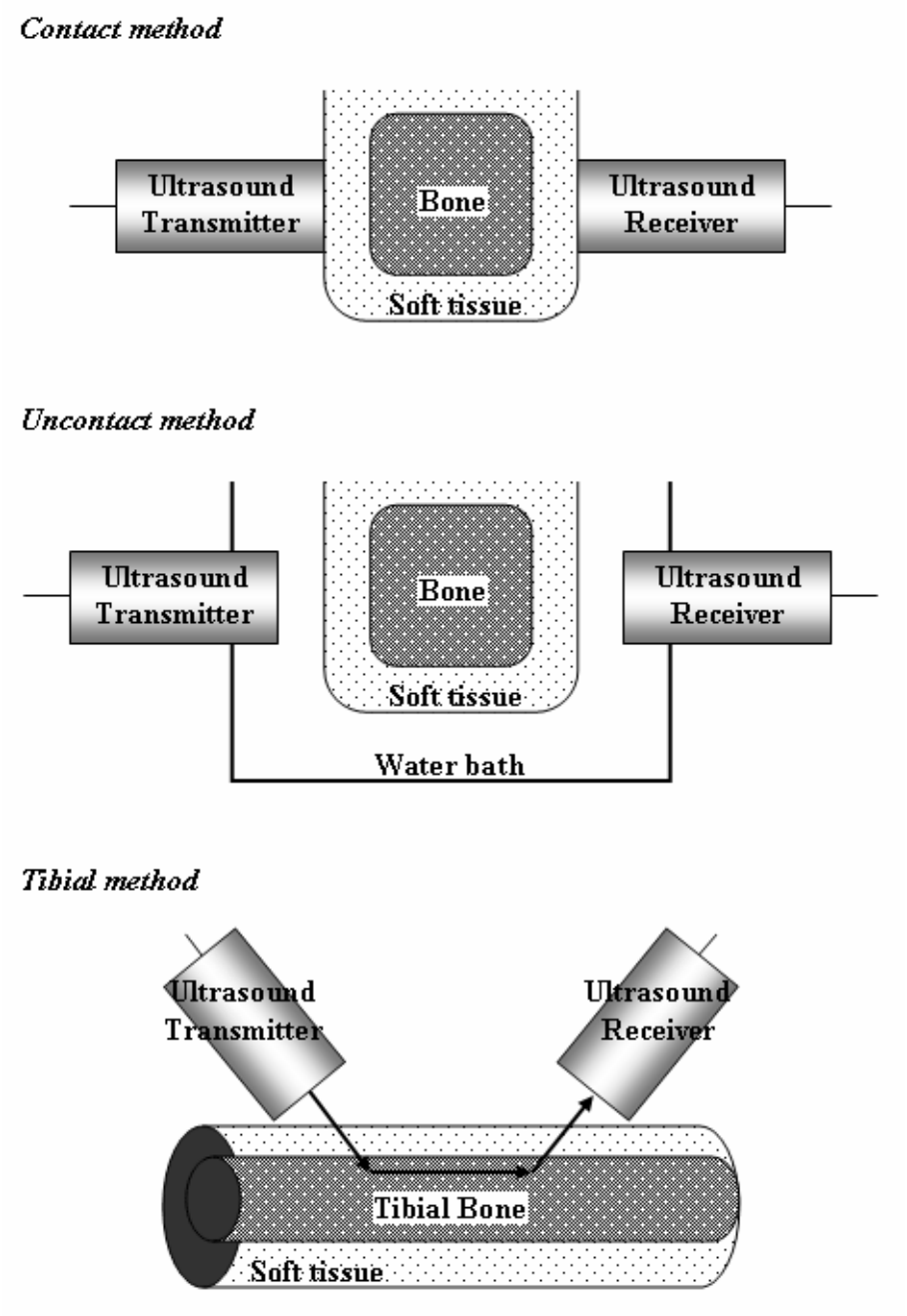

Figure 2-1 Methods of transmission ultrasound measurement.

I have performed the velocity measurement on samples of different materials using the uncontact method as illustrated in figure 2-1. The results are shown as table 2-1.

Table 2-1 SOS in different materials

Materials	Phantom velocity(m/s)
Copper	4635
Brass	4329
Normal Plastics	2370
Plastics with glass particles	2499
Teflon	1384
HDPL	2556
Acrylic Plastics	2751
Steel	5883

The way that the phase velocity changes with wave frequency is described by dispersion. There are five kinds of dispersion: 1) geometric dispersion, which is caused by boundaries of the specimen; 2) material dispersion, which is caused by the material constants that are frequency dependant such as elastic moduli; 3) scattering dispersion, which is caused by fine scatters in the medium; 4) dissipative dispersion, which is caused by the irreversible energy loss such as absorption; 5) nonlinear dispersion, which is caused by the wave speed's dependence on wave amplitude. The first four kinds are the dominant source of dispersion when ultrasound waves propagate in bone or soft tissues, so usually the last kind of dispersion is omitted.

Dispersion could be either positive or negative. It is very hard to recover the original

waveform from the dispersed one. It is important to minimize the effect of dispersion in transmission measurement.

Besides of the transmission ultrasound and TOF method for measurement of the SOS, ultrasound velocity in solid materials can also be detected by the Ultrasound Critical-angle Reflectometry (UCR) (Antich and Mehta 1997; Mehta and Antich 1997). In the simplest form of the UCR technique as shown in figure 2-2 (Antich and Mehta 1997), a pure pressure wave is generated in a liquid, e.g. water, and propagates to a solid. Once it arrivals at the liquid-solid interface, the pure pressure wave gives rise to a reflected pressure wave in the liquid as well as two refracted waves, a shear wave and a pressure wave, in the solid. The critical angle is defined as the maximum angle of incidence for which the refracted wave can propagate through the solid, or in another word, the angles of total internal reflection.

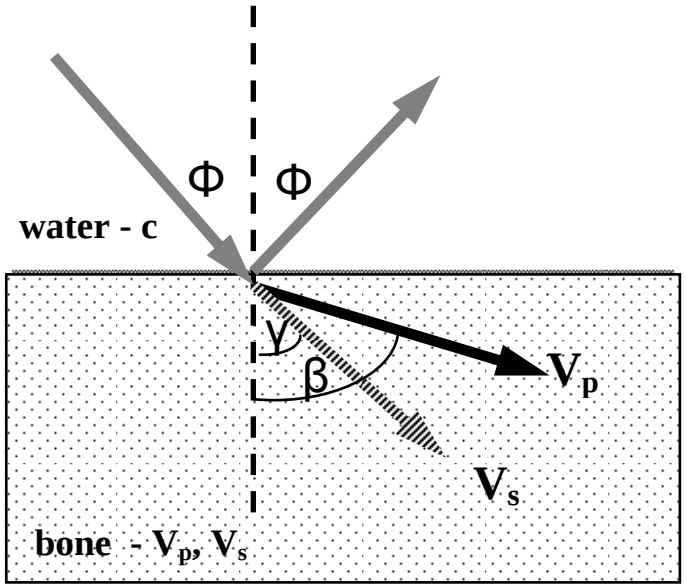

Figure 2-2 Demonstration of the UCR technique.

Since the velocity and angles of the incident wave and the refracted waves satisfy the following relationship:

$$\frac{\sin\phi}{c} = \frac{\sin\beta}{V_p} = \frac{\sin\gamma}{V_s}$$

The velocities of the pressure wave and shear wave in the solid are then determined using Snell's law:

$$V_s = \frac{c}{\sin\phi_2},\ V_p = \frac{c}{\sin\phi_1}.$$

Broadband Ultrasound Attenuation (BUA)

As the sound wave propagates in bone, attenuation occurs due to scattering and absorption. Attenuation is calculated by the ratio of the amplitude of unattenuated signal (transmitted signal) over the amplitude of the attenuated signal (received signal, attenuated by bone). Its expression in decibel (dB) is given below:

$$Att(f) = 20\log\frac{A_T(f)}{A_R(f)}.$$

The value of attenuation changes with different frequency of the sound waves. Broadband ultrasound attenuation is the parameter that characterizes the property of attenuation changing with frequency. It is determined by the slope of frequency depended attenuation curve:

$$BUA = \frac{\Delta Att(dB)}{\Delta f(MHz)}.$$

Broadband Ultrasound Backscatter (BUB)

Generally, the backscattered signals are acquired as described by Chaffai et al (Chaffai, Peyrin et al. 2002).Generally, a gated region is isolated to select the data from a location inside the bone and exclude the large specular reflection arising from the front surface of the specimen. If a focusing transducer is adopted, then this gate region is usually set at the focal length of the transducer. This gated echo signal is then used to calculate the frequency-averaged backscatter coefficients, and for instance, the Broadband Ultrasound Backscatter (BUB). A reference signal is used to deconvolute the frequency response of the measuring equipment (i.e., for calibration).

To calculate the BUB, firstly the gated echo signal is multiplied by the hamming window function and then taken Fourier transform to get its power spectrum. Then an estimated backscatter coefficient $\mu_B(f)$ is obtained by the log-spectral subtraction of the calibration spectrum from the spectrum of the windowed signal in order to deconvolute the frequency response of the measuring equipment, given by:

$$\mu_B(f) = 8.68 \ln \frac{\langle S_B(f) \rangle}{S_R(f)} C(f) Factors(f),$$

where $\langle S_B(f) \rangle$ is the averaged (normally in terms of integration) backscattered power spectrum of the gated region. Averaging is to remove pure statistical variations due to the random phase shift introduced by each scattering trabeculae. $S_R(f)$ is the reference spectrum. And the attenuation correction term $C(f)$ and frequency-dependent scattering volume correction term $Factor(f)$ are given by:

$$C(f) = e^{4\hat{\alpha}(f)z} \frac{4\hat{\alpha}(f)d}{e^{2\hat{\alpha}(f)d} - e^{-2\hat{\alpha}(f)d}},$$

and $$Factor(f) = \frac{1}{(0.63)^2} \frac{k^2 a^2}{8\pi d\left[1 + \left(\frac{ka^2}{4F}\right)^2\right]},$$

where $\frac{1}{(0.63)^2}$ is the compensation for hamming window function, $\hat{\alpha}(f)$ the frequency-dependent attenuation coefficient, d the gate length, z the attenuated path between the front surface of the specimen and the gated region, $k = 2\pi/\lambda$ the wave number and F the transducer focal length if applicable.

The broadband ultrasound backscatter (BUB), or called integrated backscatter coefficient (IBC) by some literatures (Roberjot, Laugier et al. 1996), is obtained by averaging (integrating) all $\mu_B(f)$ in the frequency bandwidth of the transducer from $f_{\min}$ to $f_{\max}$, according to:

$$BUB_{dB} = \frac{\int_{f_{\min}}^{f_{\max}} [\mu_B(f)]_{dB}\, df}{f_{\max} - f_{\min}}.$$

Some researchers also use a parameter called relative ultrasound backscatter which is the frequency-averaged backscatter power spectrum without the compensation for attenuation (Wear and Garra 1998). Similar parameters include the Apparent Integrated Backscatter (AIB) (Hoffmeister, Whitten et al. 2002; Hoffmeister, Jones et al. 2006) and Integrated Reflection Coefficient (IRC) (Hakulinen, Day et al. 2005).

2.2.2 Ultrasound imaging

Ultrasound can be used as a tool to generate images and study mechanical properties of bone. Bone is usually considered as a viscoelastic and nonlinear medium in microscopical level. As mentioned in previous section, the viscous effect can be ignored as the frequency of ultrasound wave is high enough (much higher than the relaxation frequency of viscoelastic effects); and the displacement caused by ultrasound is small enough that the nonlinear effects can be neglected.

Ultrasound imaging is based on the detected ultrasonic parameters, such as localized attenuation and velocities. For instance, ultrasound shear wave imaging has been proposed as an useful tool to image bone as it can provide shear properties of bone which may be very valuable for diagnostic purposes (Ye, Wu et al. 2000). Such imaging systems adopt high-frequency ultrasound wave to do the B-mode imaging.

Ultrasound imaging can also be used to image bone fracture. High-resolution sonography has been proposed to be a powerful, non-invasive, readily available and cost effective imaging technique to detect occult bone fracture that cannot be visualized on plain radiographs (Wang, Shieh et al. 1999; Enns, Pavlidis et al. 2004). It has been shown that ultrasound surface rendering could favorably correspond to the radiograph and allow assessment of the morphology of the fracture (Hunerbein, Raschke et al. 2000).

2.2.3 Diagnosis of pediatric bone diseases

Typical pediatric bone diseases include osteogenesis imperfecta (OI), juvenile osteoporosis and Fibrous dysplasia (FD). OI is a genetic bone disorder usually caused by the deficiency of

type I collagen. It is also known as Brittle Bone Disease, as OI patients tend to have weak or fragile bones associated with pain and skeletal deformities. Juvenile osteoporosis, including primary and idiopathic forms and a number of secondary forms, is mainly due to inherited conditions from birth and early infancy, and occurs typically before the onset of puberty. It may also be acquired during childhood and seen in young children having rapid growth. Affected patients might have vertebral compression fractures and fractures of the metaphysis of long bones as well as difficulty in walking and significant bone pain. Histomorphometry study shows dramatic (>50%) reduction in cancellous bone volume with reduced trabecular thickness and number in the iliac chest samples from patients when compare with age-matched controls (Rauch, Travers et al. 2000). FD is an uncommon, non-inherited skeleton disorder caused by activating, missense mutation of the GNASI gene encoding the α subunit of the stimulatory G-protein in somatic cells during the phase of rapid growth. Although it has a broad range of clinic expressions from single skeleton site to a severe disabling disease, pain, fracture and deformity of bone are the common feature.

The diagnosis of osteoporosis in children is different from in adults, as it's complicated and unclear. As described in Part 2.2, plain radiograph has poor precision and QCT has high radiation dose, making them unsuitable for children to use. Rather than determine the true volumetric BMD as by QCT, the most commonly available bone densitometry, including both SEXA and DEXA, determines the real BMD as the bone mineral content per unit surface area of the bone in the region of interest (ROI). The BMD determined by this method increases as the bones get larger, which means the smaller children will have lower BMD than larger children, even if their volumetric BMD is equal. This size dependency causes

errors as the BMD of smaller bone get underestimated and that of larger bone is overestimated. So far no correction method regarding this error is utilized in regular clinic use. Moreover, this real BMD is a 2-D parameter reported in g/cm^2, regardless of the depth of the ROI, i.e., can not distinguish between the periosteal surface and the endosteal surface. But the reality is, the closer the bone is located to the periosteal surface, the stronger the bone and the lesser the fracture risk (Specker and Schoenau 2005).

Diagnostic ultrasound techniques avoid the use of ionizing radiation, which makes it suitable for repeated measurements in children. It has been reported recently that quantitative ultrasound (QUS) measured at calcaneus is comparable to DXA in detecting low bone mineral in young patients with fragility fractures, indicating the effectiveness of QUS as a screening tool for diagnosing children osteopenia and osteoporosis (Fielding, Nix et al. 2003). However, QUS is related to the real BMD as determined by bone densitometry. So its result is also influenced by bone size and cortical thickness, making the interpretation of QUS evaluation of certain sites like tubular bones more problematic. On the other hand, reflection (pulse-echo) ultrasound and critical angle reflectometry are related to the real volumetric bone density and elasticity, and therefore would be better for the diagnosis of pediatric bone diseases and assessment of treatment. But generally, the use of diagnostic ultrasound in pediatric field is still in its infancy, and attracting more and more interest.

Chapter 3 Literature Review

Ultrasound technologies have been intensively studied to access bone properties. Researches indicated that the parameters of attenuation and velocity, which is BUA and SOS respectively, can be used to replace the BMD measurements by current bone densitometry techniques using ionizing radiation (Padilla and Laugier 2005).

Beside of the assessment of bone mineral changes, ultrasound techniques could also be used to provide non-BMD related bone properties, such as porosity, mechanical properties (i.e., elasticity), and probably microarchitecture (Hans, Arlot et al. 1995; Rico, Hernandez et al. 2001; Cortet, Boutry et al. 2004). These properties direct related to the morphology and strength of the bone (Mehta, Oz et al. 1998; Mehta, Antich et al. 2001), and therefore might be better markers for diagnosis of osteoporosis and prediction of osteoporotic fracture risk.

3.1 Models of Wave Propagation in Cancellous Bone

The ability of ultrasound methods to detect cancellous bone microarchitecture has not been cleared demonstrated. This is because cancellous bone has a very complex trabecular network structure, with fatty marrow filling the spaces in between. When ultrasonic wave enters this complex structure, it undergoes both scattering and absorption processes along the

propagation path. As the property of ultrasound, reflection occurs at every interface of trabeculae and marrow. Since there're a lot of such interfaces inside the cancellous bone, it is difficult to clearly describe the wave propagation in cancellous bone. The poor understanding of ultrasound interaction with bone has largely affect the development of diagnostic ultrasound. Many people have been working on this topic since 1950s, but so far only a few theoretical models have been validated to explain the ultrasonic wave propagation in cancellous bone (Zwikker and Kosten 1949; Biot 1956; Biot 1956; Attenborough 1982; Lee, Roh et al. 2003; Roh and Yoon 2004).

3.1.1 Biot's theory

One of the earliest established theories of wave propagation in porous media is the Biot's theory. After initiated by Biot in the 1950s (Biot 1956; Biot 1956), this theory has been well developed and adopted to characterize the ultrasound propagation in porous cancellous bone (Zwikker and Kosten 1949; Attenborough 1982; McKelvie and Palmer 1991; Williams 1992; Hosokawa and Otani 1997; Hosokawa and Otani 1998; Haire and Langton 1999; Lee, Roh et al. 2003; Mohamed, Shaat et al. 2003; Fellah, Chapelon et al. 2004; Roh and Yoon 2004; Wear, Laib et al. 2005). According to this theory, the porous media is conceptually modeled as a rigid homogeneous material containing identical paralleled cylindrical capillary pores which are normal to the surface and along the incident wave propagation direction.

Biot theory starts with the assumption that the pore size of the porous media is small compared with the wavelength of the elastic waves. Generally, the arbitrary size of a scattering particle (x) is defined by the ratio of its geometric dimension (r) and wavelength of

the incident wave (λ) as:

$$x = \frac{2\pi r}{\lambda}.$$

When the particle size is much smaller than the incident wavelength, i.e., x<<1, the scattering is called Rayleigh scattering, and the intensity of the scattered wave (or called scattering coefficient) varies inversely with the fourth power of the wavelength. This explains why the sky is blue, as the scattered blue light with shorter wavelength has much bigger intensity than the other colors.

With this assumption of Biot's theory, the scattering process can now be classified as Rayleigh scattering, so this model is also referred to as the Rayleigh model.

Biot's theory predicted that there're two types of longitude waves propagating in the porous media and one type of transverse wave. The two longitude waves are known as waves of the first and second kind, which are also denoted as the fast and slow waves referring to their propagating velocity. The slow waves are highly attenuated due to the diffusing process, and highly affected by temperature. The fast waves are called "true waves" by Biot, as their dispersion is negligible. The frequency of the transverse waves is proportional to the absorption coefficient of the porous medium (Biot 1956).

The characteristic frequency equation of the Biot's model, which describes the dispersion relation of both waves for isotropic materials, is given by (Stoll and Bryan 1970):

$$\begin{vmatrix} Hl^2 - \rho\omega^2 & \rho_f\omega^2 - Cl^2 \\ Cl^2 - \rho_f\omega^2 & \alpha\rho_f\omega^2 \big/ \beta - Ml^2 - i\omega F(\kappa)\eta/k \end{vmatrix} = 0,$$

where l is the complex wave number as $l = l_r + il_i$, ω is the angular frequency of the

waves. ρ is the total density of the fluid saturated porous medium, given by the porosity β and the density of solid (pore wall) ρ_s and fluid filled in the pores ρ_f as:

$$\rho = (1-\beta)\rho_s + \beta\rho_f .$$

α is the tortuosity of the porous medium, which is determined by (Berryman 1980):

$$\alpha = 1 - r(1 - 1/\beta),$$

where *r* is a variable calculated from a microscopic model of a frame moving in the fluid.

$F(\kappa)\eta/k$ accounts for the viscous resistance to the fluid flow, with η the viscosity of the fluid, and k the permeability coefficient, and factor $F(\kappa)$ given by:

$$F(\kappa) = \frac{1}{4}\left[\frac{\kappa T(\kappa)}{1 - 2T(\kappa)/i\kappa}\right],$$

with

$$T(\kappa) = \frac{\left(-\sqrt{-i}\right)J_1\left(\kappa\sqrt{-i}\right)}{J_0\left(\kappa\sqrt{-i}\right)},$$

and

$$\kappa = a\left(\omega\rho_f/\eta\right)^{1/2},$$

where a is a parameter depending upon both the size and shape of the pores with the dimension of length, and $a = (8\alpha k/\beta)^{1/2}$. J_0 and J_1 the zeroth and first order cylindrical Bessel functions, respectively.

H, C and M are generalized elastic coefficients introduced by Biot (Biot 1956; Biot 1956) and expressed in terms of the complex bulk modeuli of the saturated porous medium K_b, the

solid material comprising the pore walls K_s and the fluid within the pores K_f, as well as the complex shear modulus of the solid material μ_b, as are given below:

$$H = \frac{(K_s - K_b)^2}{D - K_b} + K_b + \frac{4}{3}\mu_b ,$$

$$C = \frac{K_s(K_s - K_b)}{D - K_b},$$

and

$$M = \frac{K_s}{D - K_b},$$

where

$$D = K_s\left[1 + \beta\left(\frac{K_s}{K_f} - 1\right)\right].$$

It has been demonstrated that by assuming the isotropy of the material, the intrinsic bulk modulus of the solid material comprising the pore walls and frames, K_s, can be calculated form its Young's modulus E_s as (Lang 1969; Katz and Meunier 1987):

$$K_s = \frac{E_s}{3(1 - 2\nu_s)},$$

with ν_s the Poisson's ratio of the solid material such as bone.

And according to Gibson, the bulk modulus K_b and shear modulus μ_b of the porous medium can also be expressed in terms of the Young's modulus E_b and the Poisson's ratio pf the porous medium (Gibson 1985):

$$K_b = \frac{E_b}{3(1-2\nu_b)},$$

and

$$\mu_b = \frac{E_b}{2(1+\nu_b)},$$

where E_b can be related to E_s as $E_b = E_s(1-\beta)^n$, with the power index n depending on the alignment of the structure.

Then by solving the fully analyzed characteristic frequency equation of the Biot's model, the wave numbers of the fast and slow wave in the porous medium are obtained as:

$$\frac{l_{fast,slow}}{\omega} = \left\{ \frac{(Hm + M\rho - 2C\rho_f) \mp \left[(Hm + M\rho - 2C\rho_f)^2 - 4(HM - C^2)(\rho m - \rho_f{}^2)\right]^{1/2}}{2(HM - C^2)} \right\}^{1/2},$$

where

$m = \alpha\rho_f / \beta - iF(\kappa)\eta / k\omega$.

The phase velocities of the fast and slow waves $\omega / \mathrm{Re}\left[l_{fast,slow}\right]$ can be found as a function of frequency, as given by (Hosokawa and Otani 1998):

$$V_{fast,slow} = \left\{ \frac{2(HM - C^2)}{(Hm + M\rho - 2C\rho_f) \mp \left[(Hm + M\rho - 2C\rho_f)^2 - 4(HM - C^2)(\rho m - \rho_f{}^2)\right]^{1/2}} \right\}^{1/2}.$$

Analytically, this model effectively explains the ultrasound velocity by the prediction of two longitude waves (fast and slow wave) which have been proved experimentally. However, the predicted attenuation of ultrasound (no negative dispersion of phase velocity and much higher attenuation of slow wave than fast wave) has a great discrepancy with the

experimental data (McKelvie and Palmer 1991; Hosokawa and Otani 1997; Hughes, Leighton et al. 1999; Kaczmarek, Kubik et al. 2002). One possible reason of this discrepancy is that, Biot's model is based on the assumption of much longer wavelength than the characteristic pore size (i.e., Rayleigh scattering), which is not valid in most experiments where the wavelength of the applied ultrasonic waves is comparable or even less than the pore size. Since Rayleigh scattering is not the case, the scattering should be modeled by either Mie theory (Barber and Hill 1990) or Discrete dipole approximation (DDA) (Draine and Flatau 1994).

Also, the Biot's model ignores the sensitivity of ultrasound attenuation to the complex, inhomogeneous and anisotropic trabecular architecture, as it assumes the cancellous bone to be a homogeneous porous material. Moreover, this model involves more than ten parameters, and many of them are just theoretical and hard to be determined experimentally, which makes it difficult to use (Haire and Langton 1999; Njeh, Hans et al. 1999; Lin, Qin et al. 2001).

There're some modified Biot's model coming out in recent years, such as the Modified Biot-Attenborough (MBA) model (Lee, Roh et al. 2003; Roh and Yoon 2004; Lee and Yoon 2006; Lee, Hughes et al. 2007; Lee, Humphrey et al. 2007). The Biot's model considers the viscous effect of the fluid but doesn't include the thermal effect; the Attenborough's theory takes into account of both the viscous and thermal effects, but due to the assumption of rigid material of the pore frames, the fast wave is not considered in this model. The MBA model combines the merits of these two theories by specifying the thermal effect with an analytic solution and allowing a nonrigid solid material for the pore frames by parametric fitting.

However, the drawback of the MBA model is still that, some of the induced parameters are empirical and have to be determined from experimental data.

3.1.2 Stratified model

Besides Biot's theory, there're many studies that modeled the cancellous bone as a stratified media (Schoenberg 1984; Hughes, Leighton et al. 1999; Lin, Qin et al. 2001; Wear 2001). This model simplifies the trabecular network of cancellous bone into layered structure (Figure 3-1).

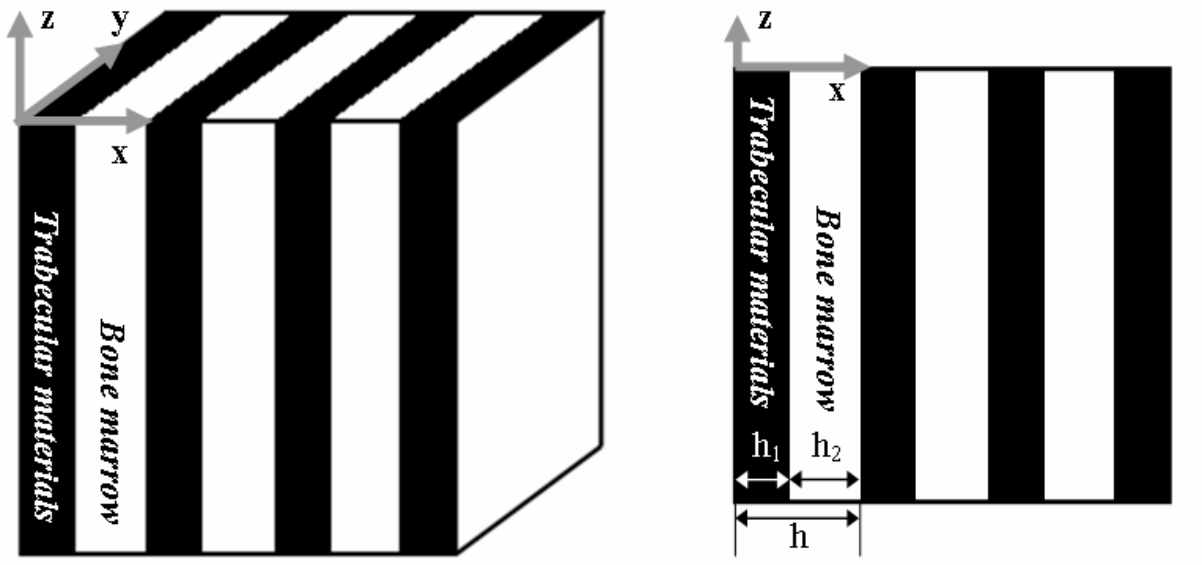

Figure 3-1 Stratified model for trabecular bone (left) and its 1-D demonstration (right). Trabecular materials (dark) and bone marrow (white) are arranged in alternating layers. The thickness h is also the period of the medium, as $h = h_1 + h_2$. The wave is assumed to propagate in the x direction, normal to the interfaces of the layers.

Unlike the Biot's model described previously, which attempts to put all the bone properties in the model, the stratified model focuses on the reflection and transmission of ultrasound at the interfaces between trabecular materials and bone marrow. The periodic structure of the model imposes periodic conditions on the solution to the wave equation, which means that the velocities and pressures at location z are the same as those at $z + nh$, where n is an integer. In this model, the apparent density ρ of cancellous bone is directly related to its porosity β and trabecular density ρ_s, as given bellow (Lin, Qin et al. 2001):

$$\rho = (1-\beta)\rho_s .$$

The wave propagation in such alternating layers was first described by Schoenberg in 1984 (Schoenberg 1984). In Schoenberg's theory, the dispersion relation of the periodically layered medium is derived by relating continuous acoustic field variables in adjacent period by propagator matrices. A slowness vector, $\vec{s} = (s_1, s_2, s_3)$, is introduced to express the acoustic wave propagation, with s_1 parallel to the layers and s_3 normal to the layers, and satisfies the following relation:

$$\left(\frac{{s_3}^2}{\langle\rho\rangle}\right) - \left[\frac{\beta\left({V_f}^{-2} - {s_1}^2\right)}{\rho_f} + \frac{(1-\beta)\left({V_f}^{-2} - {s_1}^2\right)}{\rho_s\left(1 - {V_{pl}}^2 {s_1}^2\right)}\right] = 0,$$

where the average density $\langle\rho\rangle = \beta\rho_f + (1-\beta)\rho_s$, and the plate velocity $V_{pl} = 2\left(1 - {V_{sh}}^2 / |\vec{s}|^2\right)^{1/2} V_{sh}$.

From this relationship, the phase velocity equals to the inverse of the magnitude of the slowness vector ($|\vec{s}| = \sqrt{{s_1}^2 + {s_3}^2}$), and the propagation angle through the layers relative to stratification equals to the phase angle of the vector ($\theta = \tan^{-1}(s_3 / s_1)$).

Schoenberg's theory also predicts two longitudinal waves for propagation angles other than that perpendicular to the plate where only one exists. The two longitudinal waves are equivalent to the fast and slow waves described in the Biot's theory. Inertial coupling changes with the propagation angle; it equals to zero when propagation is parallel to the layers (propagation angle is 90º), which means the waves propagate in the solid and fluid independently; it reaches its maximum when propagation is normal to the layers (propagation angle is zero), in which case the slow wave disappear and only fast wave propagates.

When ultrasound travels through the model in the direction of the stratification, assume it takes t_s seconds in the trabecular layer (solid phase) and t_l seconds in the bone marrow layer (liquid phase). Therefore t_s and t_l are:

$$t_s = \frac{h_1}{v_s} = \frac{(1-\beta)h}{v_s},$$

$$t_l = \frac{h_2}{v_l} = \frac{\beta h}{v_l},$$

where v_s and v_l are the ultrasound velocities in the solid and liquid phase, respectively. And the sound velocity in this model is:

$$v = \frac{h}{t_s + t_l} = \frac{v_s v_l}{\beta v_s + (1-\beta)v_l} \quad .$$

Hughes et al compared the ultrasound phase velocities predicted by both Biot's theory and Schoenberg's theory (Hughes, Leighton et al. 1999). Biot's theory doesn't consider the wave propagation angle, so the velocities are constant for all angle of propagation and correspond to the 90º case in the Schoenberg's theory. The variation of the velocities between these two theories is within 10% of each other when the waves propagate parallel to the layers (90º).

The advantage of modeling the cancellous bone as alternating layers of solid and fluid-like materials are: 1) the boundary conditions between the layers give rise to the degeneration of the propagating sound wave and 2) the exact solution of the wave propagating parallel to the stratification can be obtained, which would be helpful in explaining the wave propagation in porous media (Schoenberg 1984). When compared with the Biot's model which needs more than 10 parameters, the stratified model requires the input of much less parameters (six for the Schoenberg's theory, i.e., densities, speeds in the two materials, and porosity), which makes it better for the computational aspect. But in the stratified model, the fluid viscosity is not considered.

3.1.3 Numeric Simulation

The modeling of cancellous bone is very difficult due to the complexity of this material. Other models of wave propagation in cancellous bone include the numerical simulated model proposed by Langton et al (Langton, Whitehead et al. 1997) and Bossy et al (Bossy, Padilla et al. 2005). In their method, the cancellous bone model is generated by feeding into self-developed software the 3-D images of real bone sample obtained by the synchrotron microtomography. Therefore, this numerical model can very well simulate the real trabecular network of cancellous bone. However, no theoretical derivations could be obtained from this model.

3.2 Ultrasonic Characterization of Cancellous Bone

Cancellous bone can be characterized by many parameters, both material properties such as elasticity and porosity, and acoustic properties including velocity (SOS) and attenuation

(BUA, BUB, etc). It can be measured by both transmission (QUS) and reflection ultrasound methods.

3.2.1 Transmission ultrasound characterization of bone

The typical transmission ultrasound is the quantitative ultrasound (QUS) method described in previous chapter. QUS parameters are well correlated with local bone mineral density (BMD), and can be used to assess the progression of bone demineralization (Wu, Gluer et al. 1998). Nevertheless, how the QUS variables correlate with non-BMD-related bone parameters such as microarchitecture is still unclear and has been the source of many studies (Njeh, Fuerst et al. 2001; Cortet, Boutry et al. 2004). So far, strong evidence has been shown that acoustic anisotropy affect the classic transmission QUS parameters (Glüer, Wu et al. 1993; Nicholson, Haddaway et al. 1994; Hans, Wu et al. 1999), but the potential clinic benefit of the characterization of bone anisotropy has not been thoroughly investigated (Chaffai, Peyrin et al. 2002). Moreover, there are many other factors that affect the QUS measurement that should also be taken into account when interpreting clinical QUS measurement, such as the cortical density and thickness at the site of measurement (Prevrhal, Fuerst et al. 2001), collagen content and perhaps its organization (Hoffmeister, Whitten et al. 2002), and bone marrow properties (Nicholson and Bouxsein 2002).

3.2.2 Reflection ultrasound characterization of bone

Reflection ultrasound, also called pulse-echo ultrasound or backscattering of ultrasound, offers another way to probe cancellous bone quality, microarchitecture and their changes (Antich, Pak et al. 1993; Chaffai, Peyrin et al. 1999; Chaffai, Peyrin et al. 2002; Wear 2003;

Jenson, Padilla et al. 2004; Wear 2004). It measures the signals reflected from the trabecular network, and the backscattering depends upon the scatterers' (the trabeculae elements for cancellous bone) elastic properties, spatial distribution and size (Padilla and Laugier 2005). Therefore it has the potential to assess directly the microstructure of trabecular bone; for instance, trabecular thickness and trabecular number density.

Using reflection ultrasound has some advantages over transmission methods. First, only one transducer is needed. It works as both transducer and receiver, which largely increases the detection sites of the human body as compared to the limited locations for QUS measurement. Second, reflected ultrasound has the potential to be adapted for cross-sectional imaging of bone, just like the B-mode imaging modalities for soft tissue characterization. Some literatures also suggest that reflection ultrasound is more related to bone quality and microstructure, while transmission ultrasound mainly reflects bone quantity (Roberjot, Laugier et al. 1996).

A number of investigators have proposed the use of ultrasonic backscatter for bone assessment in the past decade, most of which use frequency analysis and characterize the echo signals by parameters such as broadband ultrasonic backscatter (BUB) (Chaffai, Peyrin et al. 1999; Chaffai, Peyrin et al. 2002; Wear 2003; Jenson, Padilla et al. 2004; Wear 2004), relative ultrasound backscatter (RUB) (Wear and Garra 1998), apparent integrated backscatter (AIB) (Hoffmeister, Whitten et al. 2002; Hoffmeister, Jones et al. 2006) and integrated reflection coefficient (IRC) (Hakulinen, Day et al. 2005). I have described the way to calculate the value of BUB initialized by Chaffai et al (Chaffai, Peyrin et al. 1999; Chaffai, Peyrin et al. 2002).

Jenson et al demonstrated that the backscatter coefficient was related to the 3-D spatial Fourier transform of cancellous bone microarchitecture (Jenson, Padilla et al. 2004).

3.2.3 Ultrasound reflection with oblique incidence

Most of ultrasound reflection methods deal with the direct backscatters, which mean the backscattering signal in the reverse direction of wave propagation. However, there're also some studies consider the reflection from oblique incidence, and the way that the reflected signal changes with the oblique incident angle (Antich, Anderson et al. 1991; Antich, Pak et al. 1993; Antich and Mehta 1997; Mehta and Antich 1997; Mehta, Antich et al. 2001; Fellah, Berger et al. 2003; Fellah, Mitri et al. 2003).

Fellah et al derived porosity and tortuosity of an air-saturated slab of rigid porous material via the measurements of reflected waves at two oblique incident angles (Fellah, Berger et al. 2003; Fellah, Mitri et al. 2003). Antich et al designed and implemented a different ultrasound reflection approach called ultrasound critical-angle reflectometry (UCR) (Antich, Anderson et al. 1991; Antich, Pak et al. 1993; Antich and Mehta 1997; Mehta and Antich 1997; Mehta, Antich et al. 2001).

UCR is a non-invasive and non-destructive method which measures the pressure and shear wave velocities in materials by detecting the angles of total internal reflection for refracted waves, and the results can be used to determine multiple components of the elasticity matrix of bone (Antich and Mehta 1997; Mehta and Antich 1997). As mentioned before, there is a strong statistical correlation between elasticity and bone strength. Moreover, measurement of all components of the elasticity matrix is a more sensitive prediction of bone quality than

measurement in one preferred direction. Therefore, UCR method is a very useful tool to access bone quality and predict the risk of bone fracture.

Chapter 4 Simulation of Cancellous Bone

Bone, especially cancellous bone has complex structure; it is heterogeneous, porous, viscoelastic, and acoustically anisotropy and highly scattering. The complexity of cancellous bone makes it difficult to develop analytical models to study wave propagation in bone unless using assumptions to simplify the microstructure. However, the computer simulation comes out as a tool that allows virtual experiment with some unrealistic assumptions or experiment conditions that could help with the understanding of wave propagation in bone from the basis. It avoids some difficulties associating with real experiment so that it realizes the study of several interaction mechanisms such as absorption and scattering.

Given the complex structure of cancellous bone and the unclear underlying physics of the interaction between ultrasonic waves and cancellous bone, different bone-mimicking phantoms have been proposed to help the understanding of the relationships between ultrasonic properties and the trabecular microarchitecture (Kaczmarek, Kubik et al. 2002; Lee, Roh et al. 2003; Pereira, Bridal et al. 2004; Wear 2004; Wear 2005; Lee and Choi 2007). Currently there are two kinds of models that are used mostly, the cellular model (Kaczmarek, Kubik et al. 2002; Lee, Roh et al. 2003; Lee and Choi 2007) and the wire model (Pereira, Bridal et al. 2004; Wear 2004; Wear 2005). The cellular models are usually cubes or cylinders containing paralleled or crossed capillary holes, which mimic the two phase structure of trabecular networks and pores of the cancellous bone, respectively. The wire

model consists of paralleled wires in a two-dimensional rectangular grid array, with each wire simulates a single trabeculae. These two models simulate the cancellous bone and predict the ultrasound backscattering models from two different perspectives. However, since there's no report of computer simulated of the wire model so far, it is not clear which model would be a better mimicking of the cancellous bone. So in this study, both models were simulated on the same platform under the same conditions for the first time, and their performances were analyzed and compared.

4.1 Simulation tool

There're many programming tools that can be used to do computer simulation of wave propagation in cancellous bone. Here I chose to use MATLAB® (The MathWorks, Inc., Natick, MA) and Field II ultrasound simulator (Jensen and Svendsen 1992). MATLAB® is an interactive environment that enables one to perform computationally intensive tasks using programming language similar to C language. It has been widely used in technical computing, signal/imaging processing, control design, modeling and analysis and so on. Field II ultrasound simulator is a set of programs running under MATLAB® for simulating all kinds of ultrasound transducer fields and the associated images using linear acoustics. This program set consists of a C program and a number of MATLAB® m-functions that calls this program. All calculations are performed by the C program, and all data is kept by the C program. The associated m-functions can be divided into three groups, as they are used for initializing the program, defining and manipulating transducers, and for performing calculations, respectively.

To validate the use of MATLAB® and Field II ultrasound simulator, an unrelated simulation of blood flow was made. Because of the viscous dragging force applied on the blood flow from the inner wall of blood vessel, the flow close to the vessel wall has a smaller velocity than in the center part of the vessel. In the simulation , the radius of blood vessel was set to be 5mm, scatterer density (red blood cells per resolution unit) was set to be 10, and distance from the mid-point of the blood vessel to the transducer was 7 cm. Assuming the largest velocity of RBC (flow in the center of the vessel) was 0.5 m/s. A 3 MHz focusing ultrasound transducer was used and the sampling frequency was set to be 100 MHz. The detection system used pulse-echo measurement; totally 10 pulses were emitted and the pulse repetition rate was 0.1 ms. Signal processing used the quadrature detection method as described by Zheng and Greenleaf (Yi and Greenleaf 1999)(Figure 4-1(A)). The result was shown in figure 4-1. The detected blood flow velocity across the blood vessel showed a clear envelope with a parabolic-alike shape indicating the viscous coupling between the blood flow and vessel wall. This result validated the simulation method of using MATLAB® and Field II ultrasound simulator together to realize the virtual ultrasound experiment.

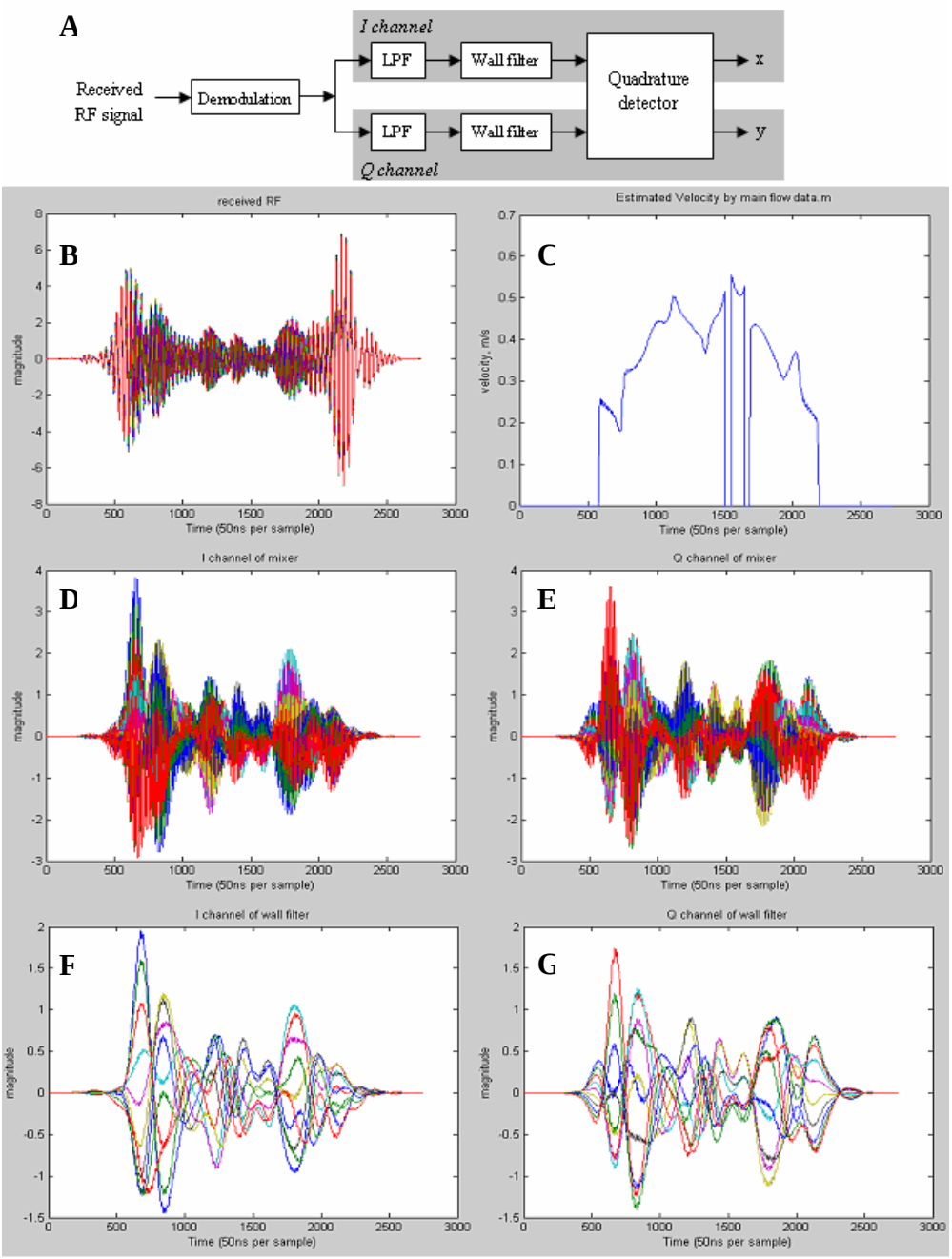

Figure 4-1 Computer simulation results of blood flow velocity estimation.

A) Block diagram of typical quadrature demodulator and flow velocity vector generator. *x* and *y* are the real and imaginary components of velocity vector; B) received backscatter signal from the blood vessel; C) estimated velocity along the cross-section of blood vessel after signal processing; D) and E) Backscattered signal at real (*I*) and imaginary (*Q*) channels, respectively, as well as their envelope detected after wall filter (F and G). Different colors represent echoes from different pulses.

4.2 Simulation of cancellous bone

The simulation of blood flow velocity estimation has proved that MATLAB® and Field II ultrasound simulator together provide a theoretical tool to simulate wave propagation in the self-defined medium. So in my study they were adopted to study the performance of the cellular model and the wire model via studying the backscattering of ultrasound after interacting with these two models.

4.2.1 Construction of the two models

The cellular model was generated as a cubic phantom containing paralleled capillary pores (Figure 4-2). The distance between the centers of any two adjacent pores was set to be 1 mm on the normal plane. So the porosity of the model was controlled by changing the size of the capillary pores. As the pore radius varied from 0.1 mm to 0.55 mm, the corresponded porosity increased from 3 % to 95 % (Table 4-1).

Table 4-1 Properties of the simulated cellular model.

Phantom	Pore Diameter	Porosity	Phantom	Pore Diameter	Porosity
1	0.1 mm	3 %	9	0.4 mm	50 %
2	0.15 mm	7 %	10	0.425 mm	57 %
3	0.2 mm	13 %	11	0.45 mm	64 %
4	0.25 mm	20 %	12	0.475 mm	71 %
5	0.3 mm	28 %	13	0.5 mm	79 %
6	0.325 mm	33 %	14	0.525 mm	87 %
7	0.35 mm	38 %	15	0.55 mm	95 %
8	0.375 mm	44 %			

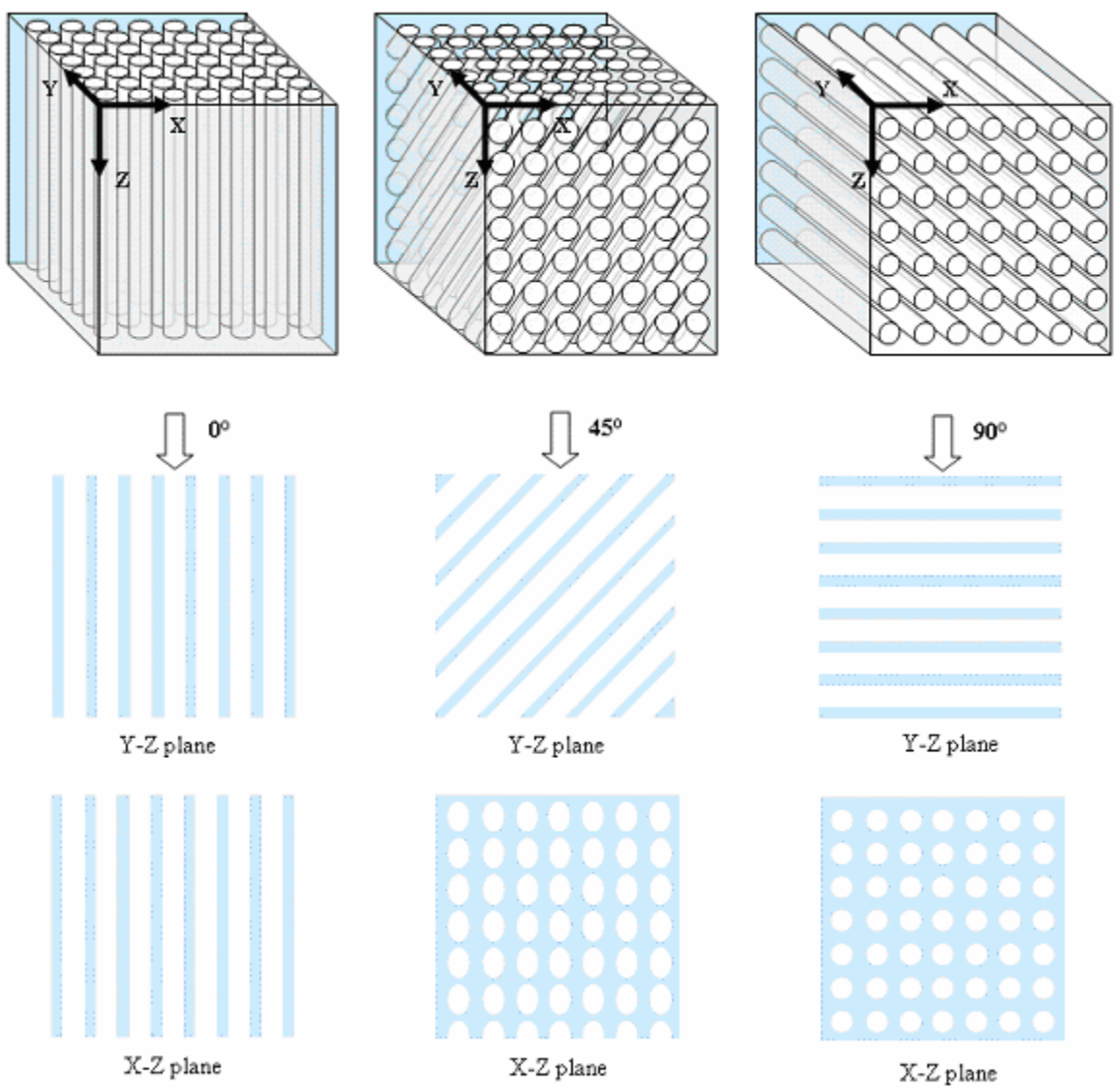

Figure 4-2 Cellular models to study the effect of trabecular orientation. The white arrows indicate the angle of incidence.

The angle between the incident wave and the aligned direction of the pores were subject to change depending upon the focusing of this study, as shown in Figure 4-2. In this study, the angels varied from 0° (the direction of wave propagation was parallel to the orientation of the capillary holes) to 90° (the capillary holes lied perpendicular to the direction of wave propagation) with a 10° increment.

The wire model was generated as an array of paralleled wires which represent the trabecular of the cancellous bone (Figure 4-3).

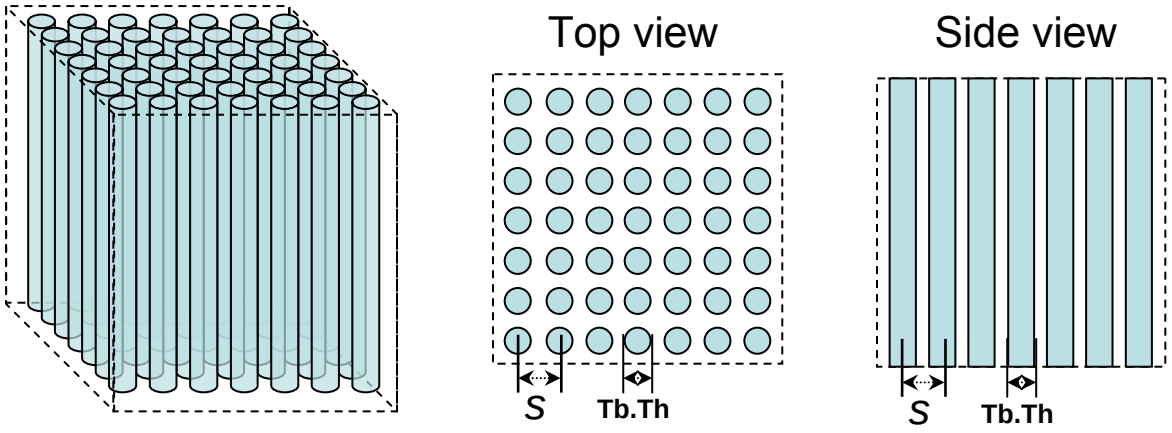

Figure 4-3 The wire model. Its top view and side view are also shown.

The diameter of the wires corresponds to the trabeculae thickness (Tb.Th). The reported mean trabeculae diameter for the human humerus and femur ranges from 70 up to 350 μm (Swartz, Parker et al. 1998), and for human calcaneus it is 127 μm (Ulrich, van Rietbergen et al. 1999).

According to Wear (Wear 2005), the trabecular spacing (s) is the distance between the centers of two adjacent wires, which is given by :

$s = \text{Tb.Sp} + \text{Tb.Th}$,

where Tb.Sp stands for the trabecular separation, and Tb.Th the trabecular thickness. The reported mean trabecular separation of human calcaneus is 684 μm (Ulrich, van Rietbergen et al. 1999), resulting in an averaged trabecular spacing of 811 μm (127 μm + 684 μm = 811 μm).

The porosity of this wired phantom is given by:

$$\beta = 1 - \frac{\pi(\text{Tb.Th}/2)^2}{s^2},$$

while $\frac{\pi(\text{Tb.Th}/2)^2}{s^2}$ is also defined as the volume fraction (VF) in some literatures.

Since the porosity (β) of the wire model is controlled by both the trabecular spacing (s) and trabecular thickness (Tb.Th), the effects of these two parameters were analyzed independently. Firstly, to study the effect of trabecular spacing, the trabecular thickness was set to be 0.2 mm, which is about the average of the reported values for human cancellous bone (Swartz, Parker et al. 1998). The trabecular spacing, s, changed from 0.45 mm to 1.0 mm, with an increment of 0.05 mm. The corresponding porosity decreases as the trabecular spacing increases (Table 4-2).

Table 4-2 Properties of the wired model with fixed trabecular thickness.

Tb.Th = 0.2 mm							
s (mm)	0.45	0.5	0.55	0.6	0.65	0.7	0.75
Porosity	84.49%	87.43%	89.61%	91.27%	92.56%	93.59%	94.41%
s (mm)	0.8	0.85	0.9	0.95	1		
Porosity	95.09%	95.65%	96.12%	96.52%	96.86%		

Secondly, to study the effect of trabecular thickness, the trabecular spacing was set to be 0.8 mm according to the previously reported mean value of 811 μm for human calcaneus (Wear 2005), and the trabecular thickness varied from 0.075 mm to 0.4 mm. This thickness range covered the reported mean trabeculae diameter for the human humerus and femur ranging from 70 up to 350 μm (Swartz, Parker et al. 1998). The resulted porosity increased accordingly to the trabecular thickness (Table 4-3). For fixed trabecular thickness or trabecular spacing, only a small range of porosity could be covered (> 80 %) (Table 4-2 and 4-3).

Table 4-3 Properties of the wired model with fixed trabecular spacing.

s = 0.8 mm							
Tb.Th (mm)	0.075	0.01	0.125	0.15	0.175	0.2	0.225
Porosity	99.31%	98.77%	98.08%	97.24%	96.24%	95.09%	93.79%
Tb.Th (mm)	0.25	0.275	0.3	0.325	0.35	0.375	0.4
Porosity	92.33%	90.72%	88.96%	87.04%	84.97%	82.74%	80.37%

4.2.2 Simulation of ultrasound transducers

The ultrasound transducer simulated here was a concave (focusing) transducer, which had an aperture diameter (l) of 1 cm and focal distance (z_f) of 5 cm. According to literature (Goodman 1968; Wear 2004), for the concave transducer with a circular aperture, the intensity at the focal plane follows the Franhofer diffraction pattern given by:

$$I(x) = \left(\frac{kl^2}{8z}\right)^2 \left[2\frac{J_1(klx/2z)}{klx/2z}\right]^2,$$

where J_1 is the Bessel function of the first kind and first order, $k = 2\pi\lambda$ is the wave number (λ is the wavelength), x is the lateral dimension, and z is the distance away from the aperture. The half width half maximum (HWHM) of $I^2(x)$ of the ultrasound beam is approximated by:

$$\text{HWHM} \approx 0.37zc/(lf),$$

where c is speed of sound and f the frequency. For instance, for a transducer with center frequency of 5 MHz, its HWHM is 0.55 mm.

Fig 4-4 shows the details of the concave (focusing) transducers which have center frequencies of 0.5 MHz, 1 MHz, 2.25 MHz, 3.5 MHz, 5 MHz and 10 MHz, respectively. In this study, only the 2.25 MHz, 3.5 MHz and 5 MHz transducers were simulated. Transducers with these frequencies were also used in practical experiments later.

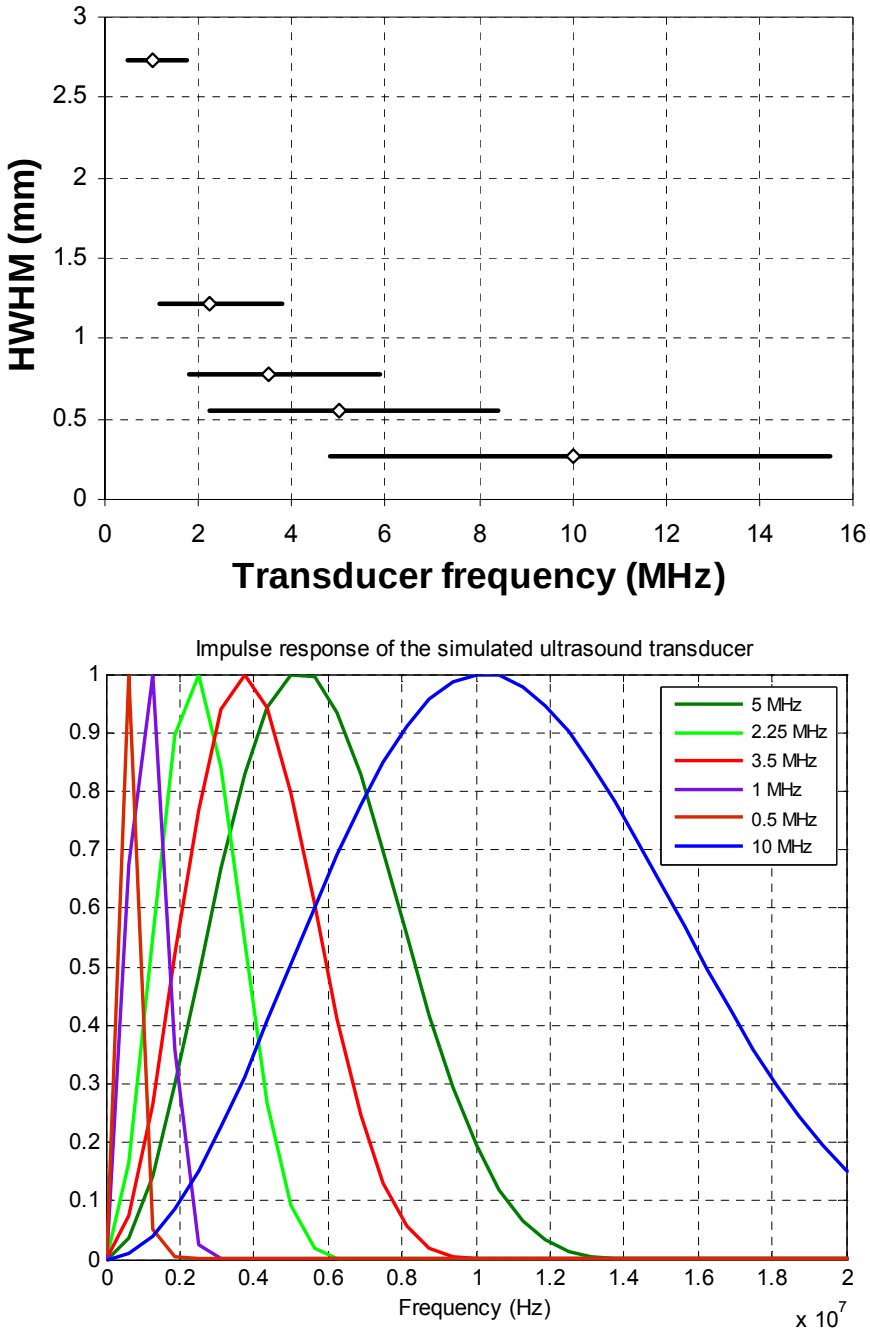

Figure 4-4 Details of the simulated ultrasound transducers.

A) Impulse responses of the transducers with different center frequency;
B) 3dB frequency bandwidth (determined from A) and HWHM of all the transducers.

4.2.3 Backscattering analysis

To study the interaction between ultrasonic waves and the trabecular network of cancellous bone, the cellular model was adopted firstly. The cellular model was described in detail previously. Pore separation, as the distance between two adjacent pores, was fixed to be 1 mm. As the diameter varied from 0.1 mm to 0.55 mm, the corresponded porosity increased from 3 % to 95 % (Table 4-1). Trabecular orientation, referring to the angle between the incident wave and the aligned direction of the pores changed from 0º to 90º with an increment of 10º. The ultrasound transducer was simulated with a center frequency of 2.25 MHz, 3.5 MHz and 5 MHz, respectively.

The transducer was set to be performed in the pulse-echo mode. The sampling frequency was 80 MHz. The amplitude of the backscattered (reflected) signals and the Broadband ultrasound backscatter coefficient (BUB, in dB) were obtained. The BUB was calculated as demonstrated in Chapter 2. First, a time gate of 256 samples was isolated to select the data from a ROI inside of the phantom. The center of the window was set at the focal point of the transducer, and the duration of the data window is 3.2 μs corresponding to the 256 samples at the sampling frequency of 80 MHz. The ultrasound velocity was set to be 1480 m/s as it propagates in water, resulting in spatial extent of the gated data to be approximately 2.4 mm, which was definitely within the simulated phantom. Then the Fourier transform of the gated signal from this ROI was taken and its power spectrum was obtained. The estimated amplitude of the backscattered signal was characterized by the peak value of the power spectrum. The estimated backscattering coefficient was computed by the log-spectral subtraction of the calibration spectrum from the average of the acquired data spectrum to

deconvolute the frequency response of the measuring system. The calibration spectrum (reference signal) was obtained by reflecting an ultrasound pulse from a standard reflecting target, which was a single scatterer locating at the focal point of the transducer in this simulation. The averaging of signal spectrum from all different ROIs, in terms of integration, was to remove pure statistical variations due to the random phase shift introduced by each scattering trabeculae. Finally, the BUB of each phantom was obtained as the average value of the estimated backscattering coefficients over the frequency bandwidth of the transducer. The ROIs were chosen to be within the phantom while un-overlapped to each other. The number of ROIs depends upon the ultrasound frequency being used. Transducers with lower central frequency have wider HWHM as shown in figure 4-4, therefore, less ROIs can be picked in the measurement.

For each transducer frequency, the measurements were repeated four times. The resulted BUBs were processed in Microsoft® Excel 2002 (Microsoft Corporation, Redmond, WA, USA) for statistic analysis. A linear regression was applied to the averaged results for each frequency and each trabecular orientation. Standard deviation between the repeated measurements, and the R^2 of the linear regression were calculated

4.2.4 Dependence of backscattering on trabecular microarchitecture

A. Results of the cellular model

Figure 4-5, 4-6, and 4-7 show the change of the BUB with the radius of the pores of the cellular model for different trabecular orientation while using the transducers of 2.25 MHz, 3.5 MHz and 5 MHz, respectively. From these results it can be seen that the BUB decreased

as the pore size increased when the trabecular direction was not normal to the wave propagation direction (90º), i.e., when the trabecular orientation vector had a component along the wave propagation direction. This relationship could be approximated by a linear regression (averaged R^2 = 0.73 for 2.25 MHz, 0.76 for 3.5 MHz, and 0.81 for 5 MHz). However, when the trabecular lied perpendicular to the wave direction, the change was not obvious for all frequencies.

Since the porosity increases with the pore size monotonically, similar strong relationship was revealed between the BUB and the porosity of the cellular models, as shown in figure 4-8, 4-9 and 4-10. The porosity change could explain an average of 84% of the variance of the BUBs for 2.25 MHz transducer (Figure 4-8), 86% for 3.5 MHz (Figure 4-9) and 91% for 5 MHz (Figure 4-10). The correlation between the porosity and the ultrasound backscattering was stronger than that between the pore radius and the ultrasound backscattering.

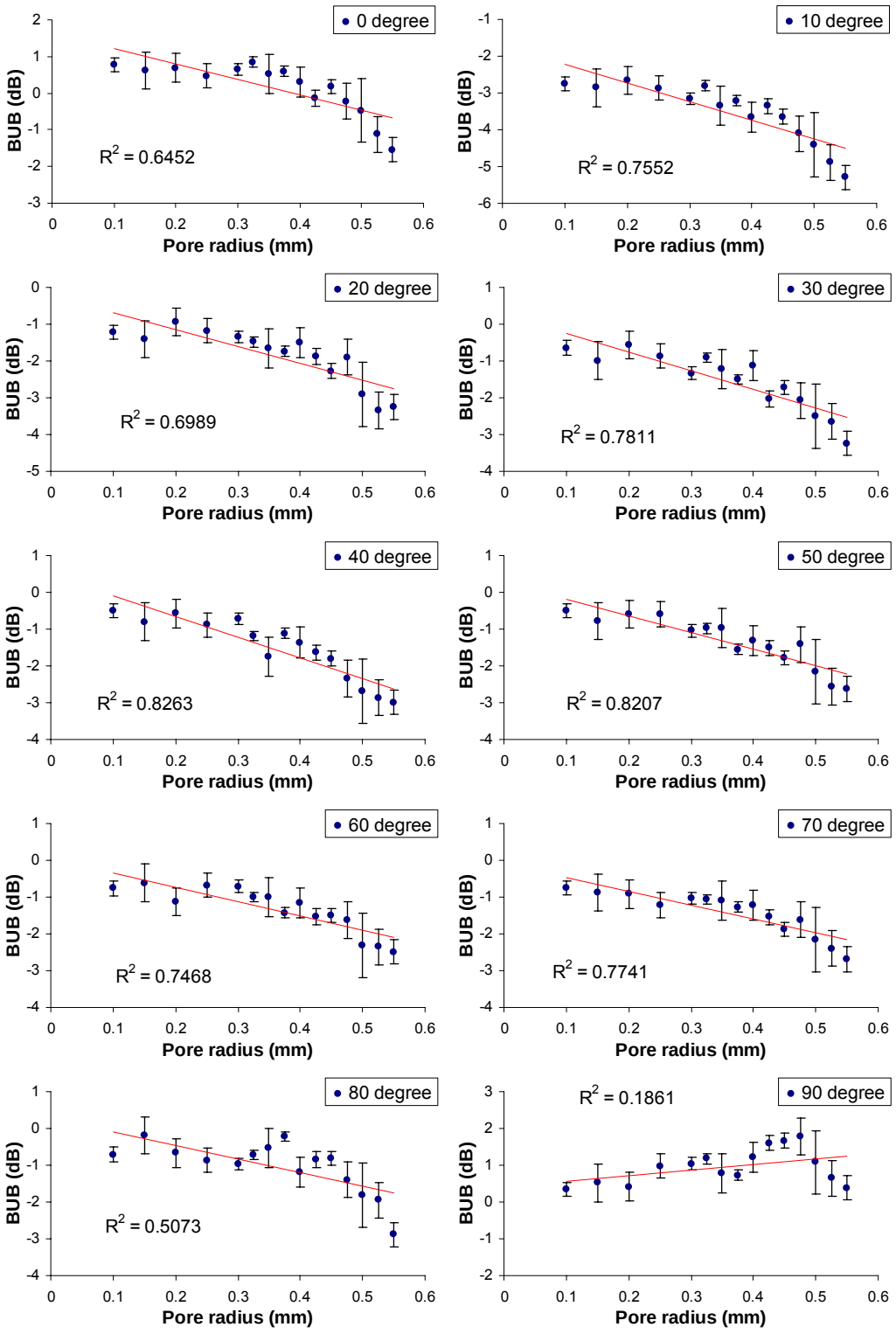

Figure 4-5 BUB vs. pore size of the cellular model with different trabecular orientation using 2.25 MHz ultrasound transducer. The linear regression is also shown (red line).

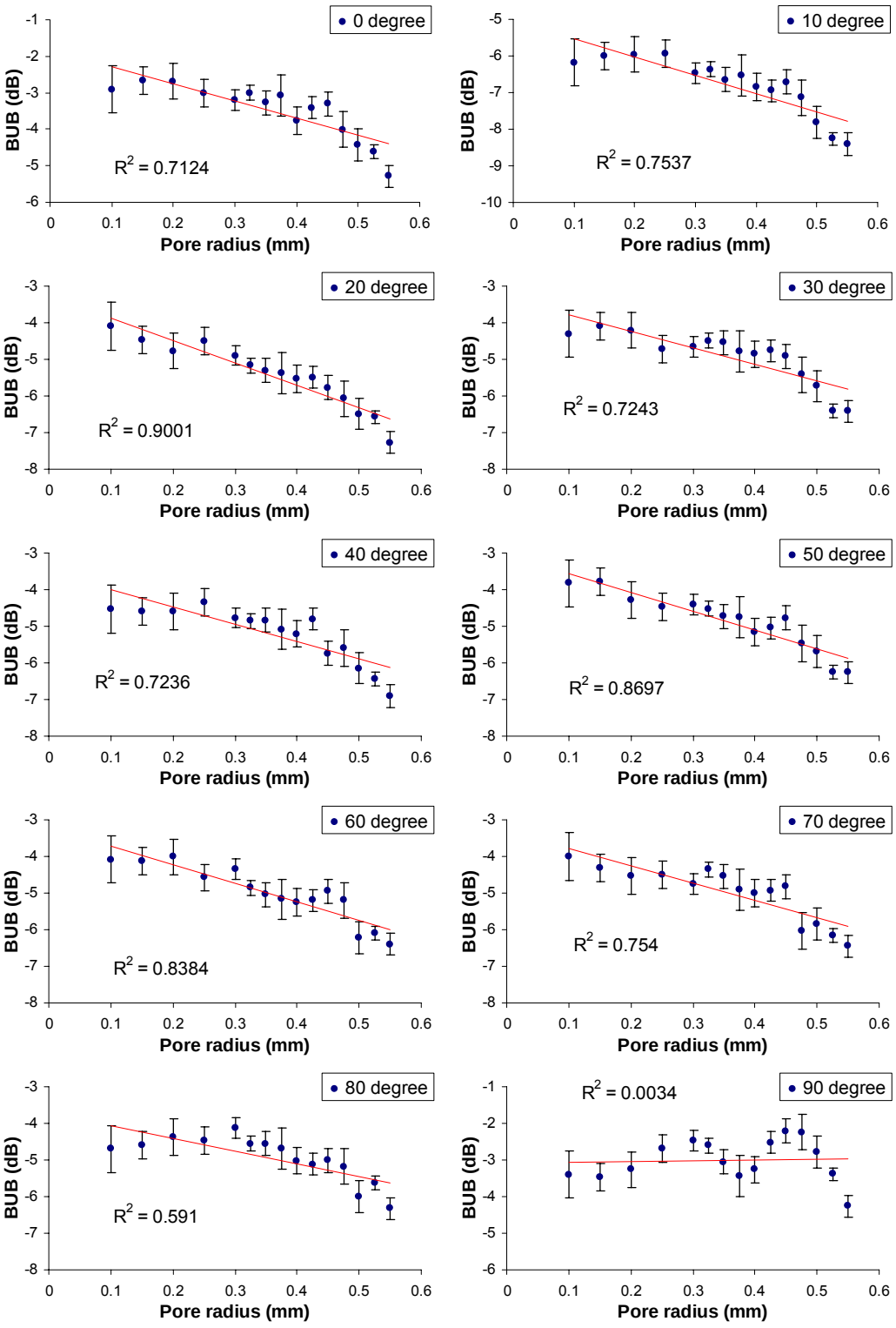

Figure 4-6 BUB vs. pore size of the cellular model with different trabecular orientation using 3.5 MHz ultrasound transducer. The linear regression is also shown (red line).

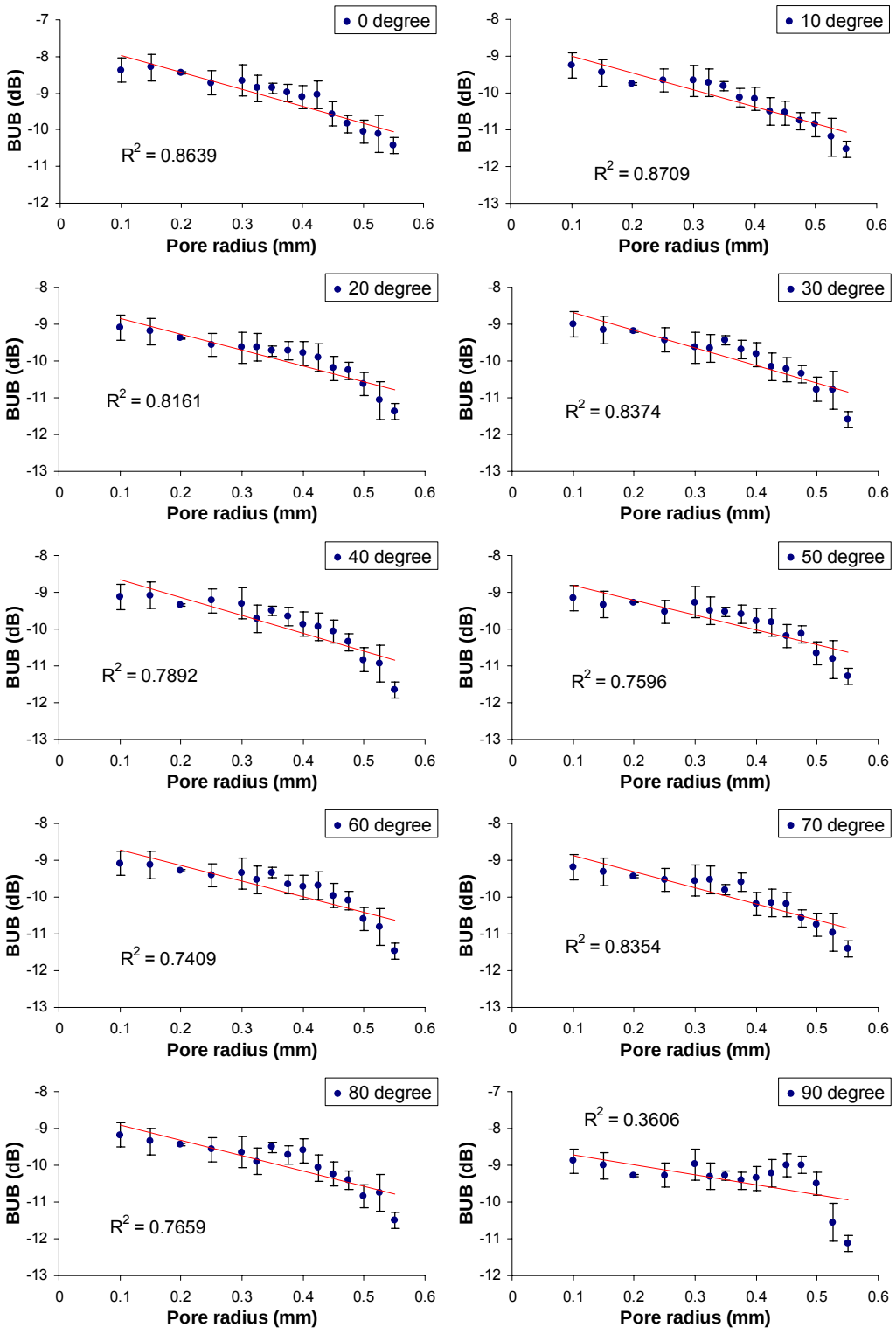

Figure 4-7 BUB vs. pore size of the cellular model with different trabecular orientation using 5 MHz ultrasound transducer. The linear regression is also shown (red line).

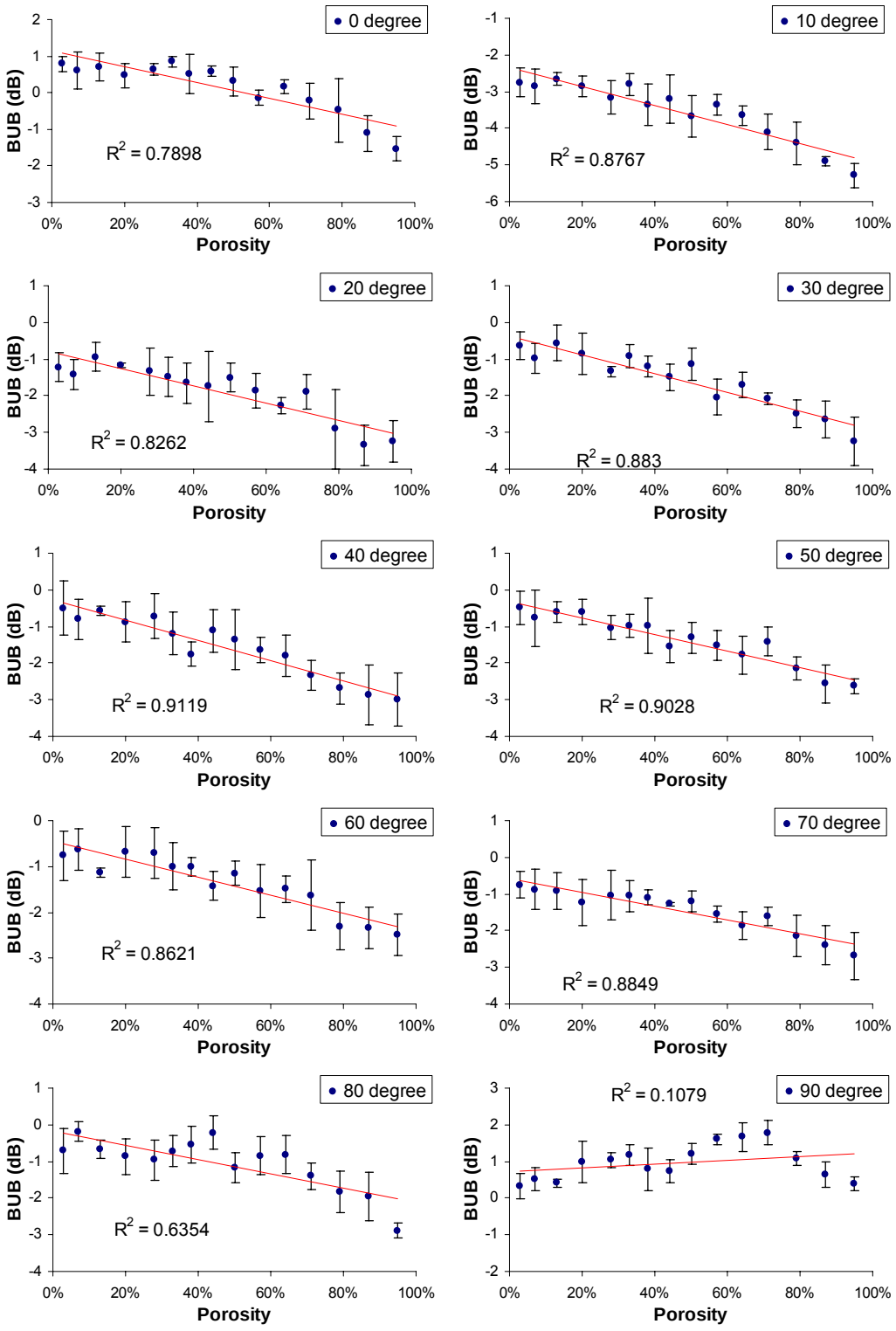

Figure 4-8 BUB vs. porosity of the cellular model with different trabecular orientation using 2.25 MHz ultrasound transducer. The linear regression is also shown (red line).

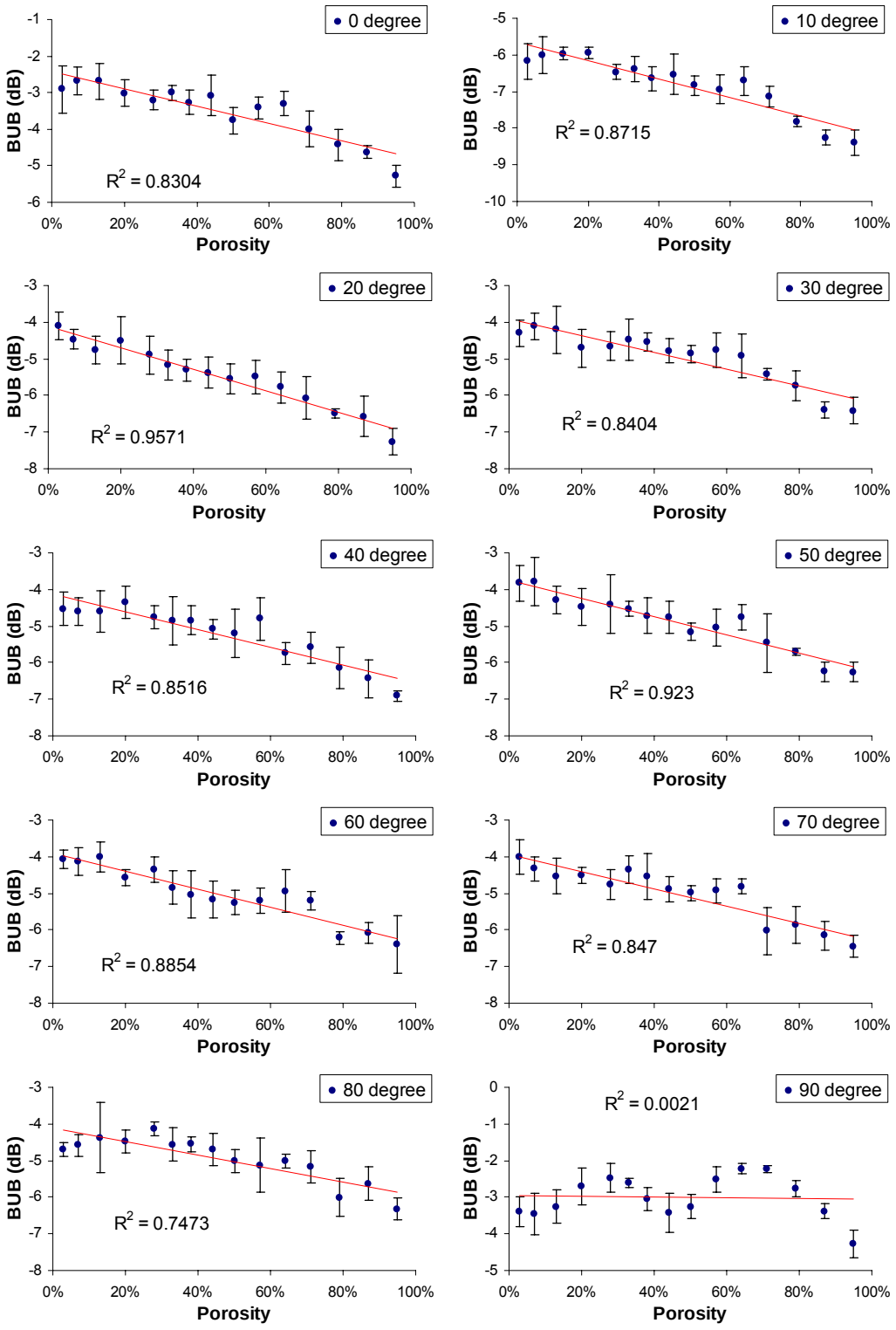

Figure 4-9 BUB vs. porosity of the cellular model with different trabecular orientation using 3.5 MHz ultrasound transducer. The linear regression is also shown (red line).

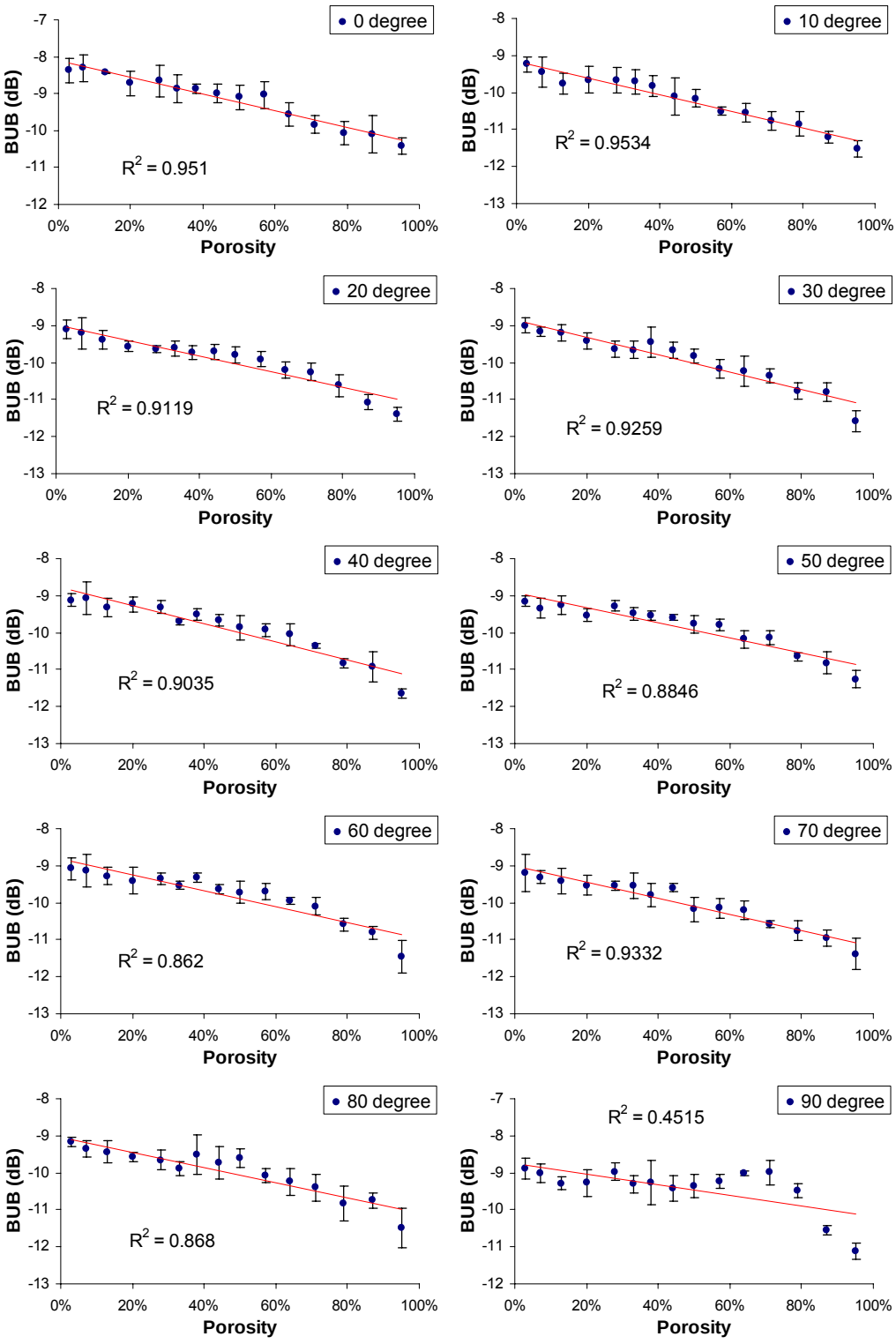

Figure 4-10 BUB vs. porosity of the cellular model with different trabecular orientation using 2.25 MHz ultrasound transducer. The linear regression is also shown (red line).

Considering the similarity of the trend of BUB changing with porosity for different trabecular orientations along the wave propagating direction, the data were averaged in terms of trabecular orientation (0º to 80º) and the results were shown in figure 4-11. The averaged BUB showed strong correlation with the porosity at all frequencies: R^2 equals to 91% for 2.25 MHz, 94% for 3.5 MHz and 93% for 5 MHz. The changing rate of the BUB with the porosity was -2.27 for 2.25 MHz, 2.41 for 3.5 MHz and 2.21 for 5 MHz; there's no significant difference between the slopes for different transducer frequencies ($P < 0.001$).

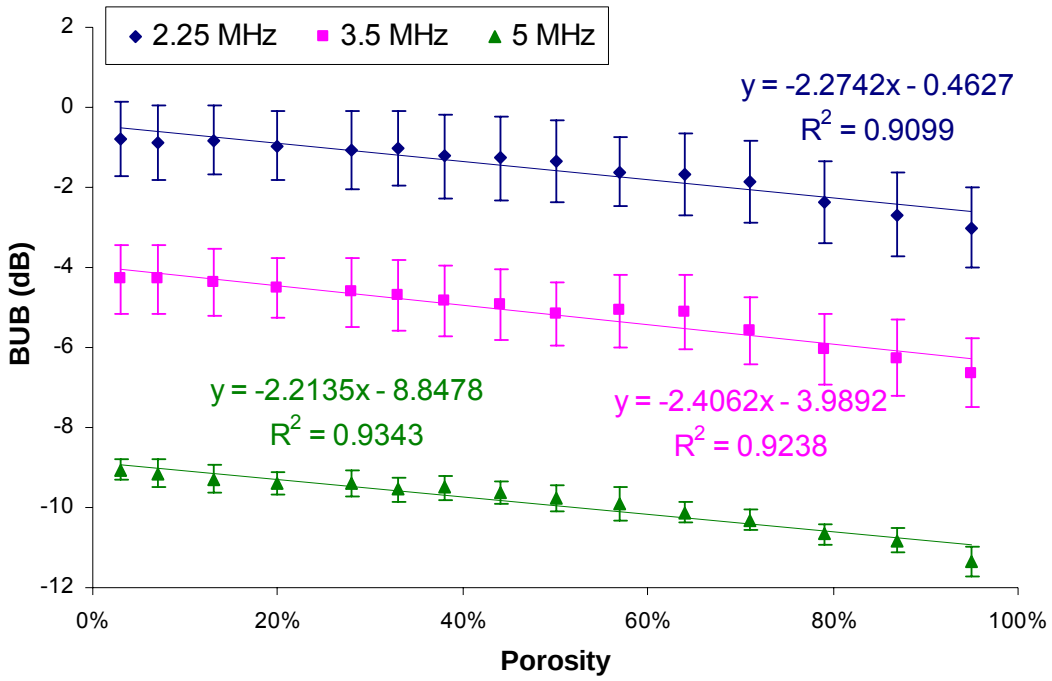

Figure 4-11 The linear regression of averaged BUBs over different trabecular orientations (0º to 80º) at different frequencies for the cellular model.

As demonstrated previously, smaller transducer frequency corresponds to higher HWHM (half width half maximum), so considering the pore/wire size (diameter), more scatters are involved in the plane wave that has lower frequency. Therefore, the BUB as an integration parameter of the backscatter signals is higher for lower frequency and vice versa. In addition, according to the simulation design, the ROIs were chosen to be un-overlapped to each other. Therefore, for a model of given size, the number of available ROIs is less for smaller transducer frequencies. As a result, the BUB is averaged for fewer times so that the variance, as indicated by the error bars in figure 4-11, is bigger for smaller transducer frequencies.

Figure 4-12 shows the change of BUB along with the trabecular orientation for different porosities. For all the porosities and all the frequencies that have been simulated, there was an immediate drop of BUB when the trabecular orientation was no longer in the direction of wave propagation, referring to the difference between the trabecular orientation of 0º and 10º. As the angle between trabecular orientation and wave direction increased, the BUB also increased until the angle reached about 30º. Then the BUB remained unchanged when the angle was between about 30º and 80º. This should be explained by the effect of rotating the phantom that changes the effective porosity that the wave has been encountered, or in another word, the projected view of a layer of the cellular phantom with some thickness onto the plane normal to the wave propagating direction.

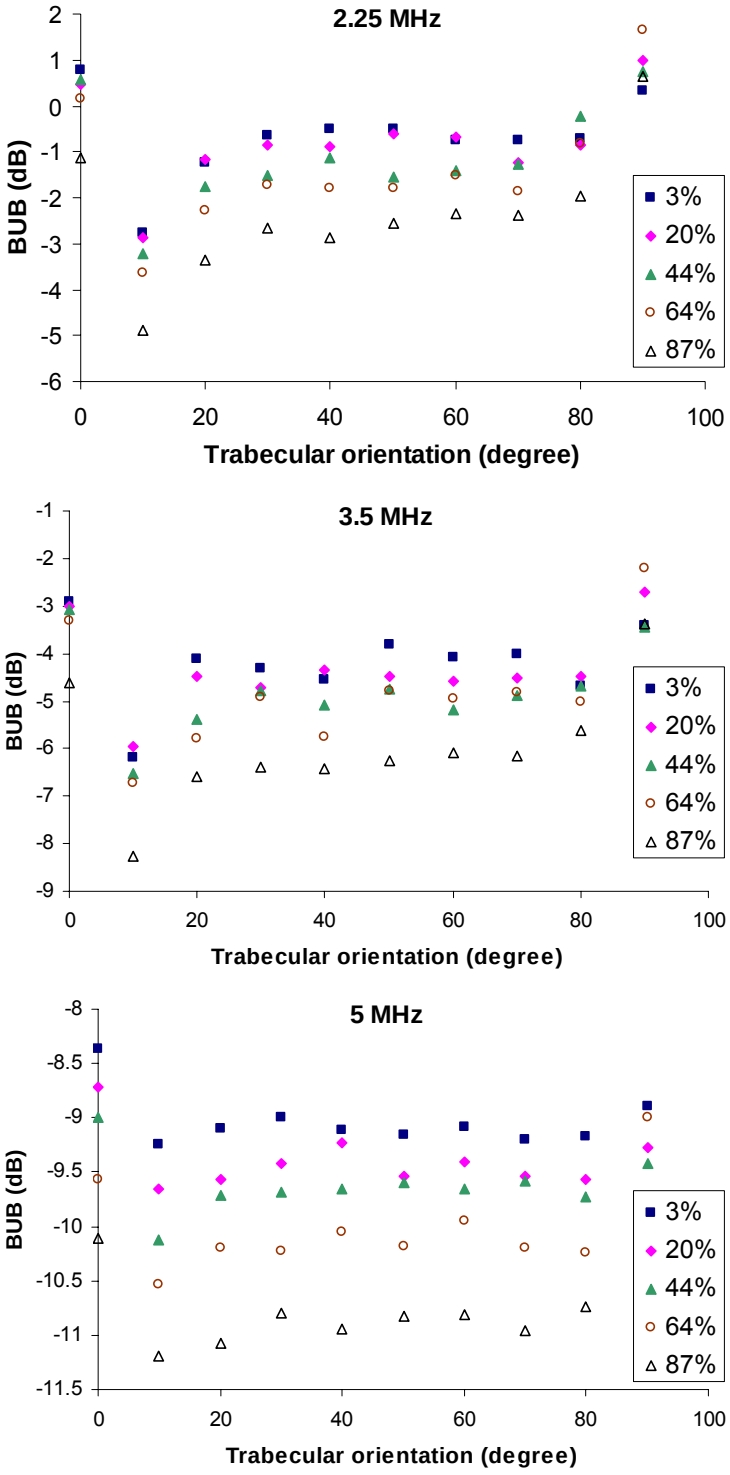

Figure 4-12 The linear regression of averaged BUBs of all trabecular orientations at different frequencies for the cellular model.

B. Results of the wire model

To analyze the effects of trabecular spacing (*s*) and trabecular thickness (Tb.Th) independently, firstly the trabecular thickness was set to be the reported mean value of human cancellous bone (Tb.Th = 0.2 mm) and the trabecular spacing was subject to change from 0.45 mm to 1 mm (Table 4-2). Trabecular orientation, referring to the angle between the incident wave and the aligned direction of the pores changed from 0º to 90º with an increment of 10º. The ultrasound transducer was simulated with a center frequency of 2.25 MHz, 3.5 MHz and 5 MHz, respectively. Other simulation parameters and data analysis method were the same to the cellular model simulation.

Figure 4-13, 4-14 and 4-15 show the change of the BUB with the trabecular spacing (*s*) of the wire model for different trabecular orientation using the transducers of 2.25 MHz, 3.5 MHz, and 5 MHz, respectively. This change could be well approximated by a linear regression (average R^2 = 0.84 for 2.25 MHz, 0.89 for 3.5 MHz and 0.91 for 5 MHz) for all the trabecular orientations except for 90º, which was the extreme case that the incidence of the ultrasonic wave was perpendicular to the alignment of the trabecular.

With fixed trabecular thickness, the porosity of the wire model decreasing monotonically with the trabecular spacing. So the BUB also decreases as a function of porosity as seen in figure 4-16, 4-17 and 4-18. Although the decrease is more dramatic at very high porosity range (β > 95 %), the relationship between porosity and BUB can also be modeled by a linear function except the 90º case, with an average R^2 = 0.79 for 2.25 MHz, 0.87 for 3.5 MHz and 0.87 for 5 MHz.

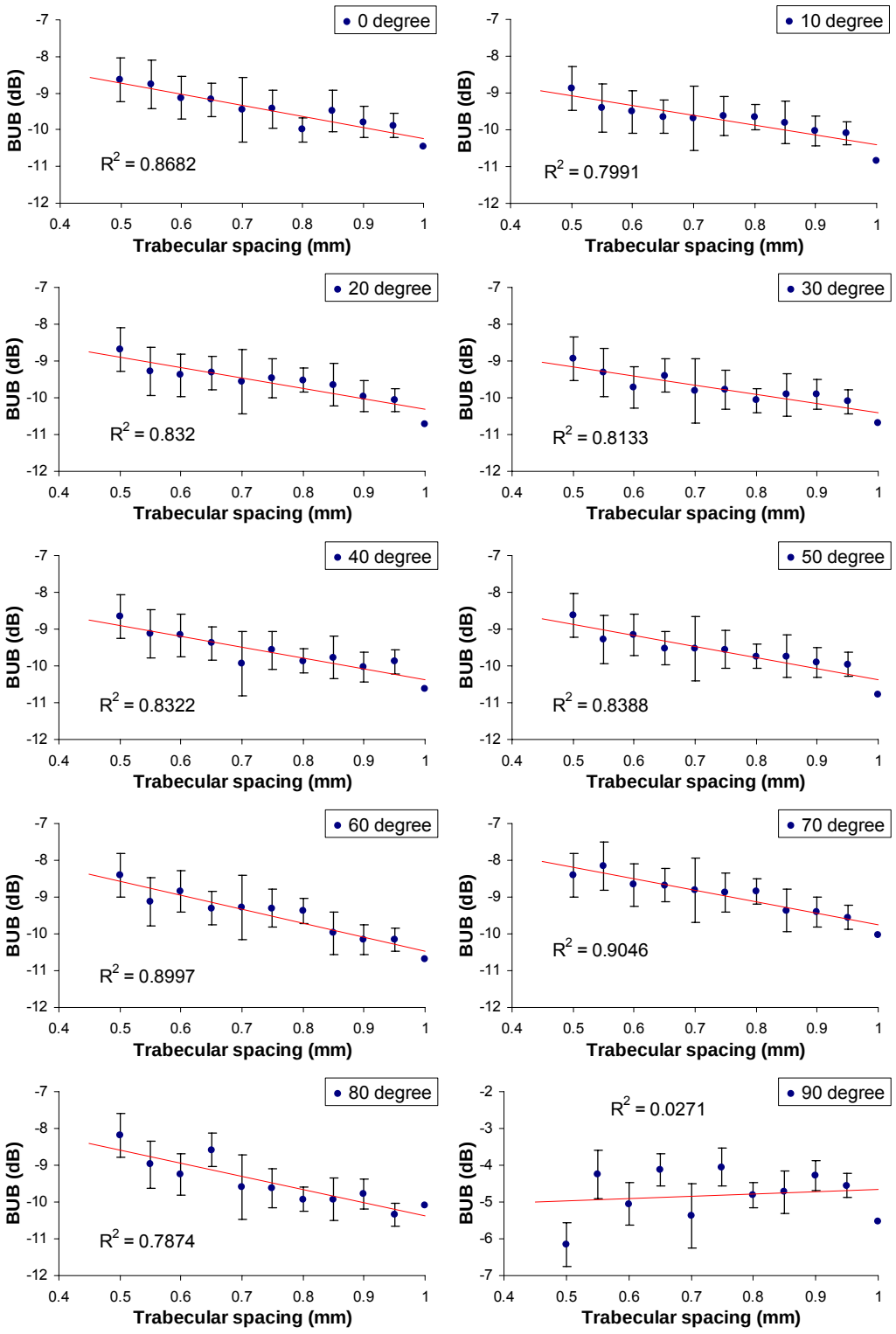

Figure 4-13 BUB vs. trabecular spacing of the wire model at different trabecular orientation using 2.25 MHz ultrasound transducer. Tb.Th = 0.2 mm. Solid line is the linear regression.

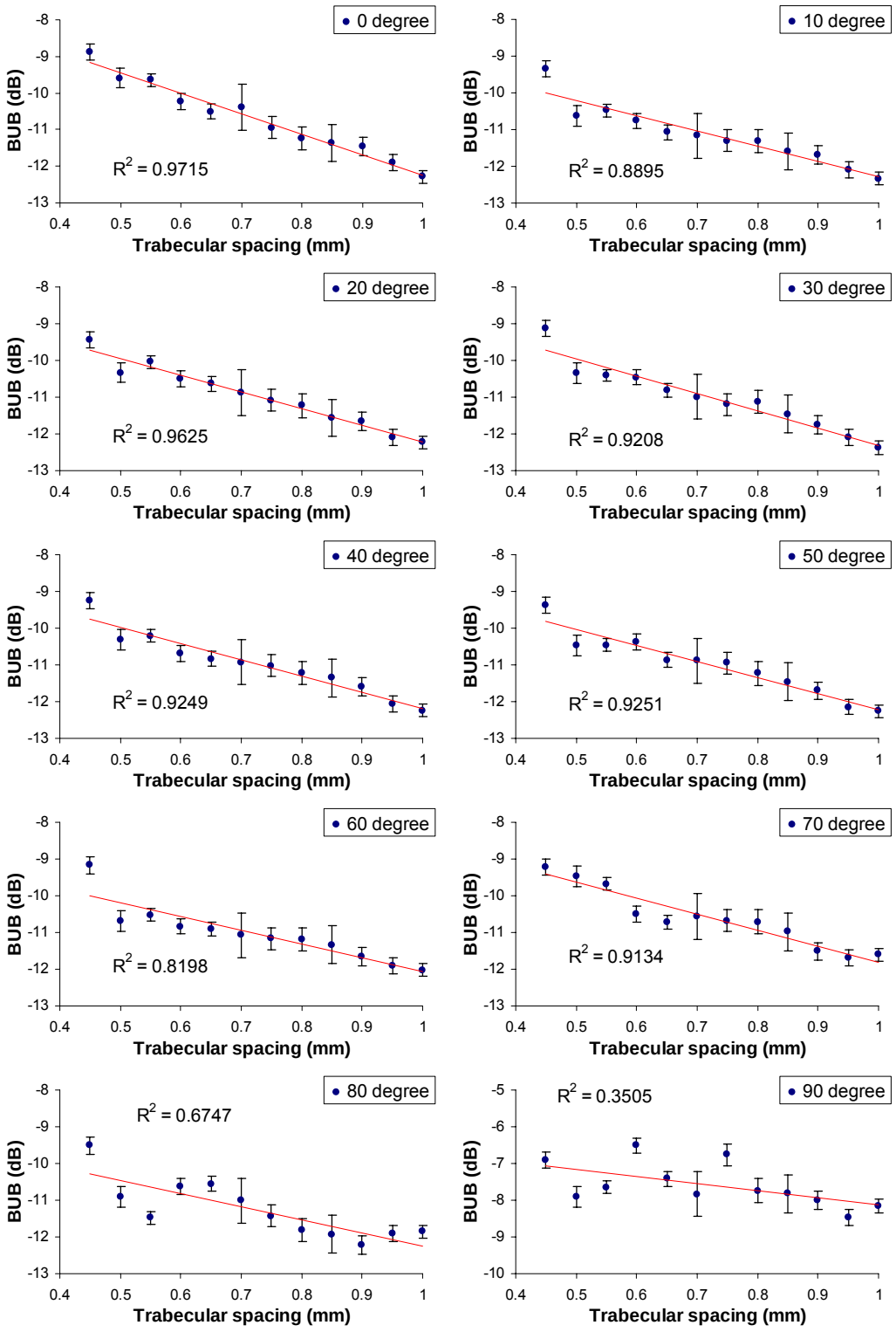

Figure 4-14 BUB vs. trabecular spacing of the wire model at different trabecular orientation using 3.5 MHz ultrasound transducer. Tb.Th = 0.2 mm. Solid line is the linear regression.

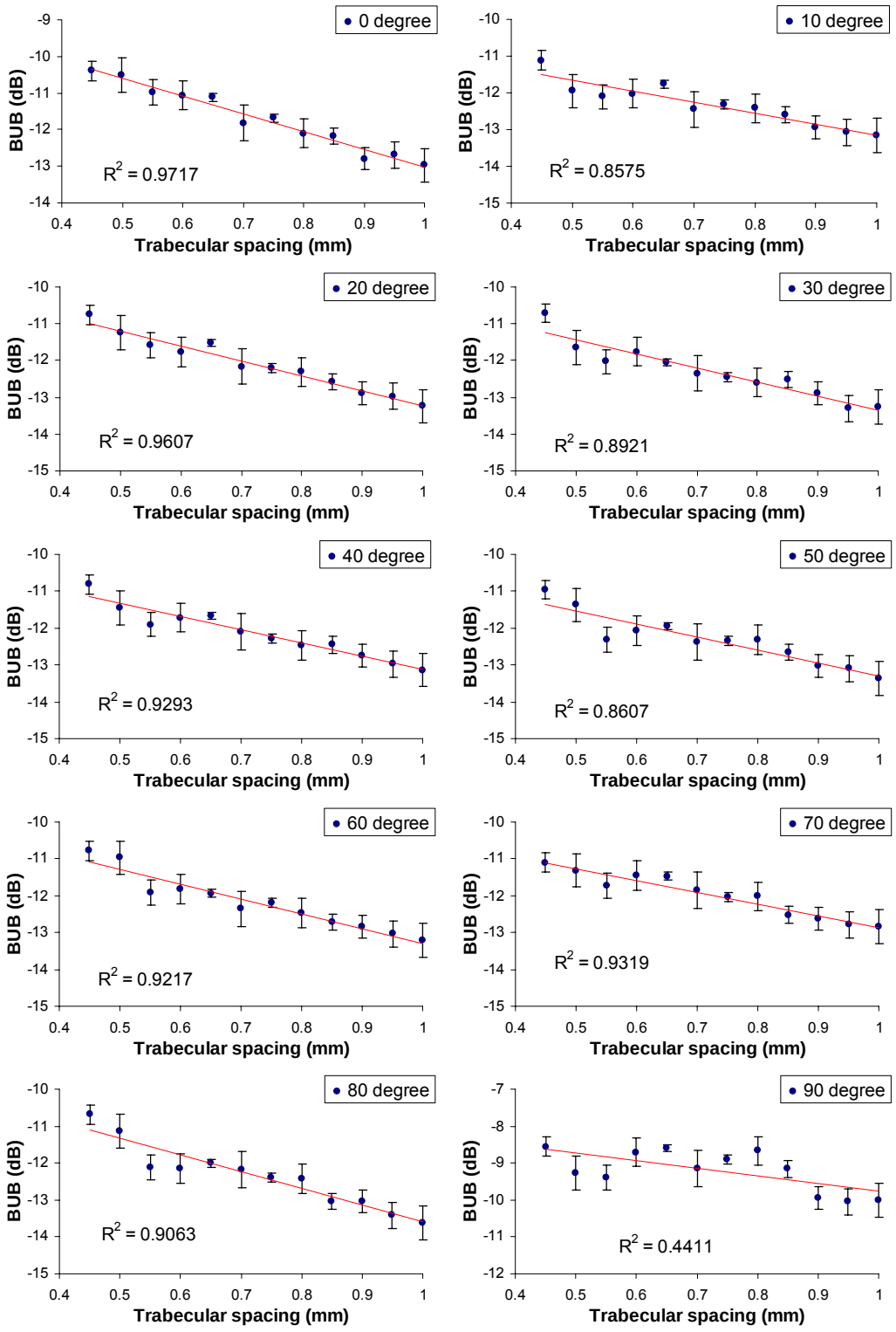

Figure 4-15 BUB vs. trabecular spacing of the wire model at different trabecular orientation using 5 MHz ultrasound transducer. Tb.Th = 0.2 mm. Solid line is the linear regression.

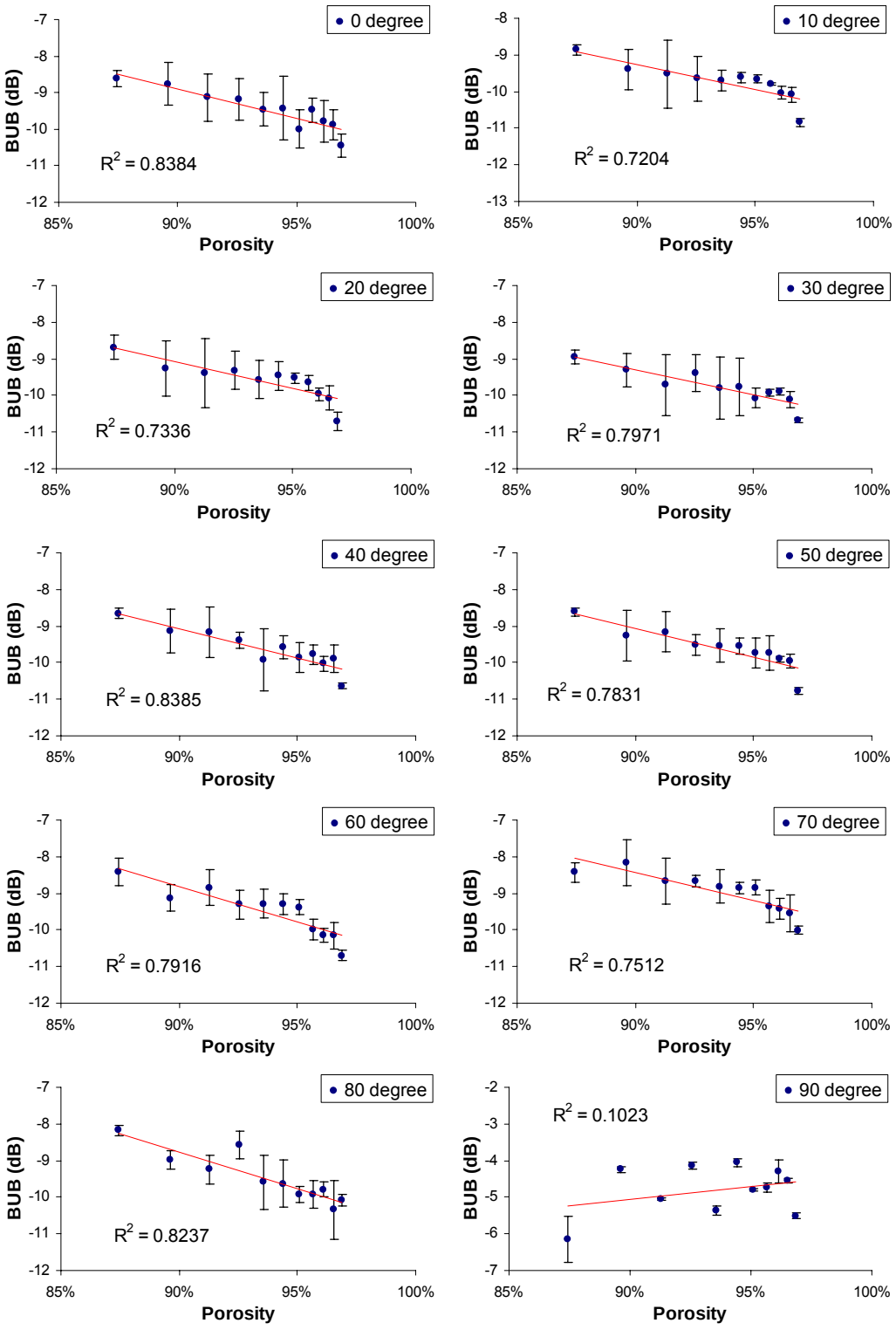

Figure 4-16 BUB vs. porosity of the wire model controlled by *s* for different trabecular orientation using 2.25 MHz ultrasound. Tb.Th = 0.2 mm. Solid line is the linear regression.

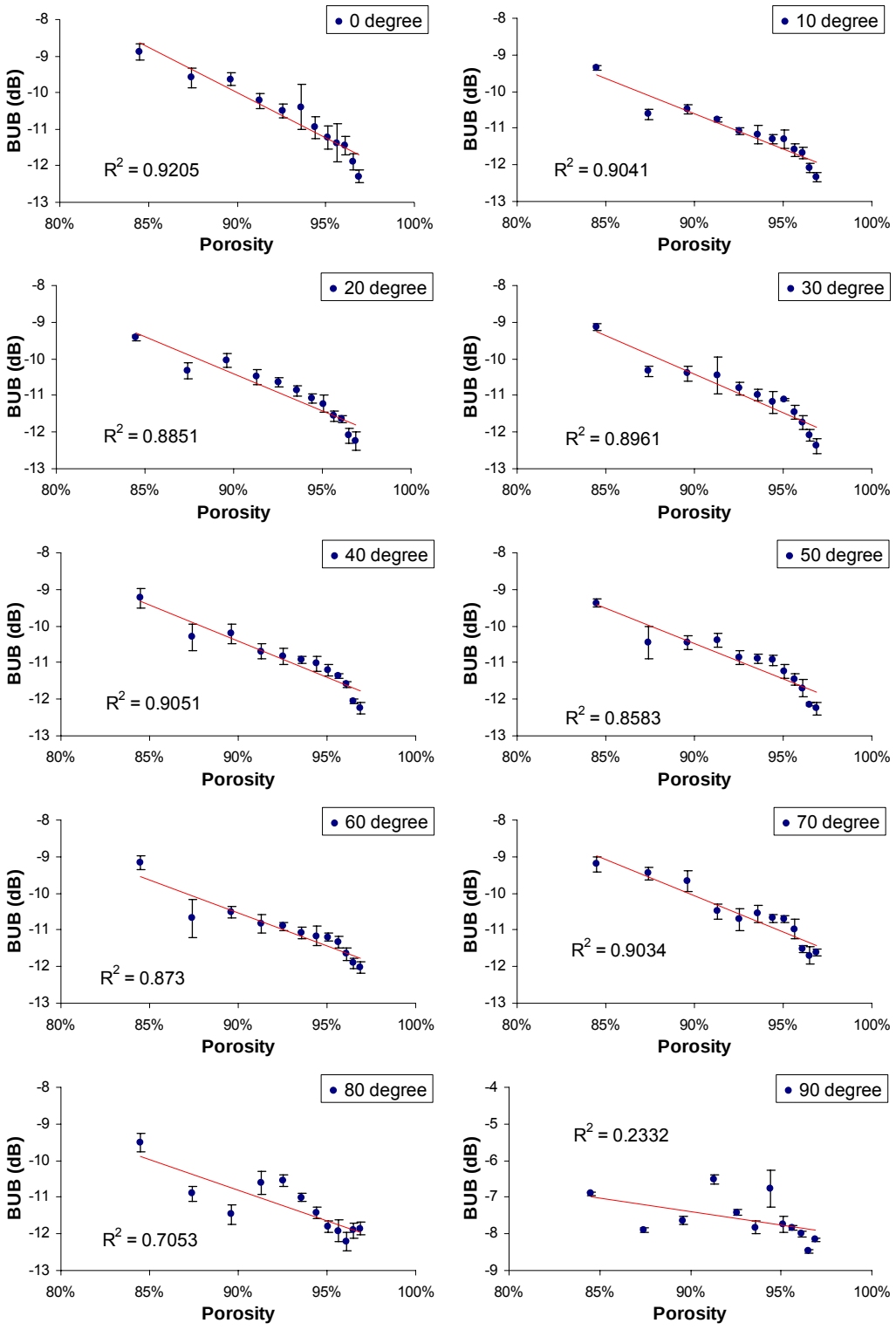

Figure 4-17 BUB vs. porosity of the wire model controlled by *s* at different trabecular orientation using 3.5 MHz ultrasound. Tb.Th = 0.2 mm. Solid line is the linear regression.

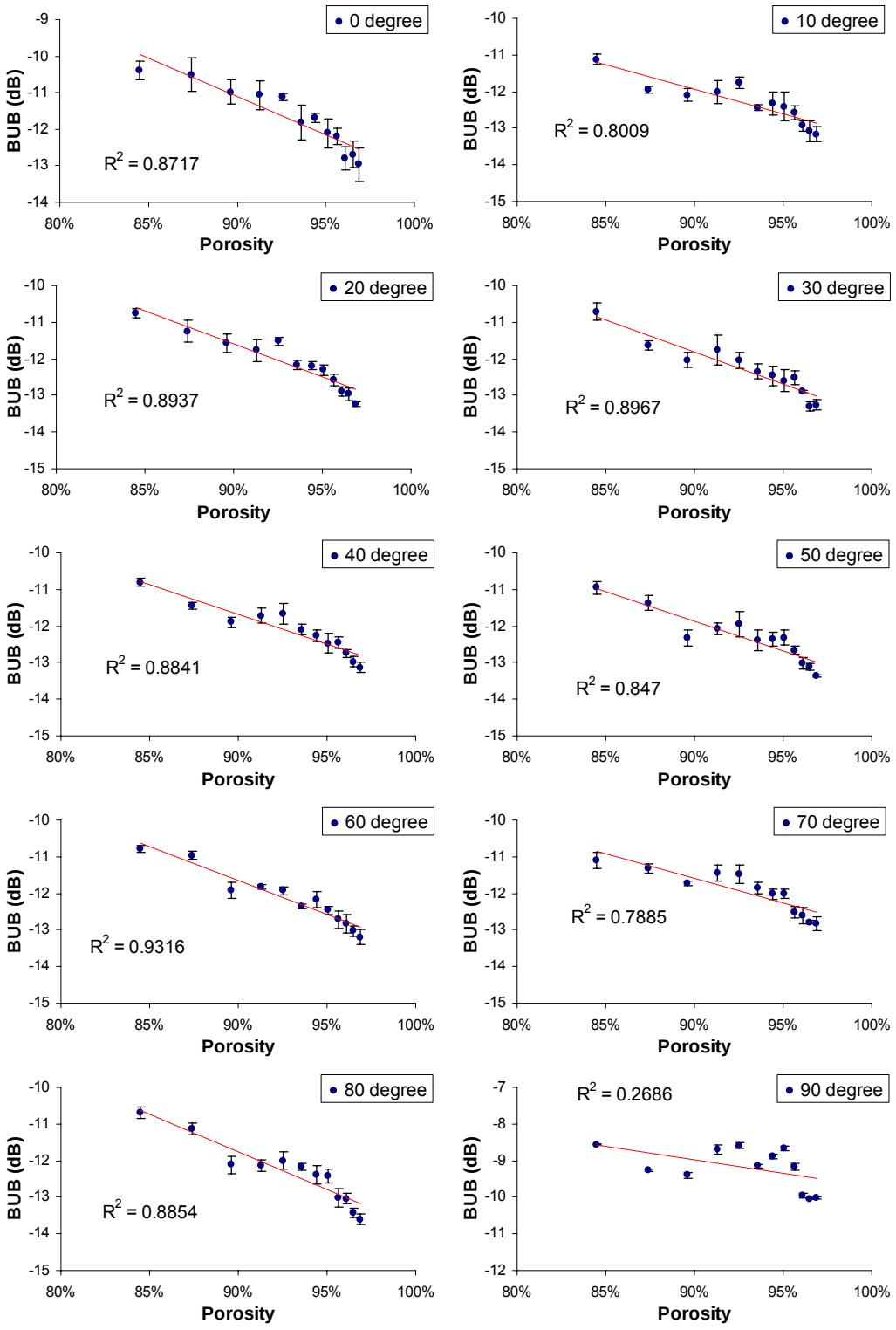

Figure 4-18 BUB vs. porosity of the wire model controlled by *s* at different trabecular orientation using 5 MHz ultrasound. Tb.Th = 0.2 mm. Solid line is the linear regression.

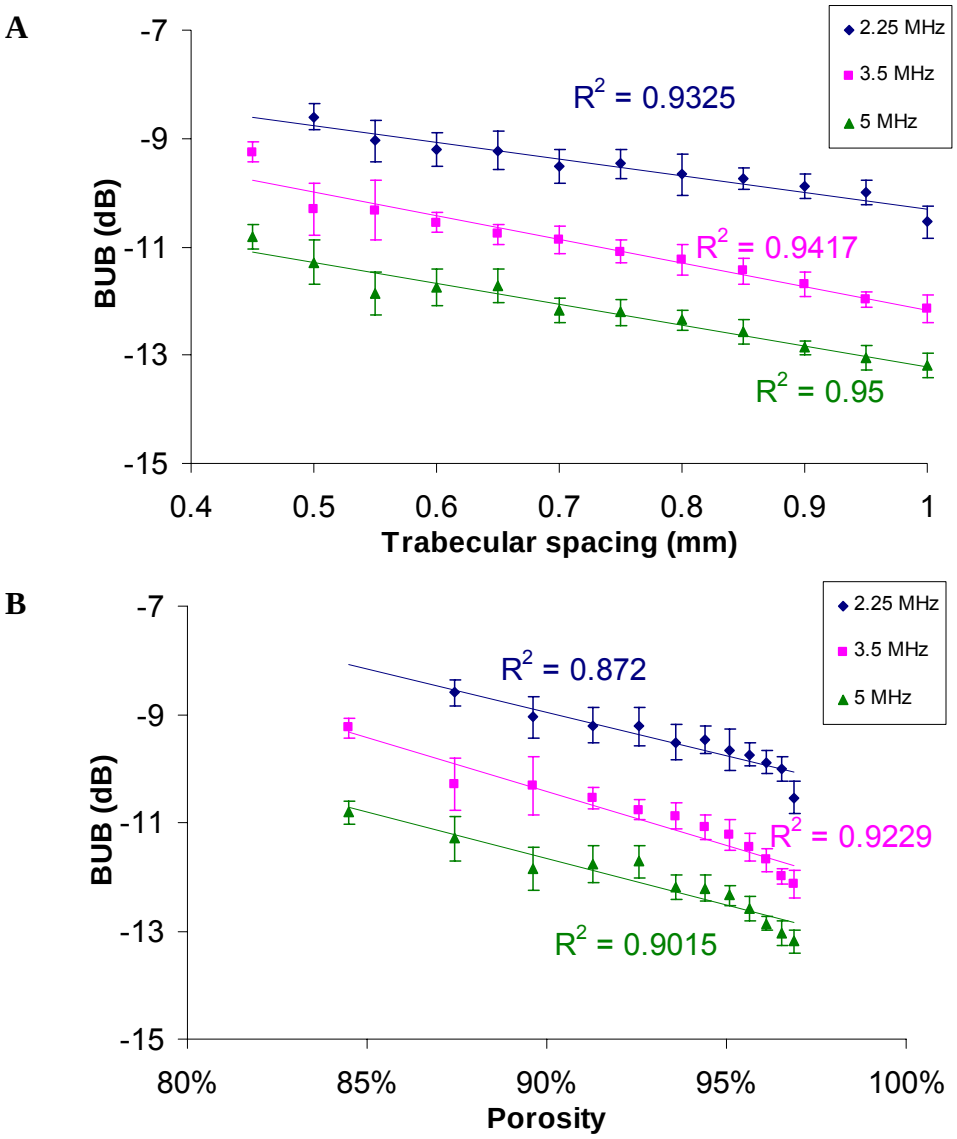

Figure 4-19 The linear regression of trabecular orientation–averaged BUBs at different frequencies as a function of trabecular spacing (A) and porosity of the wire model (B). The trabecular thickness (Tb.Th) is fixed at 0.2 mm.

Figure 4-19 shows the averaged BUB over different trabecular orientations (0º to 80º) with fixed trabecular spacing for the ultrasound frequency of 2.25 MHz, 3.5 MHz and 5 MHz, respectively. The averaged BUB showed a strong linear relationship with trabecular spacing (R^2 = 0.93 for 2.25 MHz, 0.94 for 3.5 MHz and 0.95 for 5 MHz). The trabecular orientation

and ultrasound frequency possess very limited effects on this relationship. In another word, the changing trend of BUB with trabecular spacing was independent of the trabecular orientation and ultrasound frequency.

Then the effect of trabecular thickness was analyzed independently of the trabecular spacing by setting it to be constant. In my study, s = 0.8 mm, which is about the reported average trabecular spacing of 811 μm. The trabecular thickness varied between 0.075 mm to 0.4 mm (Table 4-3). Figure 4-20, 4-21, and 4-22 show the change of BUB with trabecular thickness of the wire model for different trabecular orientation using the transducers of 2.25 MHz, 3.5 MHz, and 5 MHz, respectively. The increase of trabecular thickness had little effect on BUB for smaller angles between trabecular orientation and the wave direction. When the trabecular orientation was perpendicular to the direction of wave propagation (90º), the change of trabecular thickness could explain over 95% of the variance of BUB for 2.25 MHz, 95% for 3.5 MHz and 94% for 5 MHz.

With fixed trabecular spacing, the change of porosity of the wire model resulting from the trabecular thickness also showed little effect on BUB for smaller orientation angles between the trabecular and the wave direction (Figure 4-23, 4-24 and 4-25). Remember the porosity decreases monotonically as the trabecular thickness increases. Consequently, when the trabecular orientation was normal to the direction of wave propagation (90º), the BUB also increased as a function of porosity when the change of porosity was due to trabecular thickness only. The relationship between porosity and BUB at 90º incident angle from trabecular orientation could be modeled by a linear function, with a R^2 of 0.96 for 2.25 MHz, 0.86 for 3.5 MHz and 0.83 for 5 MHz.

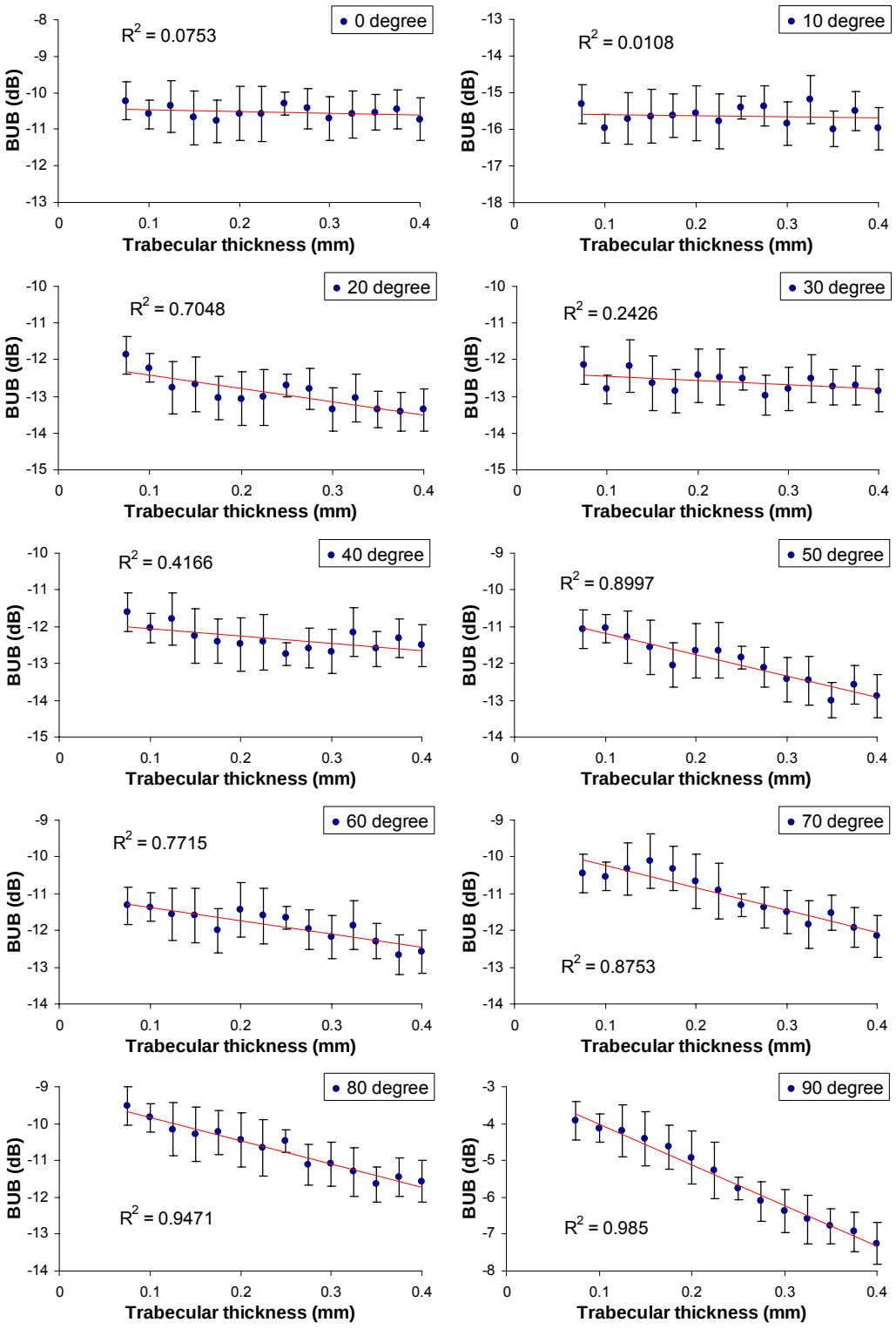

Figure 4-20 BUB vs. different trabecular thickness using 2.25 MHz ultrasound transducer. Trabecular spacing is constant ($s = 0.8$). A linear regression is also shown (red line).

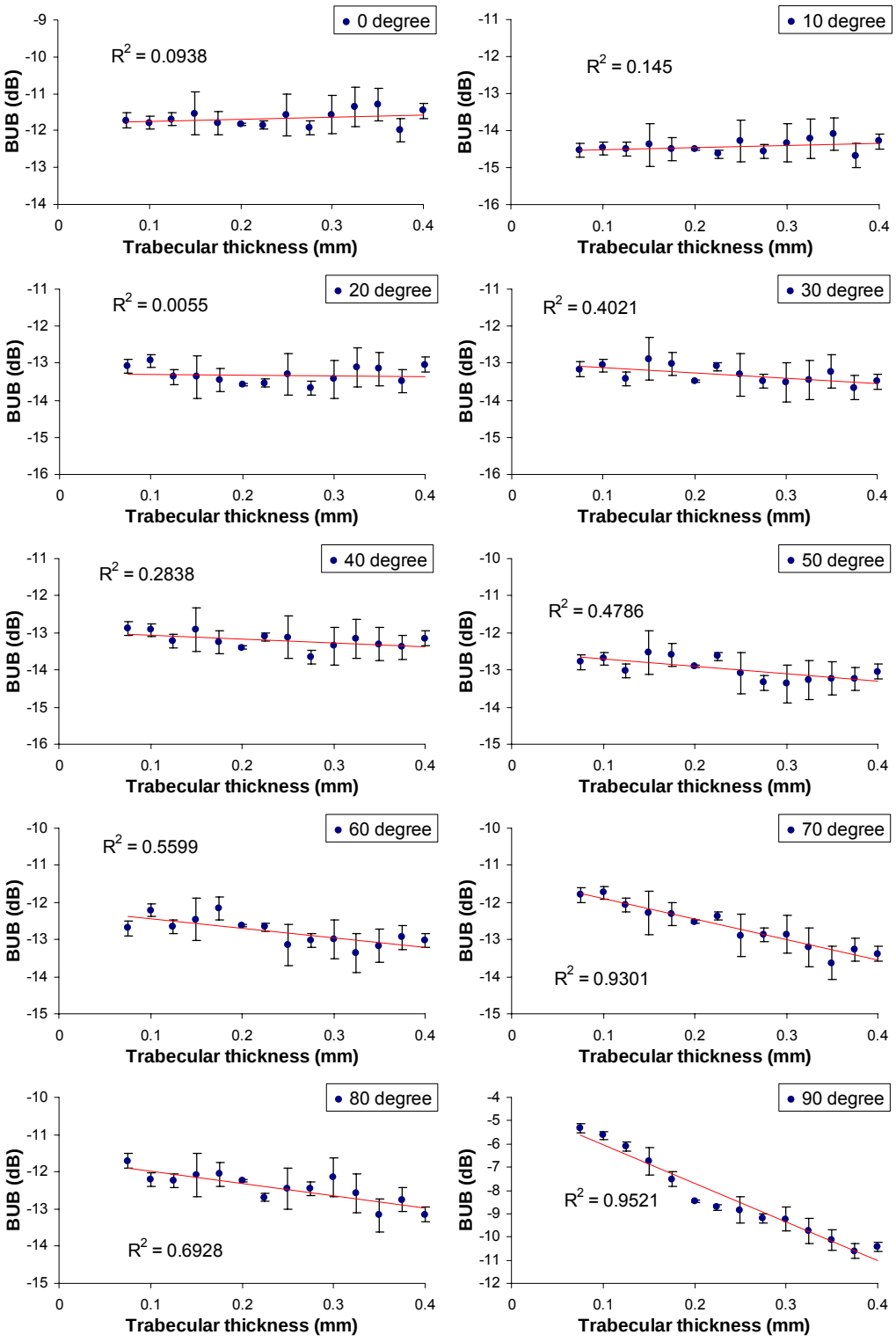

Figure 4-21 BUB vs. different trabecular thickness using 3.5 MHz ultrasound transducer. Trabecular spacing is constant (s = 0.8). A linear regression is also shown (red line).

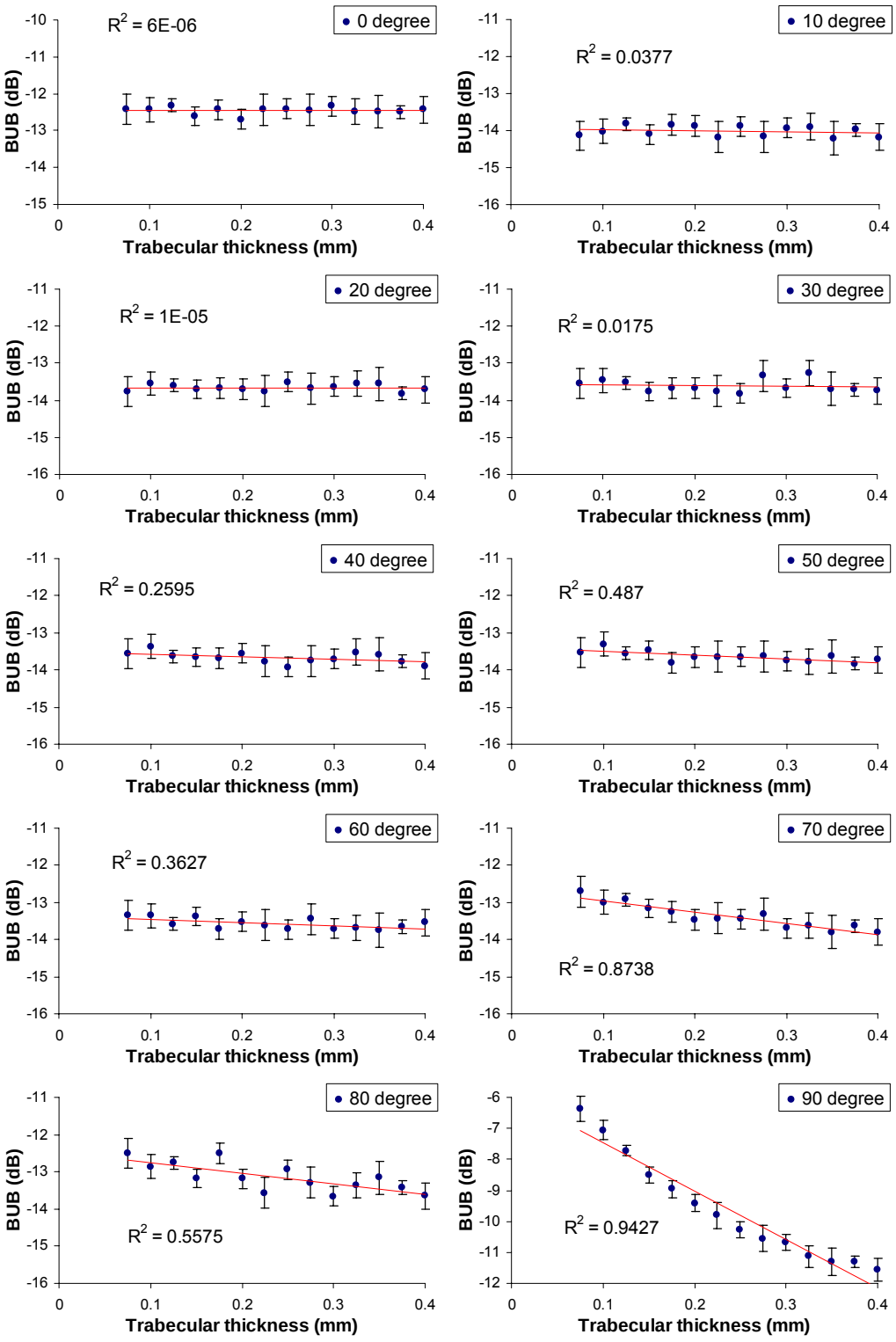

Figure 4-22 BUB vs. different trabecular thickness using 5 MHz ultrasound transducer. Trabecular spacing is constant (s = 0.8). A linear regression is also shown (red line).

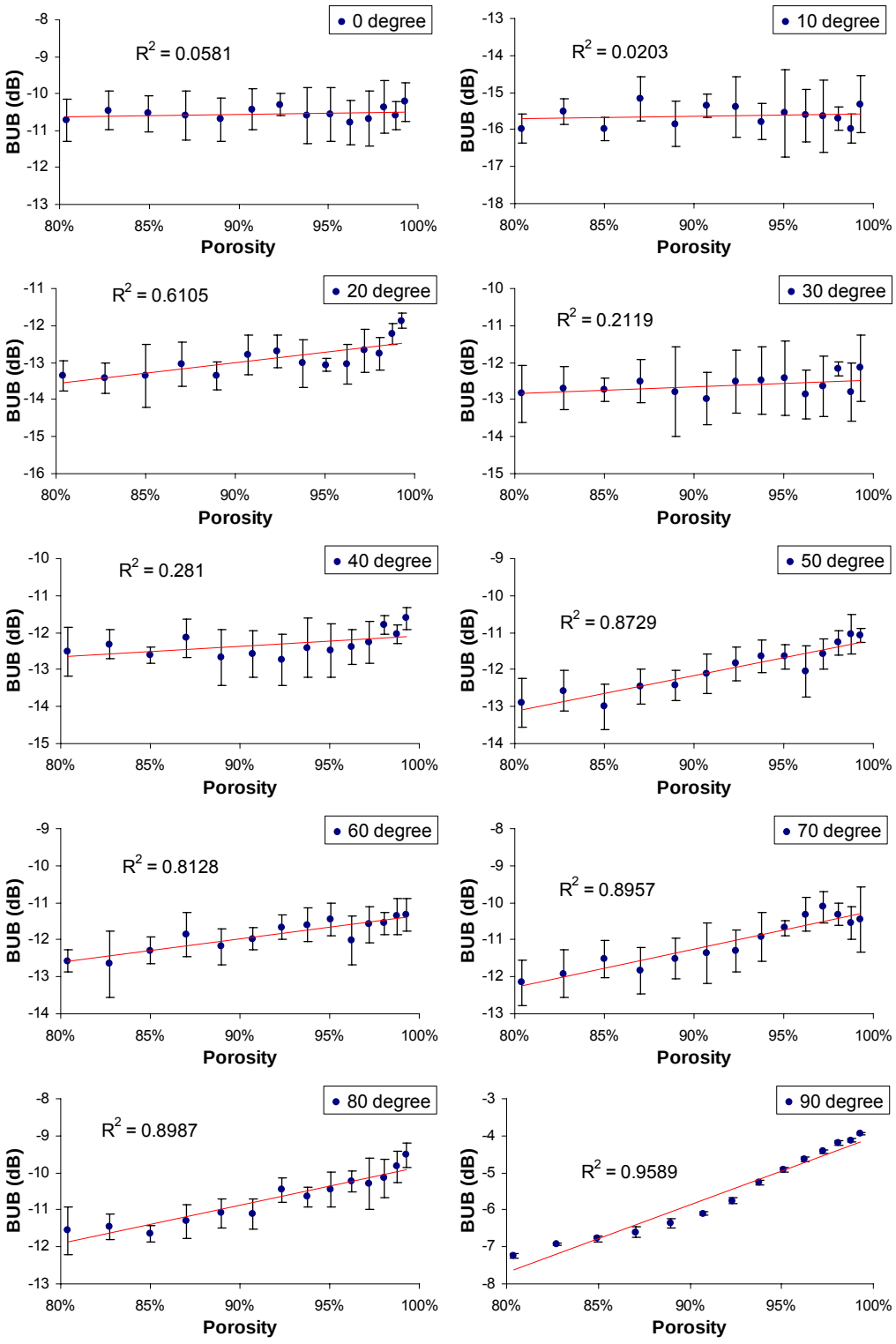

Figure 4-23 BUB vs. porosity controlled by Tb.Th of the wire model for different trabecular orientation using 2.25 MHz ultrasound. s = 0.8. A linear regression is shown (red line).

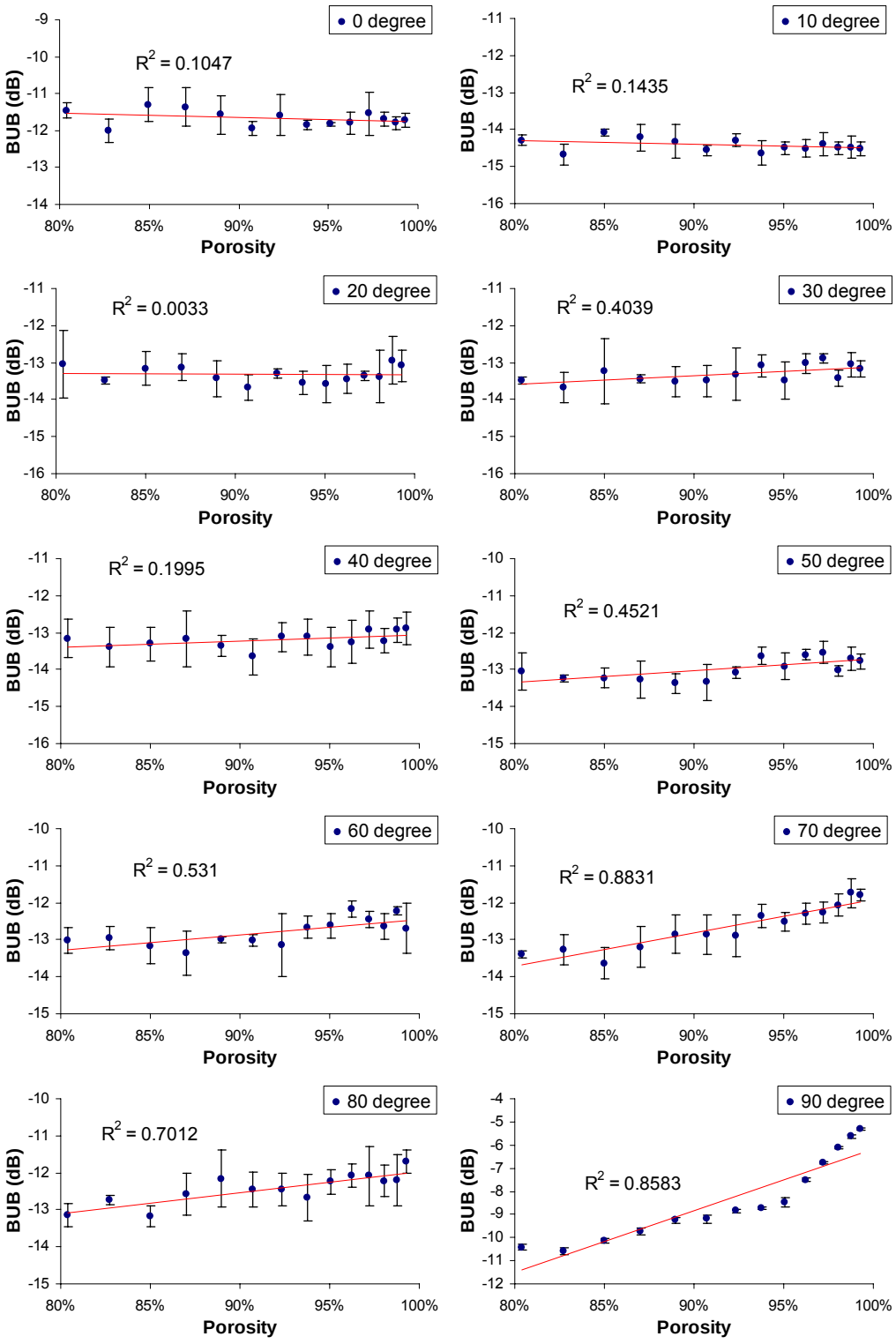

Figure 4-24 BUB vs. porosity controlled by Tb.Th of the wire model for different trabecular orientation using 3.5 MHz ultrasound. $s = 0.8$. A linear regression is shown (red line).

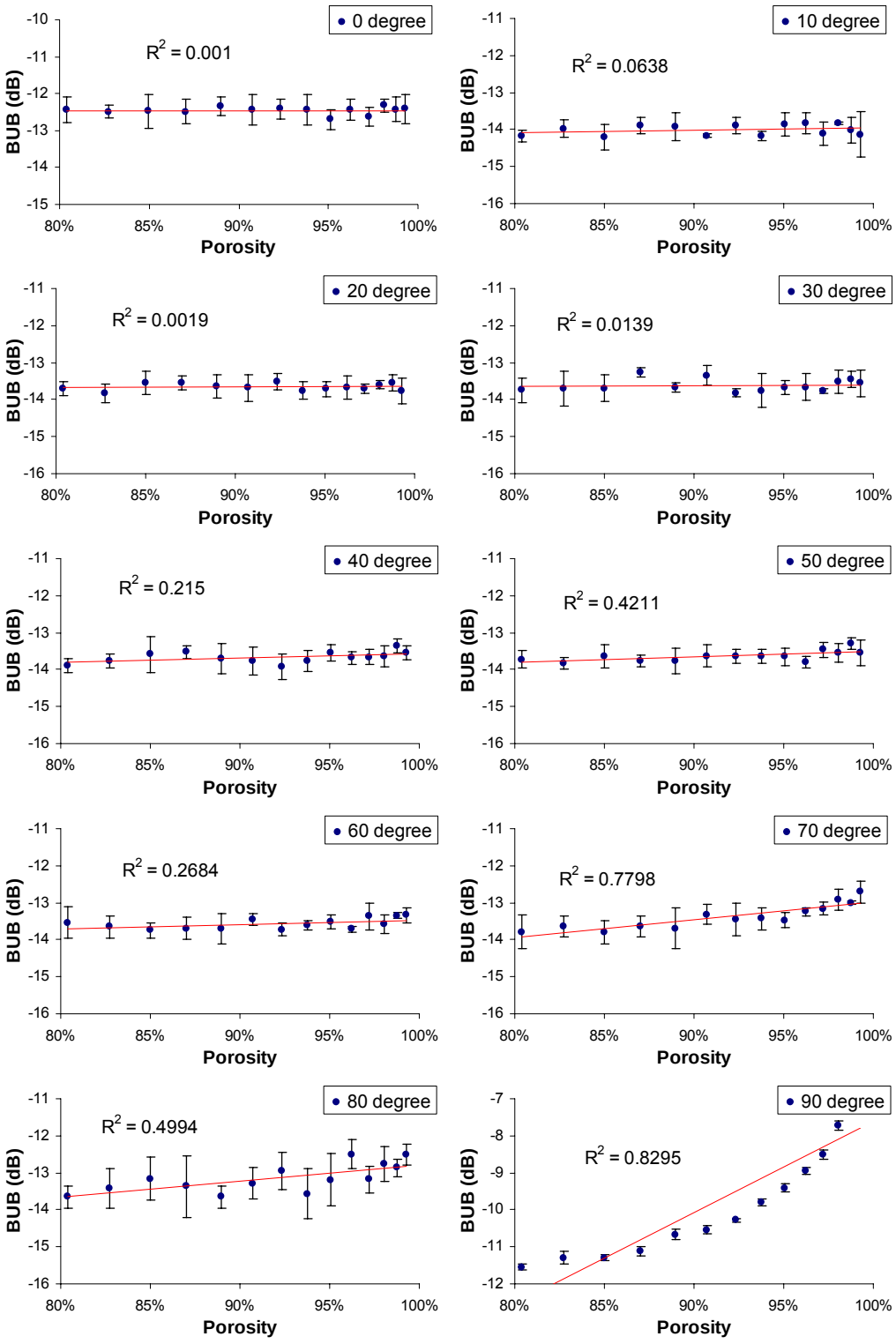

Figure 4-25 BUB vs. porosity controlled by Tb.Th of the wire model for different trabecular orientation using 5 MHz ultrasound. s = 0.8. A linear regression is shown (red line).

This trend of change could be understood as that, for media with low scatterer density such as the wire model, more backscattering processes occurring at the thicker trabeculae/lower porosity cases, weaken the energy of the received signal. In addition, when the angle between trabecular orientation and the wave propagating direction is getting large, the wire model becomes similar to a stratified model (layered model) as shown in figure 4-26; the smaller the trabecular thickness, i.e., bigger porosity, the more it is layered, and the stronger the backscattered signal is.

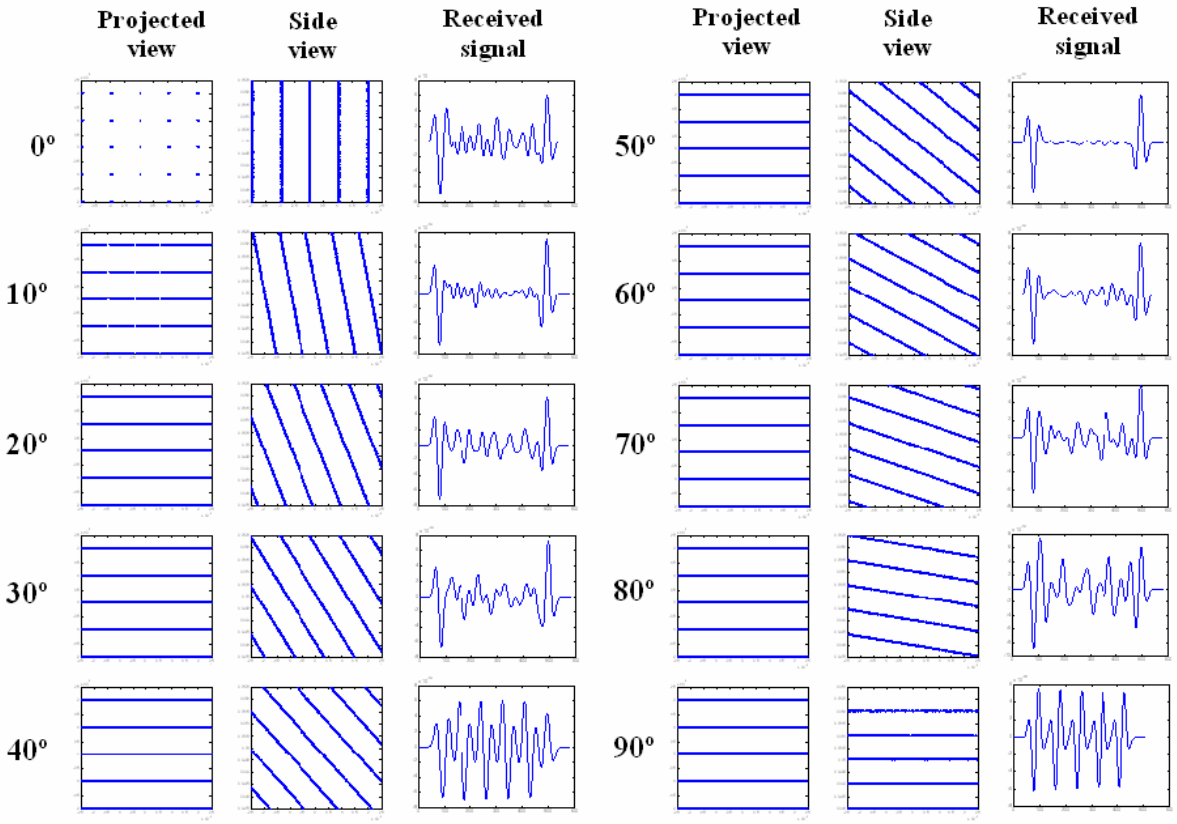

Figure 4-26 Rotation of the trabecular affects the received ultrasound backscatter signal.

C. Discussion

It is the first computer simulation of the wired model, and also the first time that both the cellular model and wire model are simulated under the same circumstances for comparison purpose: same ultrasound transducers, same ultrasonic field being generated, and same scatterer unit.

In this study, both the cellular model and the wire model proved their usefulness in evaluating the porosity and structural parameters of the porous material such as cancellous bone by ultrasound backscattering.

The cellular model can simulate a wide spectrum of porosity by control the pore size of the model. It showed that when the trabecular orientation vector has a component along the wave propagating direction (i.e., less than 90º), the change of pore size could explain more than 70% of the variance of the ultrasound backscattering coefficient, and the change of corresponding porosity could explain over 80% of the variance of BUB.

The porosity of the wire model is controlled by two parameters, the trabecular spacing and trabecular thickness. The effect of these two parameters can be assessed independently by fixing one and changing the other. It has been clearly shown that the BUB decreases accordingly to the porosity that is changing by trabecular spacing, when the trabecular orientation is not perpendicular to the wave propagating direction. If the incident wave is normal to the trabecular, the BUB is mainly affected by the trabecular thickness. In another word, for the wire model, it has been revealed that trabecular spacing is responsible for the change of ultrasound backscattering when the trabecular orientation vector has a component in the incidence direction, while the trabecular thickness is the one that is responsible for the

change of ultrasound backscattering when the trabecular lies perpendicular to the wave direction. The disadvantage of the wire model is that, it can only simulate high porosity range of over 80%, if fit in the structural parameters according to the reported value of human cancellous bone.

Generally speaking, for the simulation of cancellous bone as a porous material composed of pores and trabecular network, the cellular model simulates the pores while the wire model simulates the trabeculae. They predict the backscattering change from two different points of views, but reach the same conclusion. This showed that the reflection ultrasound method is not sensitive to the shape of a scatterer of wavelength size but to the spacing between the scatterers. The two models should be chosen based on the purpose of the study.

Chapter 5 Evaluation of Cancellous Bone Porosity

Cancellous bone is a two phase material. It is built by the pore walls which are made of the calcified materials of trabeculae and plates, and the fatty marrow within the pores. The porosity of cancellous bone changes rapidly with metabolic and disease status. Previous research (Parfitt 1987) indicated that in osteoporosis, plates and trabeculae become thinner and gradually disappear; as a result, the porosity increases and bone material properties change. Bones with osteoporosis become fragile and more likely to break. But if diagnosed sufficiently early, patients with osteoporosis may be treated effectively to reduce the risk of fracture (Schlienger and Meier 2003; Bouxsein, Kaufman et al. 2004). Quantitatively monitoring bone porosity would be a great advantage in detecting osteoporosis and assessing treatment.

5.1 Computer simulation study

To study the relationship between cancellous bone porosity and ultrasound backscattering, a computer simulation was firstly performed to obtain a theoretical prediction.

Fig 6-1 shows the cross-sectional view (normal to the wave propagation direction) of the models. Here the pores were represented by spherical cavities buried inside the medium, which had the diameters of 0 mm, 0.6 mm, 0.8 mm, and 1mm, respectively. This design was

homogeneous in every direction, so that the effect of trabecular orientation factor was removed. Therefore although this model is unrealistic to be built in practical, it provided a better over all guidance than the cellular model being used in many real experiments which is described in previous chapter

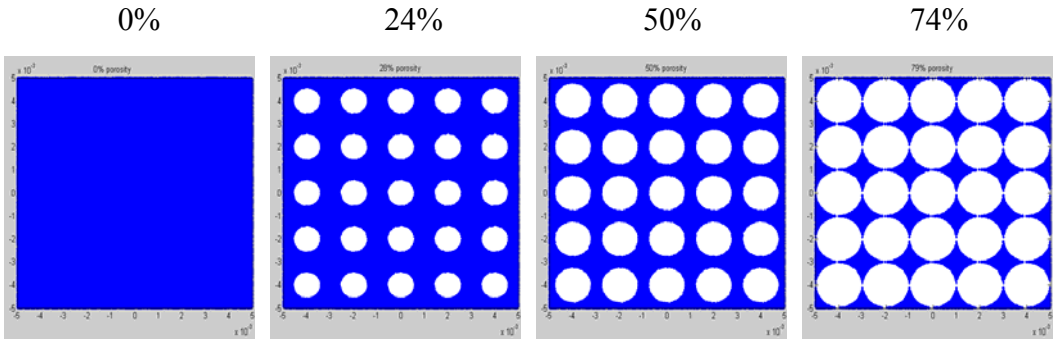

Figure 5-1 Cross-sectional view of simulated porous bones with different porosity (noted above). The white circles represent the spherical cavities inside the phantoms.

The transducers were generated as both piston (planar, unfocusing) transducer and convex (focusing) transducer (Figure 5-2). The piston transducer had a center frequency of 5 MHz, and radius of 3 mm. The convex transducer had 16 elements, with each element 5 mm × 1mm in size and ¼ mm apart. The radius of the convex was 2 cm, and the center frequency of the transducer was also 5 MHz.

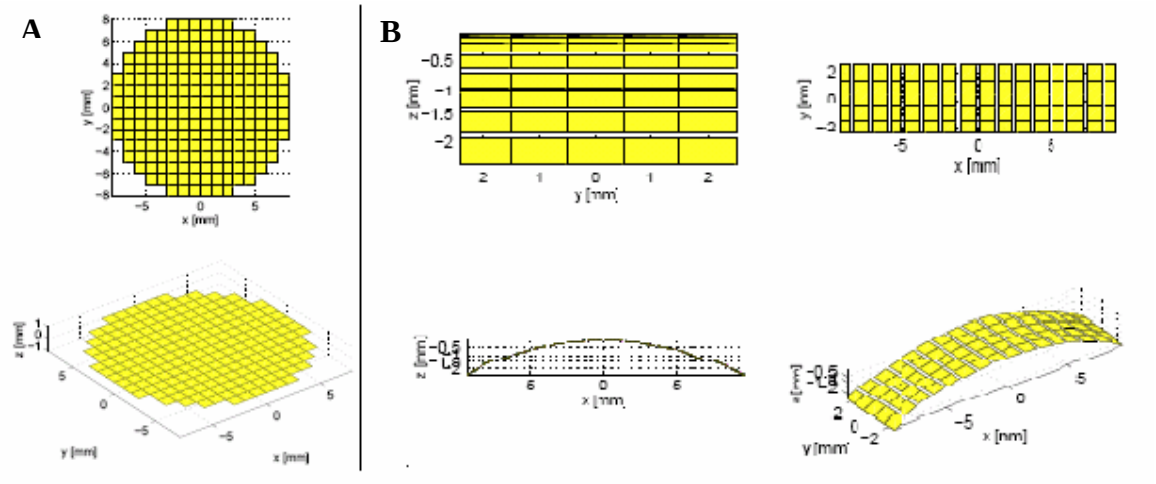

Figure 5-2 A) Piston transducer (r = 3 mm) and B) convex transducer (16 element, convex radius=2 cm) generated by Field II ultrasound simulator. [Adapted from Field II user's guide]

The computer simulation shows that for the ideal case there is a linear relationship between a material's porosity and the peak amplitude of the reflected signal, as shown in figure 5-3.

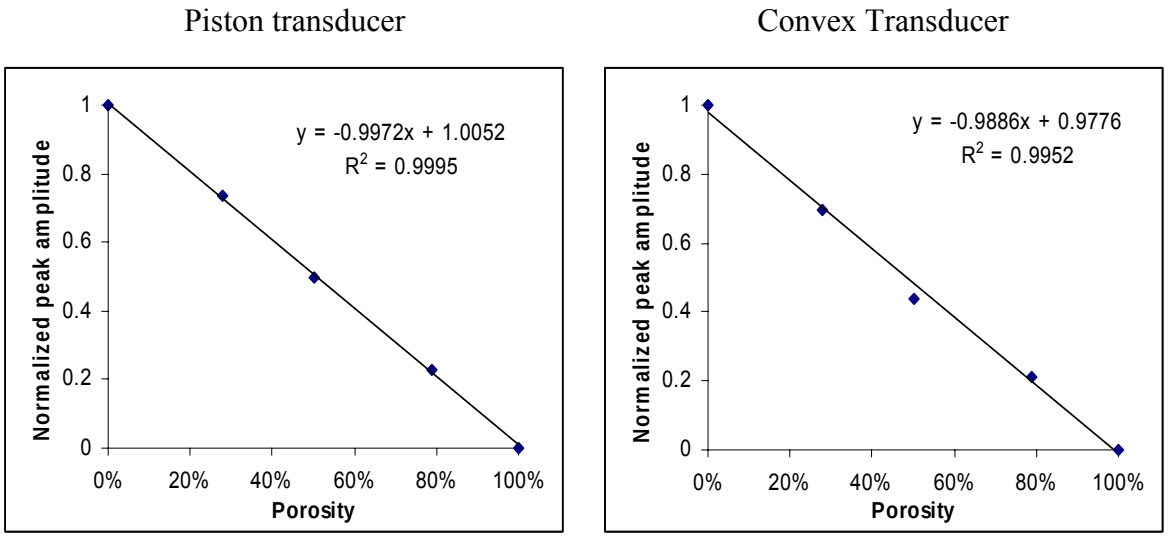

Figure 5-3 Computer simulation results. The normalized peak amplitude of the reflected signal changes with material porosity.

5.2 Bone-mimicking phantom Study

In the phantom study, I used the acrylic plastic phantoms with cylindrical capillary pores running normal to the surface to mimic the cancellous bone. The parameters of ultrasonic waves reflected from the phantoms with porosities from 0% to 49% were measured using a planar transducer with a center frequency of 5 MHz.

5.2.1 Bone-mimicking phantoms

First, the simple acrylic plastic phantoms with a square cross section of 20 × 20 mm^2 and a thickness of 6 mm were made and fabricated with cylindrical capillary pores normal to the square cross section, as the cellular model of cancellous bone as described in previous chapter. One phantom consisted of pure acrylic plastics without pores, and three phantoms had cylindrical capillary pores with different diameters and distributions to control the porosity of each phantom (Figure 5-4 and Table 5-1).

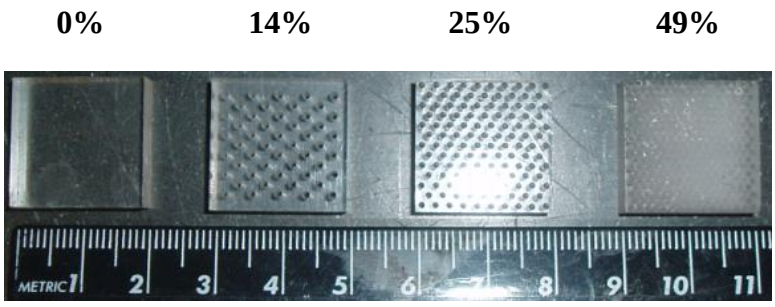

Figure 5-4 Acrylic plastic phantoms with paralleled cylindrical capillary pores.

Table 5-1 Properties of four phantoms

Phantom	Pore diameter	Pore number	Porosity
1	0.0 mm	0	0.0%
2	1.2 mm	50	14.1%
3	1.0 mm	124	24.3%
4	1.0 mm	295	57.9%

As shown in Table 5-1, the porosities of the four phantoms were 0.0%, 14.1%, 24.3%, and 57.9%, respectively. Although these porosities were relatively lower than the reported porosity range of dense cancellous bone of human which is 30% – 70% (Lee and Choi 2007) and my experimentally obtained range of bovine cancellous bone which is 10% – 80%, they still covered the whole range of cortical bone (0% – 30%) and partial range of the dense cancellous bone.

The phantoms largely simplify the complex structure of cancellous bone, using the porous acrylic structure to mimic the trabecular network. The fatty marrow which fills the pores of cancellous bone *in vivo* can also be simplified to water. Table 5-2 compares the acoustic properties of phantom materials (acrylic plastics and water) measured in experiment and human cancellous bone materials (trabeculae and fatty marrow) in the literature (http://www.bamr.co.za/velocity20of%20materials.shtml).

Table 5-2 Comparison of the acoustic properties of phantom materials measured in experiment and human cancellous bone material in literature.

Material	Density	Speed of Sound
Acrylic plastics	1.2 g/cm^3	2750 m/s
Cancellous bone	1.3 g/cm^3	2300 m/s
Fat	0.9 g/cm^3	1459 m/s
Water	1.0 g/cm^3	1480 m/s

As shown in table 5-2, the density and sound velocity of the acrylic plastics are about 1.2 g/m^3 and 2750 m/s, respectively, which are comparable to those of the human cancellous bone, indicating the use of acrylic plastics here was proper to mimic the trabecular material. The acoustic properties of water are also similar to those of fat. In addition, previous study revealed that the results of *in vitro* measurements substituting fatty marrow with water are consistent with *in vivo* measurements (Wear 2005). Therefore, the designed phantoms immersed in water should be appropriate in mimicking cancellous bones filled with fatty marrow as *in vivo*.

5.2.2 Ultrasound measurements

The ultrasound measurements were performed using pulse-echo method in a water bath which was filled with distilled water at room temperature around 18 °C. The scheme of using

the pulse-echo (reflected) ultrasound method to detect the porosity was that, giving a porous material, first the ultrasound signal was generated and transmitted out by a planar ultrasound transmitter. The ultrasound signal was then partly reflected back from the porous material. The reflected signals were received by the ultrasound receiver and recorded for further analysis.

The experiment was setup as show in figure 5-5.

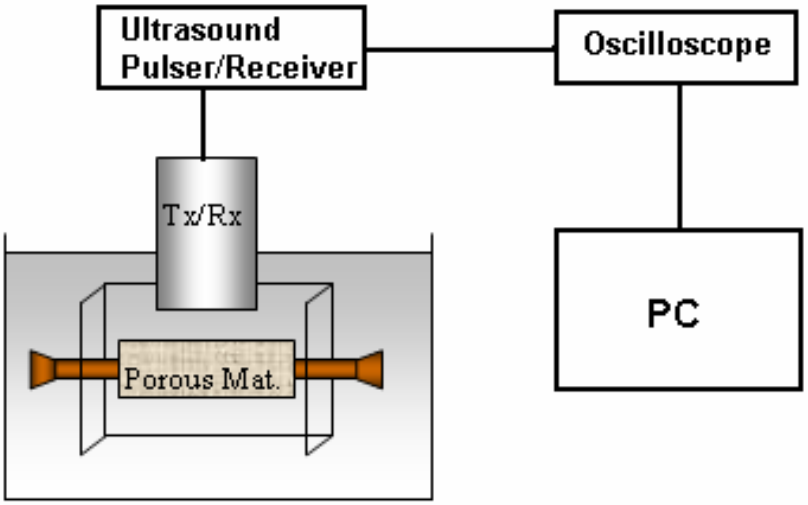

Figure 5-5 Experiment Setup.

The phantoms were immersed in water to simulate the soft tissues in which the cancellous bone is embedded *in vivo*. A planar PCT transducer (Panametrics V326, Panametrics Inc., Waltham, MA, USA) with the central frequency of 5 MHz and diameter of 0.375 inch was used. The ultrasound signals were generated by an ultrasound pulser/receiver (Panametrics

5052PR, Panametrics Inc., Waltham, MA, USA) operating at the pulse-echo mode. No attenuation and damping were applied to the generated signal, and no high-pass filter to the received signal. But there was a 40 dB gain applied to the received signal. The output of pulser/receiver was connected to digital oscilloscope (Tektronix 2540, Tektronix Inc., Beaverton, OR, USA), where the signal was digitized (sampling frequency of 100 MHz) and displayed in real-time. The oscilloscope was then connected to the computer via a PCI-GPIB Card and Cable (National Instruments Inc., Austin, TX), and this allowed the loading of the displayed signal from the oscilloscope to the computer for off-line analysis. The data analysis was done by the customized LabVIEW software (LabVIEW 7.1, National Instruments, Austin, TX, USA). The peak amplitude and the integral of the reflected signals were analyzed.

Previous computer simulation shows that for the ideal case there is a linear relationship between a material's porosity and the reflected signal (Figure 4-4). The results of phantom study confirmed this simulation finding by shown similar linear relationship between the phantom porosity and the parameters of the reflected ultrasound signals (Figure 5-6).

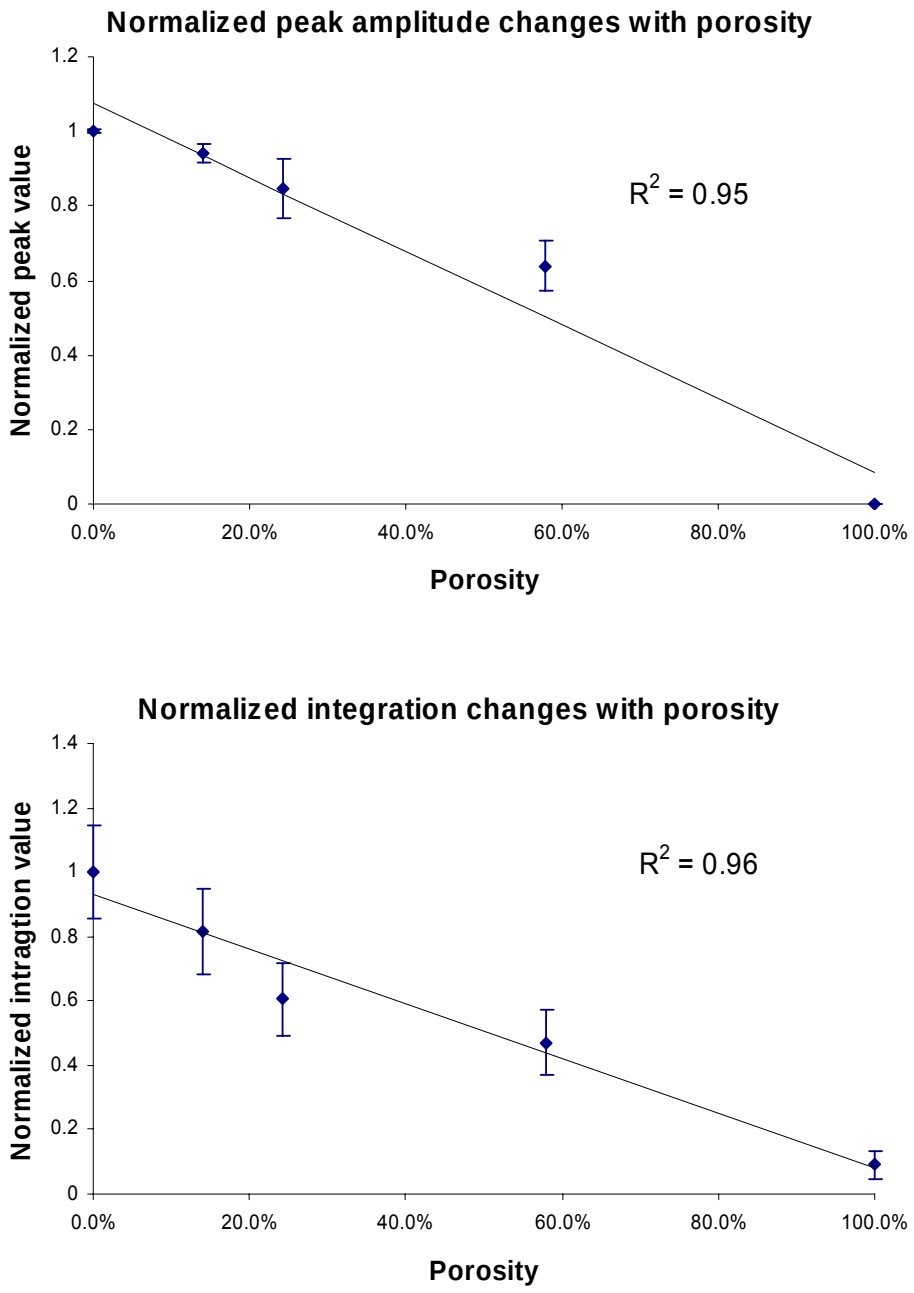

Figure 5-6 The experimental results of phantom study agreed with computer simulation.

5.3 In vitro cancellous bone study

Finally, the *in vitro* bone sample study was performed. Twelve cancellous bone samples were cut from cow femur bones for *in vitro* study (Figure 5-7). These bones were immersed in alcohol for two weeks and defatted.

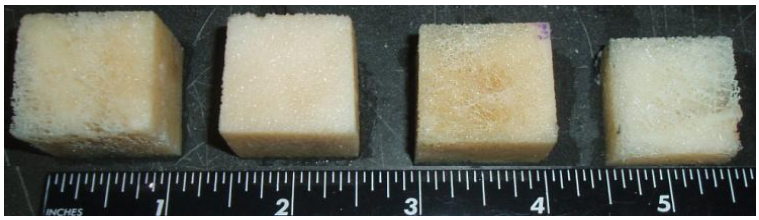

Figure 5-7 Bone samples for experiment

The porosities of these bone samples were estimated by calculating the ratio of the mass in air to the "wetted mass" when the sample was immersed in water and all the air was drained from the pores:

$$porosity = \frac{weight\quad of\quad "wetted\quad mass" - weight\quad of\quad dry\quad mass}{density\quad of\quad water * volume\quad of\quad the\quad sample} * 100\%.$$

The apparent density was defined as the ratio of the weight of dry mass over the total volume:

$$Apparent\quad density = \frac{dry\quad weight}{total\quad Volume}.$$

The plot of the estimated porosity and the apparent density of all the samples showed that the acquired apparent density was linearly and inversely related to the estimated porosity (Figure 5-8). This agreed with previous researches and indicated that our estimated porosity was reasonable and close to the real value.

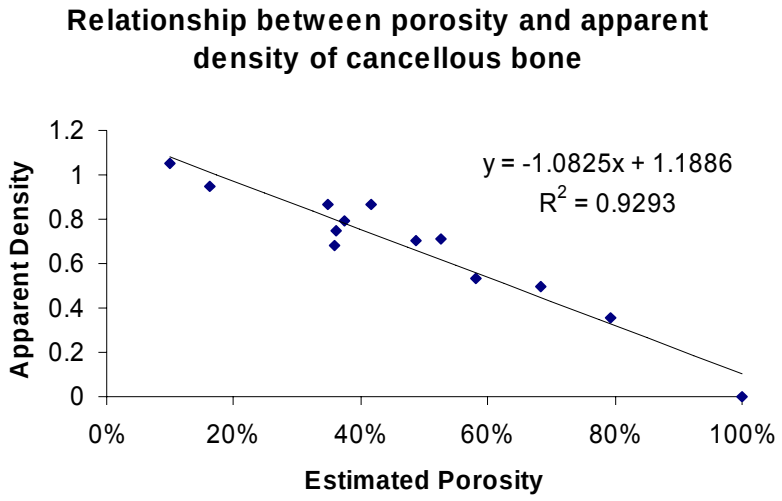

Figure 5-8 Relationship between estimated porosity and measured apparent density of cancellous bone samples.

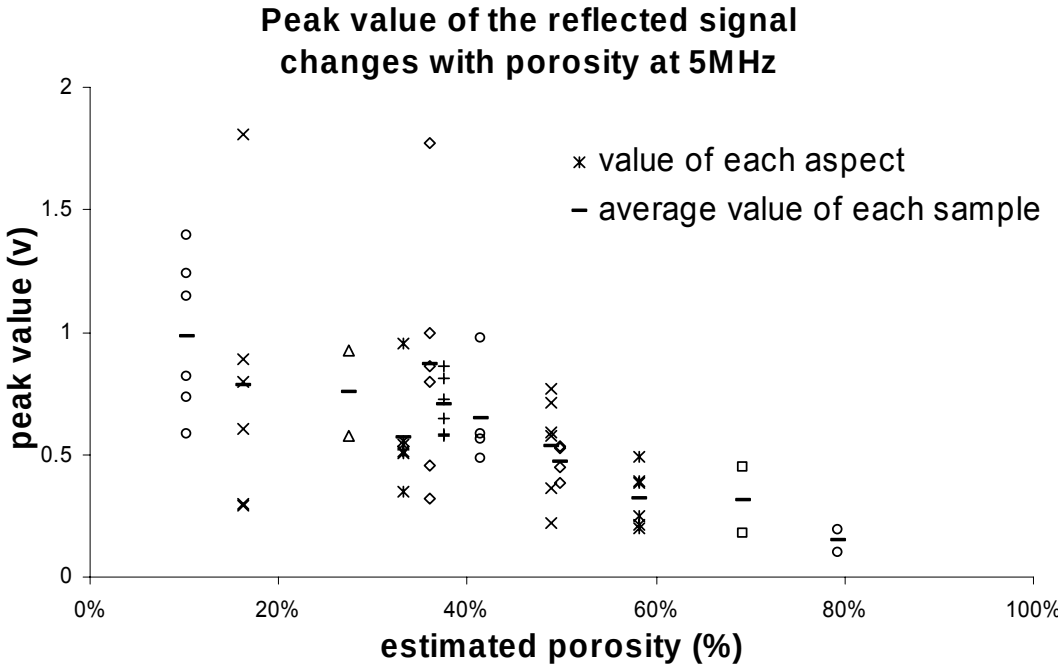

Figure 5-9 Results of the *in vitro* study.

In figure 5-9, the peak amplitudes of the reflected signals from different faces of each sample were plotted. This plot showed that the observed porosity depends upon the face interrogated showing heterogeneity of the porosity. Although the reflected signal from different faces of one single bone sample varied a lot, there was still a good linear relationship between the average porosity and the peak amplitude of the reflected ultrasound signal when the values were averaged for individual sample referring to the over-all porosity (Figure 5-10).

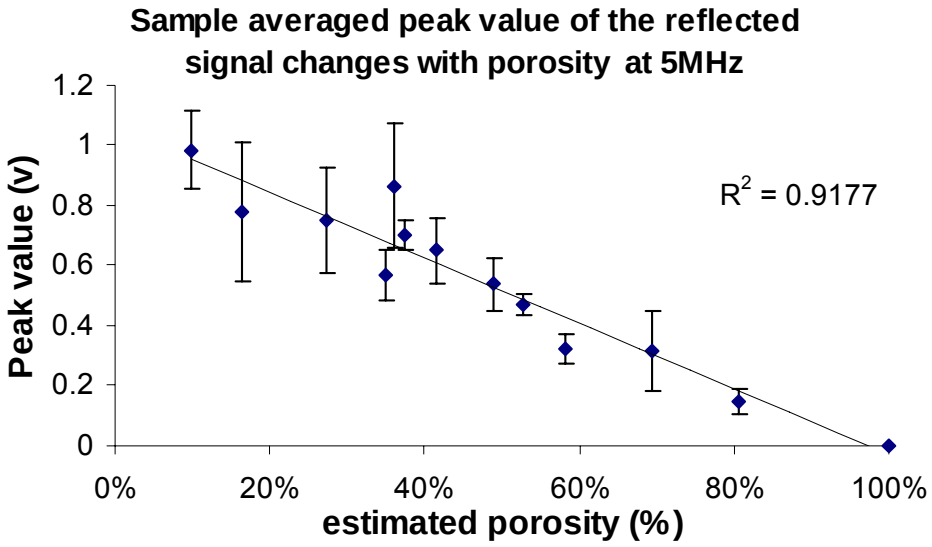

Figure 5-10 Sample averaged peak amplitude of the reflected signal changes with porosity.

The error bars shown in figure 5-10 and 5-11 were the standard error, given by $s/\sqrt{n}$, where s is the sample standard deviation, and n is the sample number. All the statistic analysis was done by Microsoft® Excel 2002 (Microsoft Corporation, Redmond, WA, USA).

The linear relationship shown between the sample averaged peak amplitude and the estimated porosity also applied to the sample averaged integration value and the porosity (Figure 5-11). In case that the peak amplitude is hard to detect, integration of the reflected signal could be a good alternative for porosity detection.

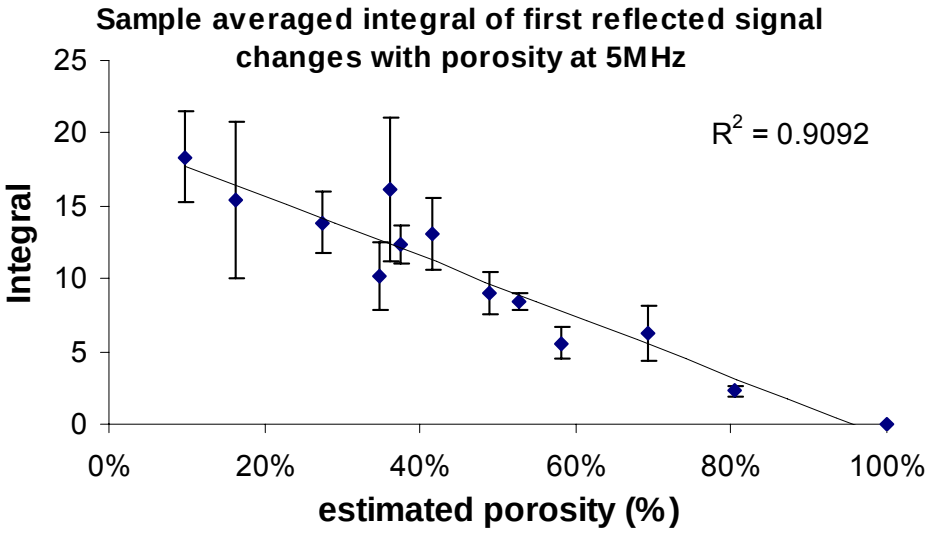

Figure 5-11 Sample averaged peak amplitude of the reflected signal changes with porosity.

In summary, the average porosity is correlated with the density, while the local porosity depends upon the heterogeneity of the cancellous bone. It has been shown in this study that the average porosity of cancellous bone can be directly determined by the parameters of the ultrasound signals reflected from the bone, as there is a linear relationship between them. It has also been shown that the observed porosity depends upon the face interrogated. This orientation dependency may be used to monitor the density of cancellous bone and study the effect of the microarchitecture of cancellous bone.

Chapter 6 Evaluation of Short Bone

Short bone is mainly composed of cancellous bone. Patella is typical short bone. It is also the largest sesamoid bone (defined as a bone embedded within a tendon) in the human body. Patella is important in knee extension as it is attached to the tendon of the quadriceps femoris muscle that controls the straightening of the leg. According to literatures, patella is one of the preferred sites of diagnosing osteoporosis (Heaney, Avioli et al. 1989; Stegman, Heaney et al. 1994; Stegman, Heaney et al. 1995; Stegman, Heaney et al. 1995; Stegman, Davies et al. 1996).

6.1 Evaluation of short bone – mimicking phantoms

Before the *ex vivo* and *in vivo* experiments with patella, a short bone mimicking phantom study was performed to test the experiment design and predict the results.

6.1.1 Phantom preparation

In the phantom study, nine acrylic plastic cubes fabricated with different porosities were used to simulate the patella bone (Figure 6-1). The validation of using acrylic plastics phantoms immersed in water to mimic bone samples has been demonstrated in the previous chapter.

Here each cuboid acrylic plastic phantom was 2 cm × 2 cm × 2 cm in size. One of the phantoms was composed by pure acrylic plastics, referring to the 0% porosity. The other

eight phantoms contained two paralleled layers of intact plastics, called the compact faces, which mimic the cortical layer of short bones. The compact faces had different thickness, called edge thickness in table 6-1. In between the compact faces, the central part of the phantom contained orthogonally interleaved cylindrical capillary holes which are normal to the orthogonal surfaces in order to simulate the trabecular network. There were five distribution patterns of the capillary holes with the diameters ranging from 1.0 mm to 1.6 mm, respectively. The detailed parameters of the phantoms are summarized in table 6-1.

Figure 6-1 Examples of the acrylic short bone phantoms.

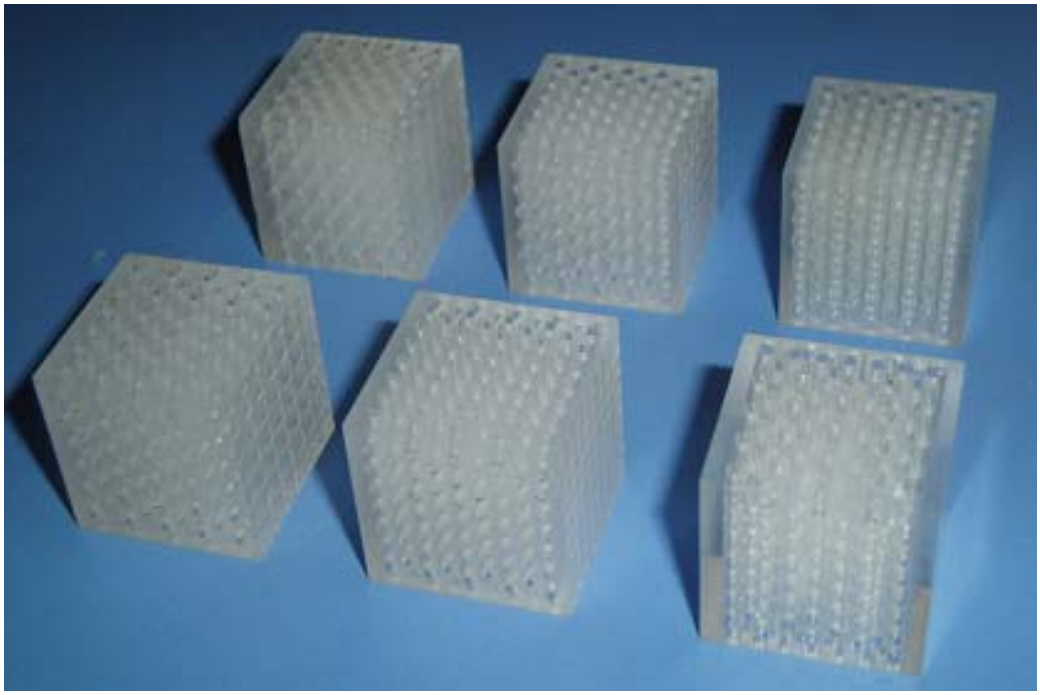

Table 6-1 Properties of nine cuboid short bone phantoms.

Phantom	Pore distribution	Edge (mm)	Pore spacing 1 (mm)	Pore spacing 2 (mm)	Pore diameter (mm)	Apparent Density	Porosity
1	Solid	1.5	0	0	0.0	100.00%	0%
2	Type A	1.3	2	1.5	1.0	74.69%	20.4%
3	Type A	1.2	2	1.5	1.4	68.23%	36.9%
4	Type A	1.5	2	1.5	1.6	56.83%	46.3%
5	Type B	1.4	2	1.25	1.0	79.99%	23.4%
6	Type B	1.4	2	1.25	1.2	82.35%	32.3%
7	Type C	1.6	~1.7	~1.7	1.4	72.66%	42.0%
8	Type D	1.9	1.5	2	1.2	61.11%	30.8%
9	Type E	0.5	1.5	1	1.0	56.64%	44.1%

* Pore spacing indicates the distance between the centers of two pores.
Pore spacing 1: spacing from porous face
Pore spacing 2: spacing from intact face

Among these parameters, pore spacing and pore diameter are the two that characterize the structural property of the phantoms, and together they define the porosity and affect the apparent density. As shown in figure 6-2, the apparent density was theoretically in agreement with the porosity; the variation shown in the figure should be mainly due to the fabricating errors and approximation in the calculation. It is said so because the phantoms falling in the two similar patterns (group 1: #3, #7 and #8; group 2: #2, #5 and #6) were not related in structure, as they had different pore distribution style (Table 6-1).

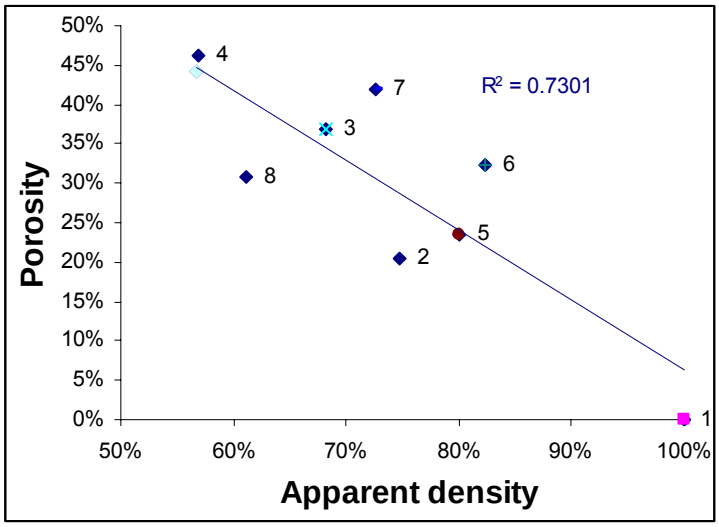

Figure 6-2 Porosity vs. apparent density for the nine short bone mimicking phantoms.

6.1.2 QUS measurement

After immersed in water overnight so that all the pores were saturated by water, the samples were acoustically tested using a QUS system. The system consisted of an ultrasound pulser-receiver, a pair of ultrasound transducers, a digital oscilloscope and a water tank. The paired transducers (Panametrics V326, Panametrics Inc., Waltham, MA, USA) were unfocusing transducers with a center frequency of 5 MHz, and diameter of 0.375 inch. The ultrasound signals were generated by the ultrasound pulsar/receiver (Panametrics 5054A, Panametrics Inc., Waltham, MA, USA) operating at the transmission mode. No attenuation and damping were applied to the generated signal, and no high-pass filter to the received signal. There was a 40 dB gain applied to the received signal. The output of pulser/receiver was connected to the digital oscilloscope (Tektronix 2540, Tektronix Inc., Beaverton, OR, USA), where the

signal was digitized (sampling frequency of 100 MHz) and displayed in real-time. The oscilloscope was then connected to the computer via a PCI-GPIB Card and Cable from National Instruments Inc. (Austin, TX, USA), -which allowed the loading of the displayed signal from the oscilloscope to the computer for off-line analysis. The data analysis was done by the customized LabVIEW software (LabVIEW 7.1, National Instruments, Austin, TX, USA).

The samples were placed between the two transducers by a sample holder. The distance between the transducers was fixed at 5 cm during the measurements. Measurements of the samples were conducted in the water bath maintained in the room temperature that varies between 19.0 °C and 19.7°C.

Ultrasound velocity was determined by the time of flight (TOF) method. Thickness of the specimen along the wave propagating pathway could be determined by subtracting the distances from each transducer to the closer side of the sample from the total distance between the two transducers. The distance between each transducer and the sample was obtained by reflection ultrasound method with each transducer performed as transmitter/receiver probe and the PANAMETRICS pulser/receiver operating at its pulse-echo mode. Transmitted ultrasound signals were recorded in the presence and absence of the phantoms, respectively. Then the speed of sound and BUA was calculated using the equations given in chapter 2.

The TOF was determined accurately by locating the peak amplitude of the envelope of the received waveforms. The envelope detection has been proved to be effective in eliminating phase effect (Wear 2007). The envelope was detected by creating the analytic signal of the

received signal using a Hilbert transformation. The analytic signal is a complex signal, of which the real part is the original signal and the imaginary part is the Hilbert transform of the original signal; the envelope was then calculated by taking the absolute value of the analytic signal. Although not used here, a low-pass filter could be applied to the resulted envelop in order to eliminate ringing and smooth it. Peak value and/or peak-to-peak value of the envelope was then easily detected by the LABVIEW data analysis program (Figure 6-3(B)). Furthermore, if the peak value of the envelope is the only interest, this method can be even simplified by peak holding, as shown in figure 6-3(A).

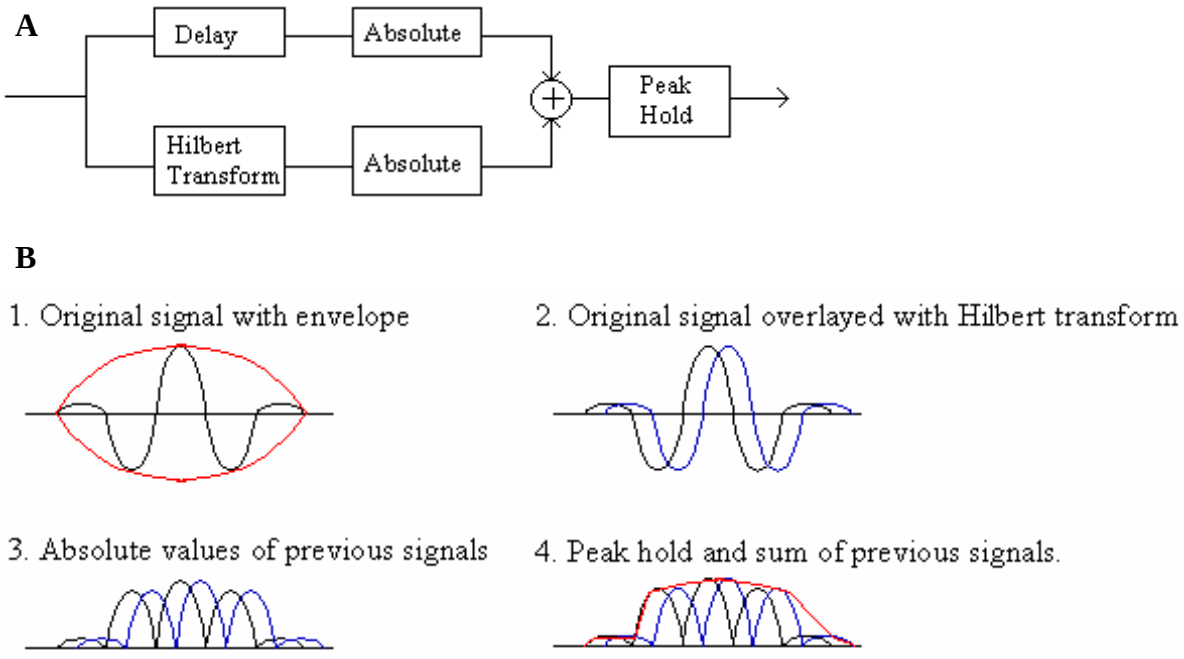

Figure 6-3 Block diagram of the envelope peak detector (A) and illustration (B). [Adapted from http://www.numerix-dsp.com/envelope.html]

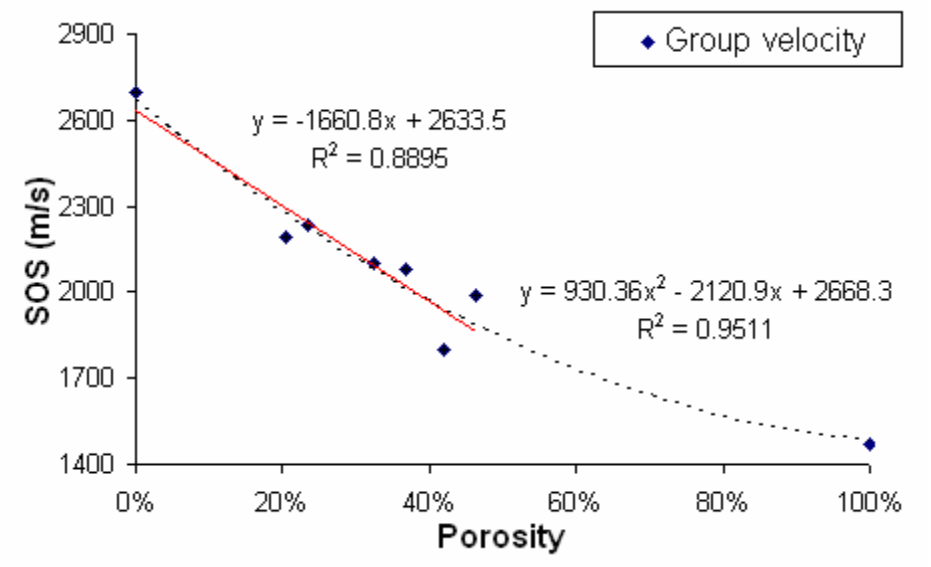

Figure 6-4 SOS measured by QUS method at 5 MHz vs. porosity for seven phantoms.

Figure 6-4 shows the result of the ultrasound group velocity measurement using QUS method. The speed of sound (SOS) decreased as the porosity increased, following a polynomial trend curve (R^2 = 0.95). But since the curvature of the trending curve is considerable small, a linear fit was in good agreement with the local data, i.e., at the lower porosity range (0 % to 50 %, R^2 = 0.89). This result agreed with previous studies by different groups (Lee, Roh et al. 2003; Wear 2005).

Figure 6-5 shows that the peak amplitude of the transmitted signal through the phantoms varied with porosity. This relationship appeared to be linear (R^2 = 0.99) at the porosity range of 20 % to 50 %.

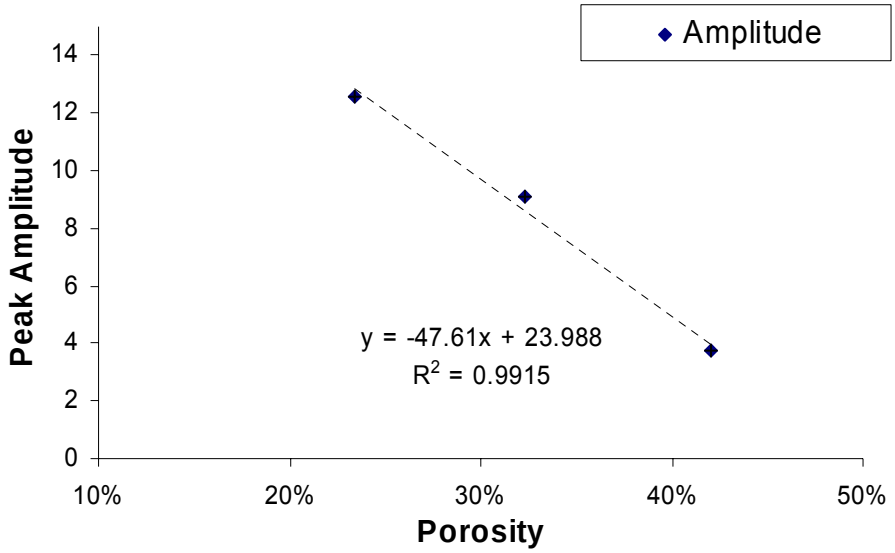

Figure 6-5 Peak amplitude measured by QUS at 5 MHz vs. porosity for three phantoms.

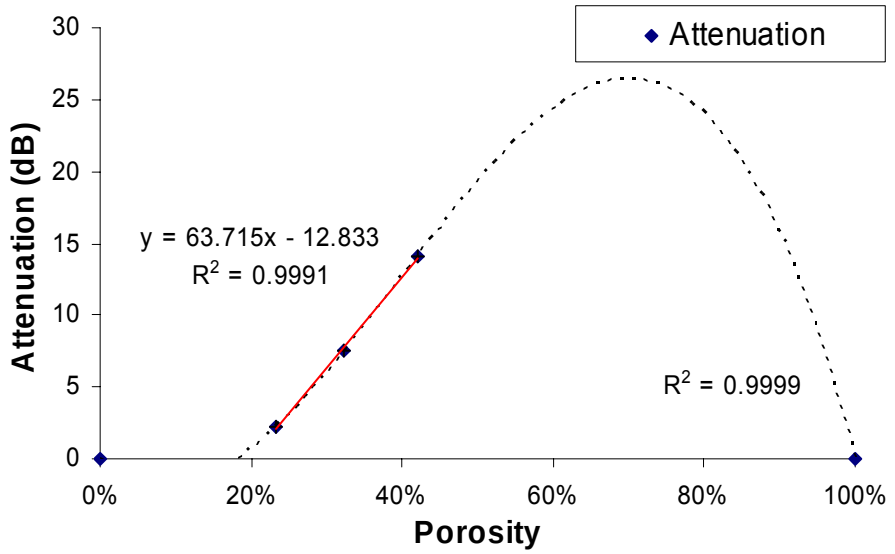

Figure 6-6 Calculated attenuation coefficient at 5 MHz vs. porosity for three phantoms.

The attenuation coefficient of the same three phantoms shown in figure 6-4 was calculated as a logarithm difference between the amplitude of the received signals in the presence and absence of the phantom on the ultrasound wave propagation route (Figure 6-6). Besides the linear fit at the lower frequency range, an estimated polynomial curve ($R^2 \approx 1$) was also shown in the figure. The fitting curve was in good agreement with the predicted changing curve by Nicholson et al (Nicholson, Strelitzki et al. 2000). This fitting curve had two phases, the ascending phase and the descending phase. In the ascending phase, the attenuation increased until the porosity was about 70%. This is because the increase of porosity is often accompanied by the increase of interfaces, which causes the scattering and therefore increases attenuation. For the descending phase with porosity over 70%, the pore size or trabecular spacing became to play the major role. As more sound waves went through the pores unattenuated, attenuation coefficient decreased.

6.1.3 Reflection ultrasound measurement

The ultrasound backscattering from the porous phantoms were assessed via the reflection ultrasound measurement, and characterized by scattering parameters, i.e., Integrated Reflection Coefficient (IRC) and Apparent Integrated Backscatter (AIB).

For the reflection ultrasound measurement, an unfocusing PCT transducers with the central frequency of 2.25 MHz (Panametrics V306, Panametrics Inc., Waltham, MA, USA, with the diameter of 0.5") was used. The ultrasound signals were generated by an ultrasound pulser/receiver (Panametrics 5052PR, Panametrics Inc., Waltham, MA, USA) operating at the pulse-echo mode. No attenuation and damping were applied to the generated signal, and

no high-pass filter to the received signal. But there was a 40 dB gain applied to the received signal. The output of pulser/receiver was connected to a digital oscilloscope (Tektronix 2540, Tektronix Inc., Beaverton, OR, USA), where the signal was digitized (sampling frequency of 100 MHz) and displayed in real-time. The oscilloscope was then connected to the computer via a PCI-GPIB Card and Cable (National Instruments Inc., Austin, TX), which allowed the recording of the displayed signal from the oscilloscope to the computer for off-line data analysis. The AIB and IRC were then calculated by the customized LabVIEW software (LabVIEW 7.1, National Instruments, Austin, TX, USA).

The phantoms were immersed in water holding by a sample holder. The sample holder was controlled with a customized LabVIEW software to choose the ROIs in the phantoms. Measurements of the samples were conducted in the water bath maintained at the room temperature.

The algorithms for the calculation of the AIB and IRC were described previously in chapter 2. Firstly an IRC region was defined by thresholding. Then the lateral averaged apparent backscattering power spectrum was obtained by taking Fourier transform of the gated signal. The frequency-dependent backscatter and reflection coefficient was computed by the log-spectral subtraction of the reference spectrum from the acquired data spectrum. With this subtraction, the effect of the measuring instrumentation on the detected parameters could be eliminated. Then the frequency-averaged backscatter and reflection coefficient was obtained by integrating the frequency-dependent backscatter and reflection coefficient in the frequency bandwidth of the transducer (Wear and Garra 1998; Chaffai, Peyrin et al. 1999; Chaffai, Peyrin et al. 2002; Hakulinen, Day et al. 2005; Hoffmeister, Jones et al. 2006). The

AIB and IRC were different in choosing of the windowed/gated data from the reflected signal. The IRC characterizes the signals reflected from the surface part of the material, while the AIB is related to properties of a region inside the porous material.

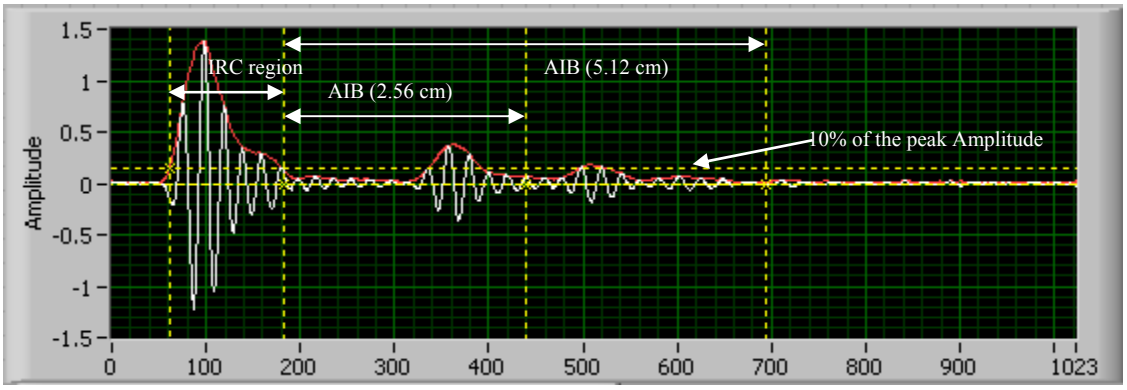

Figure 6-7 Received backscattering signal and the definition of IRC and AIB.

In figure 6-7, the received reflected signal from phantom #8 is shown as an example. The IRC region was defined by thresholding at 10% of the peak amplitude of the signal envelope. A gated region of 256 and 512 samples were isolated from the received signal, corresponding to 2.56 μs and 5.12 μs time duration at the sampling frequency of 100 MHz, and about 2.6 mm and 5.1 mm in depth inside the phantom, respectively. The reference signal was acquired by measuring the reflected RF signal from a 0.6 mm thick steel plate. Then the frequency-averaged backscatter and reflection coefficient was obtained by integration of the frequency-dependent backscatter and reflection coefficient in the frequency bandwidth of the transducer. As shown in figure 4-4, the frequency bandwidth of the 2.25 MHz ultrasound

transducer is from 0.78 to 3.91 MHz. The obtained IRC and BUB were averaged over eight to nine ROIs for each phantom to increase the precision.

The relationship between ultrasound backscattering parameters and the porosity of the phantoms were being studied.

For **porous face measurement**, which means the incident wave was normal to one of the porous sides and parallel to the two compact faces of each phantom, the results are shown in figure 6-8. A good linear relationship between the backscattering coefficients, i.e., IRC and AIB, and the porosity of the phantom was observed. Both the IRC and AIB deceased linearly as the porosity of the phantom increased.

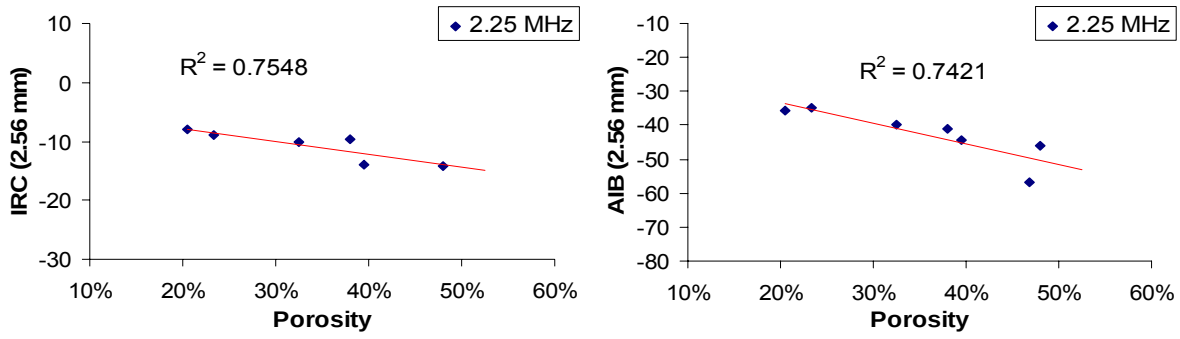

Figure 6-8 IRC and AIB for the porous face measurement.

For **intact face measurement**, which means the incident wave was normal to one of the two compact faces of each phantom, the results are shown in figure 6-9 and 6-10.

The IRC, which characterizes the signal from the surface region of the phantom, remained constant for all phantoms of difference porosity or different compact face thickness.

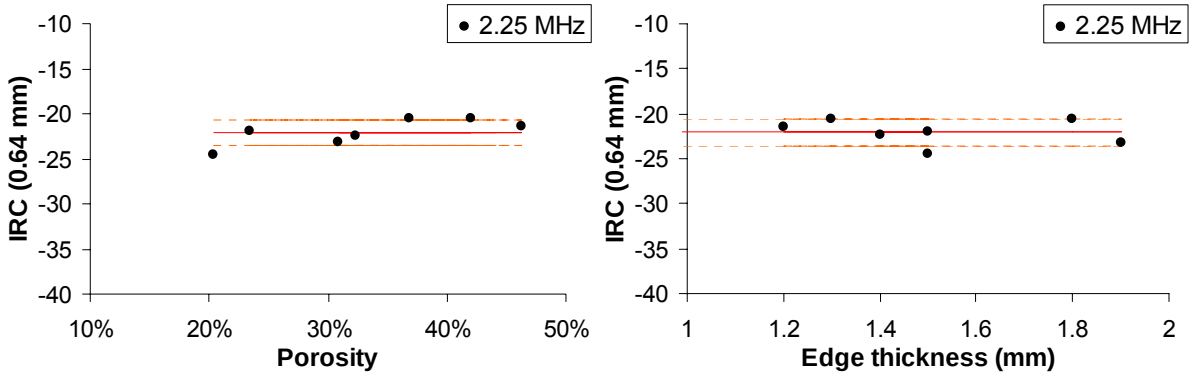

Figure 6-9 IRC for the compact face measurement. Solid red line is the mean value, and dash red lines indicate the standard deviation.

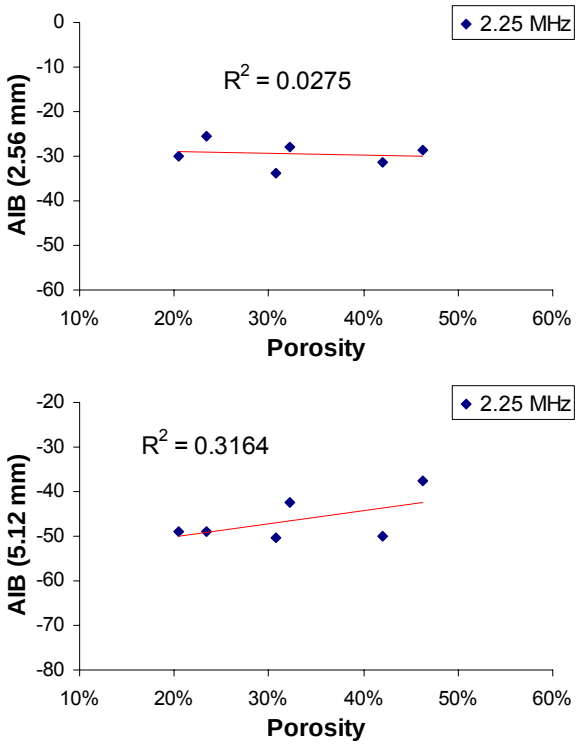

Figure 6-10 AIB for the compact face measurement.

As shown in figure 6-10, there's no apparent trend of change of the backscatter coefficient as the porosity increases. This could be due to: 1) the low intensity of the interior signals, 2) signal overlap from different layers, 3) attenuation effect, and 4) error or bias in porosity estimation.

Figure 6-11 shows that, for 2.25 MHz transducer, the backscatter coefficient dropped linearly as the thickness of compact face increases. This suggested that it was the attenuation that played a big role here, making the backscattering mainly reflects the compact layer thickness. Therefore, an attenuation correction term should be applied in order to reveal the relationship between AIB and porosity clearly, which might be studied in the future.

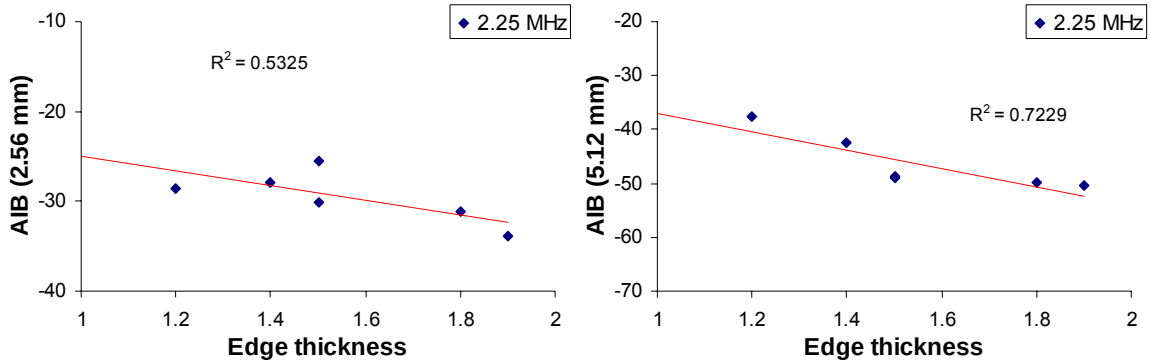

Figure 6-11 AIB changes with the thickness of the intact layer.

For the above analysis, some of the phantoms were excluded if their second big lobe (the separation between the first and second lobe as shown in figure 6-7 is determined by the

parameter “edge”) was overlapped with the first lobe which definitely affects the accuracy. This calls for an effective algorithm to be applied to solve the signal overlapping problem for future study.

In summary of the reflection ultrasound study, three transducer frequencies were used to measure the ultrasound backscattering from the short bone mimicking phantoms. Sound wave incidence from both the porous face and the flat face were studied. The results showed that the backscattering coefficients, both IRC and AIB, changed with porosity linearly when the wave incidence was from the porous face. On the other hand, when the wave incidence was from the compact face, the IRC representing the compact face properties was independent of porosity and compact face thickness. However, the AIB decreased with the compact face thickness of the phantoms, which suggested that to study the effect of porosity on the AIB, an attenuation correction term should be applied in order to compensate the effect of attenuation. Techniques regarding the dividing of overlapping signals and attenuation compensation would improve the accuracy of the results.

6.1.4 UCR measurement

Besides of the transmission ultrasound and reflection ultrasound measurements, the Ultrasound Critical-angle Reflectometry (UCR) sample machine was also utilized to detect the properties of the patella-mimic phantoms. In the home-made UCR sample machine (Figure 6-12), six motors control the axial movements (along the X, Y, Z axis, respectively) and rotations (in the X-Z, Y-Z and X-Y plane, with rotation angle denoted by Θ, Φ and Ψ, respectively) of the object holding by the sample holder. A transducer is mounted at 30º with

the vertical axis. An array of transducer elements are used to receive the signal reflected from the surface of the sample. The received signals are then sampled and digitized by the Data Acquisition System and sent to the computer for further analysis. The system is controlled by customized LabVIEW® software which enables the automation of sample movement and data acquisition.

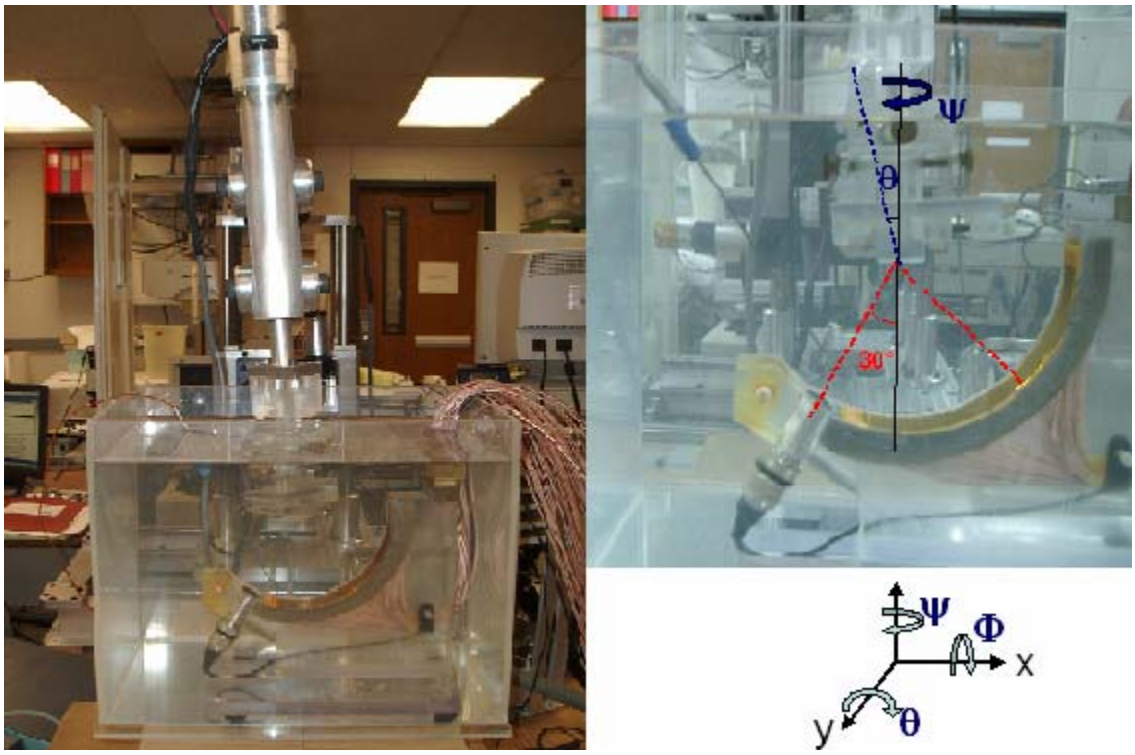

Figure 6-12 UCR sample machine (A) and the detailed view of ultrasound transducer and receiver array (B).

Figure 6-13 shows the results of the speed of sound (SOS) measurements using the UCR sample machine for solid cubes made by different kind of plastics. These results were compared to the velocity measured by QUS method (Table 6-2).

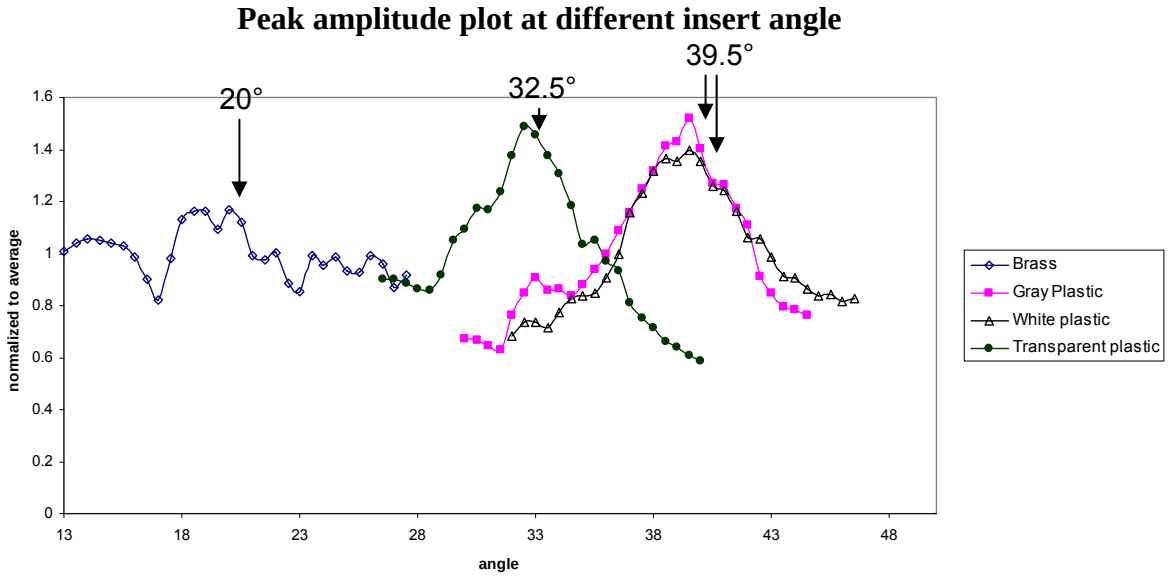

Figure 6-13 Plot of detected peak amplitude of received signal changes with ultrasound insert angle using UCR sample machine.

Table 6-2 Comparison of the value of SOS obtained by UCR method and QUS method.

	Critical Angle	**SOS from UCR**	**SOS from QUS**
Brass	20°	4327 m/s	4329 m/s
HDPL	32.5°	2755 m/s	2751 m/s
Plastics with glass particles	39.5°	2327 m/s	2499 m/s
Normal plastics	39.5°	2327 m/s	2370 m/s

As seen in Table 6-2, there's no significant difference between the results from the UCR method and QUS method for except for the white plastic which contains some tiny glass particles.

Then the nine porous acrylic plastic phantoms were measured using the UCR sample machine. The measurement was done in the water bath at room temperature around 20 ºC with 1 ºC variation.

Raw data from the UCR measurement shows how the intensity of the reflected ultrasound wave changes as the incident angle increases (Figure 6-14)

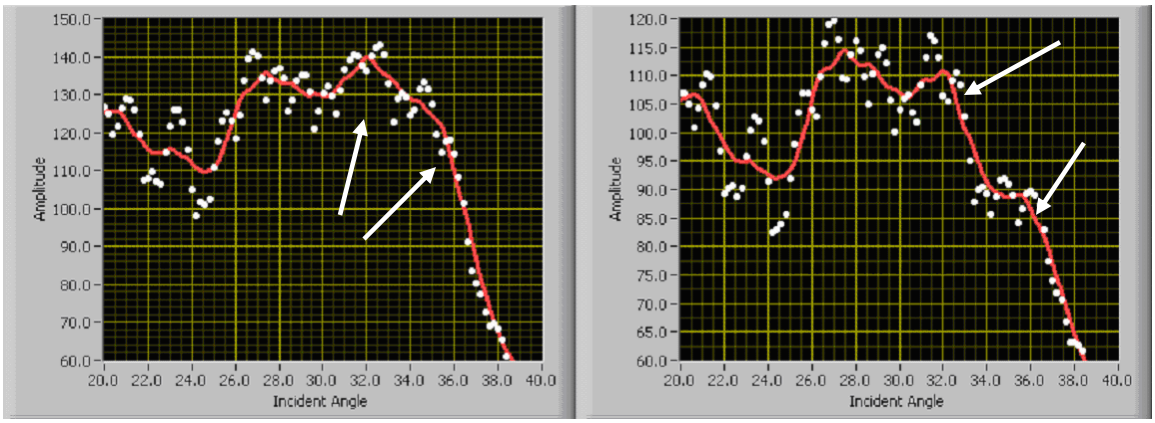

Figure 6-14 UCR measurements of the compact face (left) and porous face (right) of a shot bone mimicking phantom show the reflection ultrasound wave changes with incident angle. e, respectively, in each case. The white arrows indicate the first and second critical angle.

Figure 6-15 and 6-16 show the result of the UCR measurement from both the flat layer and the porous layer of the acrylic short bone mimicking phantoms. The group velocity was calculated using the critical angles obtained as from figure 6-14.

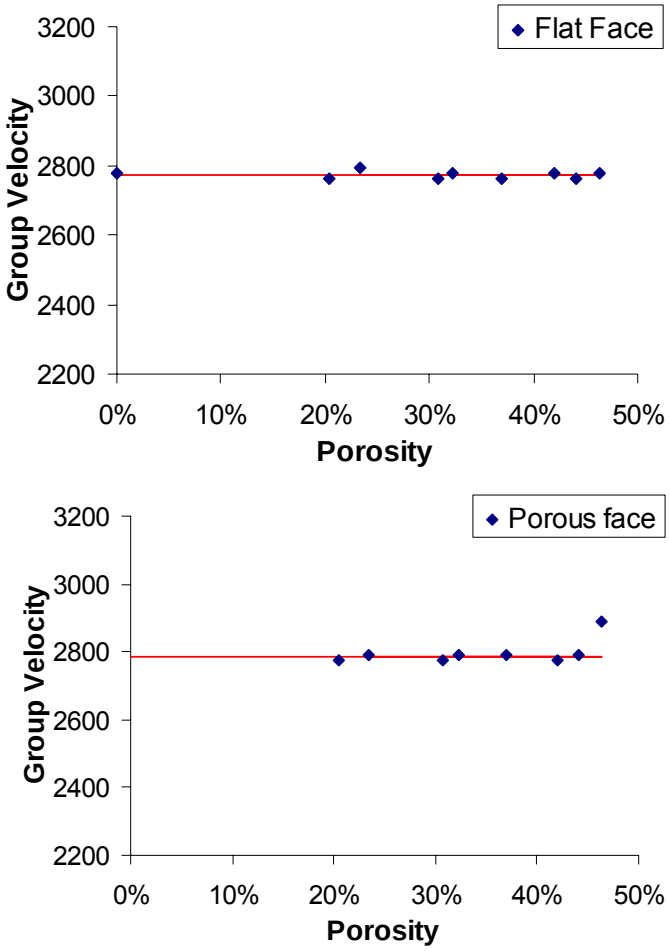

Figure 6-15 Velocity calculated based on the first critical angle in figure 6-17.

As shown in figure 6-15, the obtained velocity corresponding to the first critical angle was a constant of 2772.3 ± 10.8 m/s for the flat face measurement and 2786.2 ± 37.6 m/s for the porous face measurement, which were in agreement with each other. The obtained velocities also agreed with the SOS of pure acrylic plastics (2730 m/s) given by other sources (http://www.bamr.co.za/velocity20of%20materials.shtml).This indicates that the first critical angle mainly reflects the material property of the pore frame/skeleton.

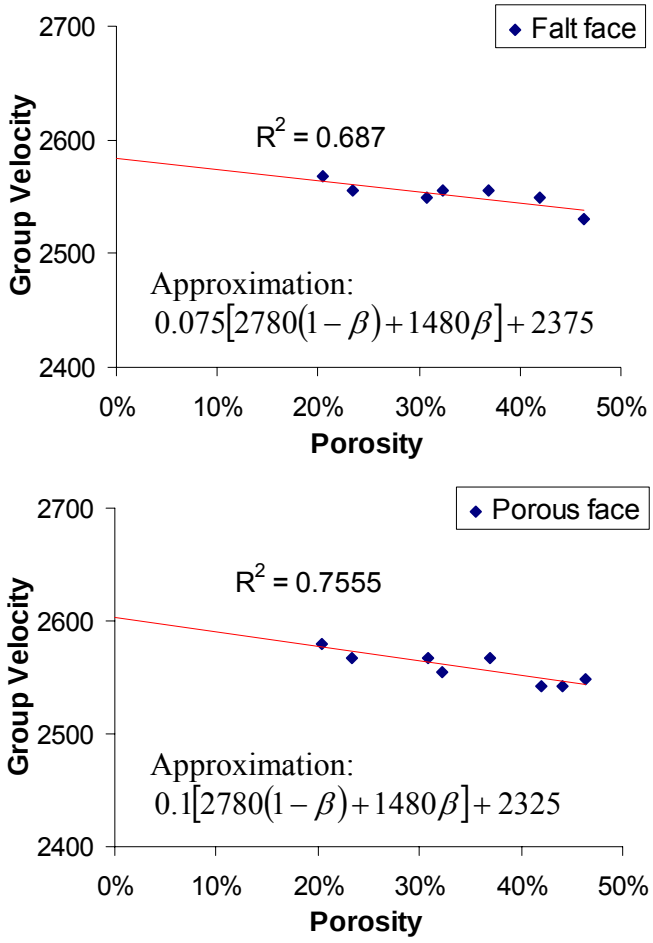

Figure 6-16 Velocity calculated based on the second critical angle in figure 6-17.

Figure 6-16 shows the velocity determined by the second critical angle presented a trend of decrease as the porosity increased. This trend could be well characterized by the linear fitting of bulk velocity $C_b = C_s(1-\beta)+C_f\beta$, in terms of the SOS in the solid material C_s (acrylic plastics, ~2780 m/s) and fluid C_f (water, ~1480 m/s at 20 ºC) as well as the porosity of the phantom β. Therefore the second critical angle represents the bulk property of the porous phantom.

Figure 6-17 shows the amplitude of the reflected ultrasound signal at the first and second critical angles for the porous face measurement of the phantoms. For both cases, the amplitude decreases linearly as the porosity increase. This linear relationship at the first critical angle ($R^2 = 0.93$) is much better than that at the second critical angle ($R^2 = 0.55$).

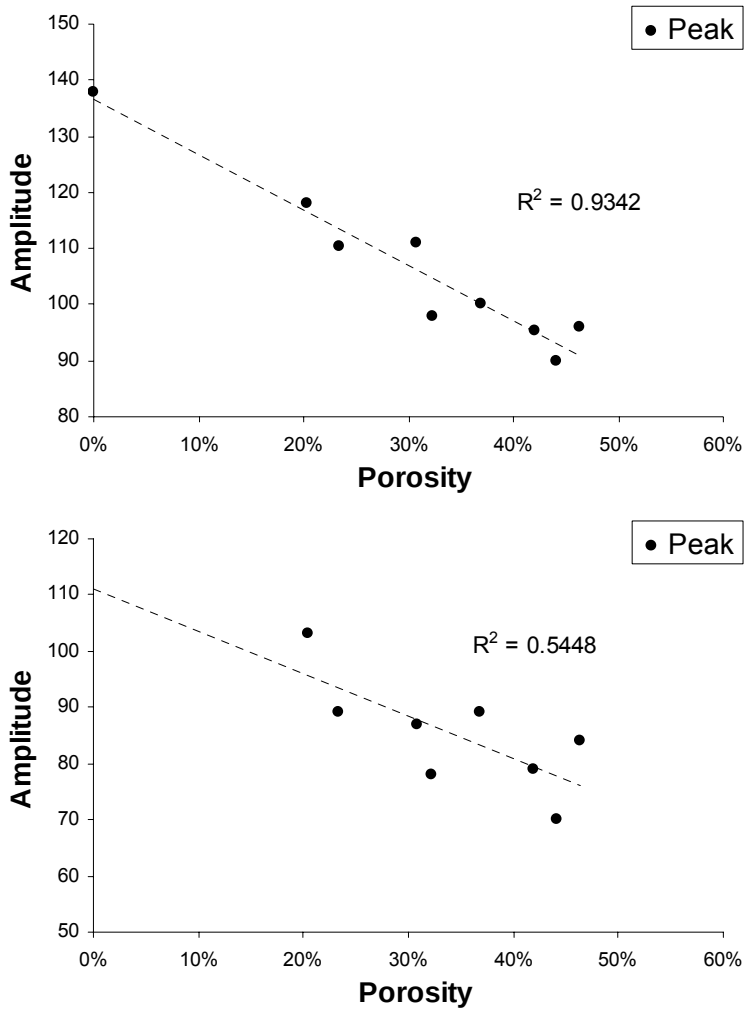

Figure 6-17 Amplitude measured by the UCR sample machine corresponding to the first (top) and second (bottom) critical angles.

Table 6-3 is the summary of the relationship between UCR results and phantom porosity. The UCR method detects two critical angles. The first critical angle, corresponding to the solid velocity, was independent of porosity, but its amplitude was strongly related to porosity (R^2 = 0.93). On the other hand, the second critical, corresponding to bulk velocity, was strongly related to porosity (R^2 = 0.76), but the correlation between its amplitude and the porosity was weak (R^2 = 0.54).

Table 6-3 Summary of the relationship between UCR results and phantom porosity

	Velocity	Amplitude
1st critical angle	Solid velocity; Independent	Strong (R^2 = 0.93)
2nd critical angle	Bulk velocity; Strong (R^2 = 0.76)	Weak (R^2 = 0.54)

Figure 6-18 shows how the velocity obtained from the UCR measurement is related to the backscattering coefficient from the reflection ultrasound measurement. The higher the porosity, the lower the bulk velocity and the smaller the backscatter parameters. Therefore, the measurement by the UCR sample machine was in agreement with the backscattering measurement using pulse-echo ultrasound method using lower frequency.

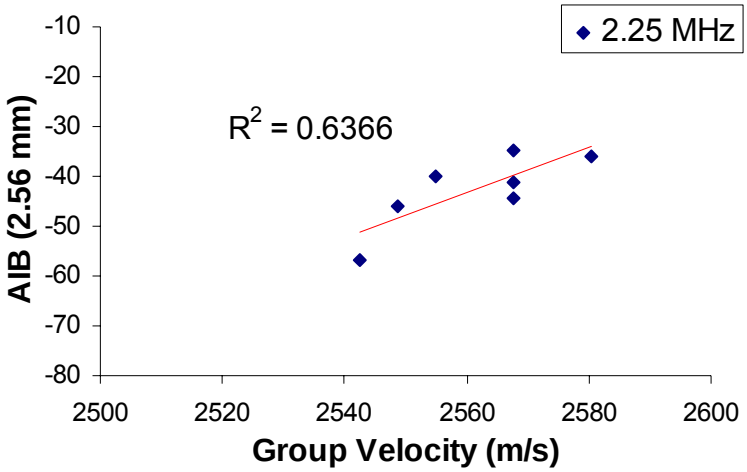

Figure 6-18 Results of the UCR velocity measurement and backscattering measurement are good related.

6.2 Ex vivo patella experiment

Patella is a typical short bone that is mainly composed of cancellous bones. It is also one of the preferred sites for the diagnosis of osteoporosis (Heaney, Avioli et al. 1989; Stegman, Heaney et al. 1994; Stegman, Heaney et al. 1995; Stegman, Heaney et al. 1995; Stegman, Davies et al. 1996). For the *ex vivo* short bone sample study, the porcine patella samples were measured by ultrasonic methods including the reflection ultrasound method and the UCR method.

6.2.1 Material preparation

Three intact porcine patella samples were obtained from a grocery store. For preparation, most of the surrounding tendon and soft tissues were removed, leaving the anterior and posterior aspects intact. The specimens were immersed in 99.9% ethanol for three weeks to get rid of the rest soft tissues. Then they were immersed in acetic acetate for 3 days so that the surrounded tendon was softened and peeled off. After cleaning, these patella samples were kept in 99.9% ethanol in room temperature before experiment (Figure 6-19).

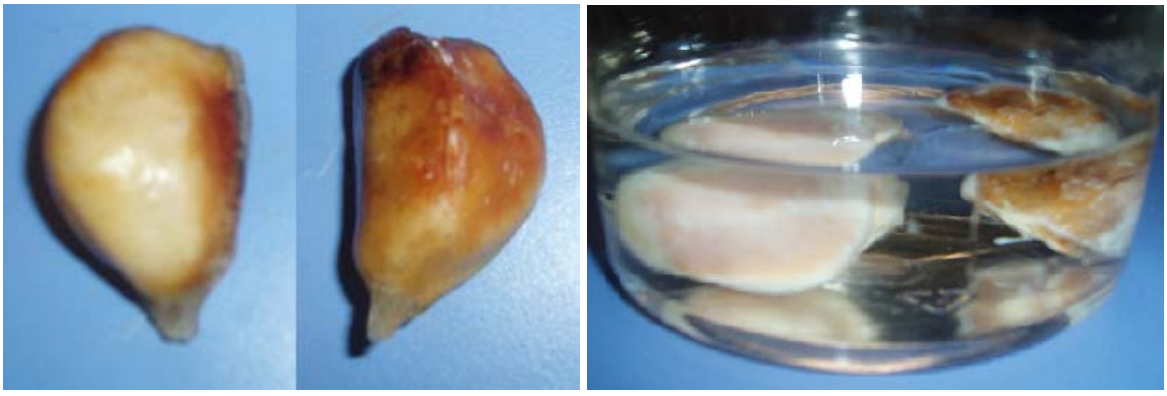

Figure 6-19 Views of a porcine patella sample (Left). The patella samples were kept in 99.9% ethanol in room temperature (Right).

The MicroCT image of the patella sample shown in figure 6-19 (left) was taken (Figure 6-20). This MicroCT image was taken at the Ohio State University.

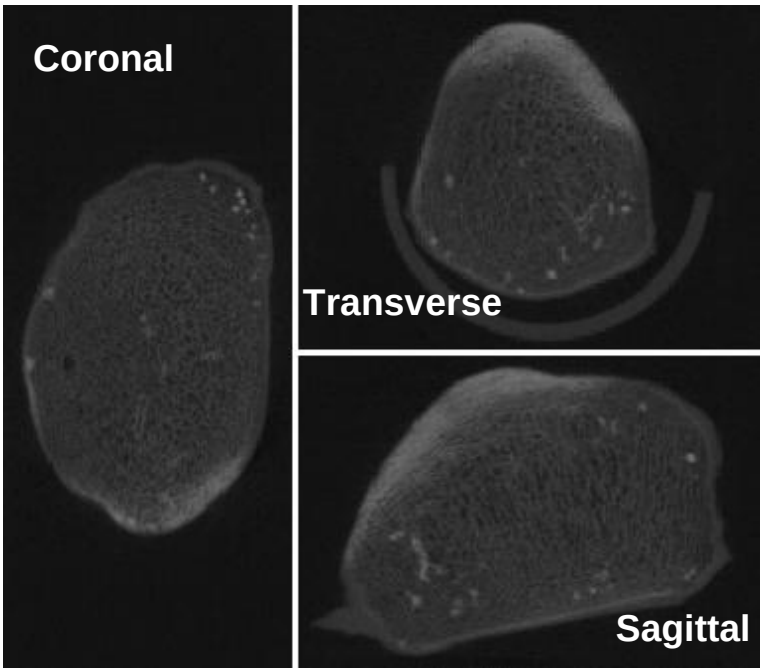

Figure 6-20 MicroCT image of one pork patella.

Fig 6-20 clearly shows that the patella is mainly composed of cancellous bone, which is surrounded by a very thin layer of cortical bone. The trabecular network inside the patella is not homogenous; the center part has slightly bigger porosity, and the anterior part has much bigger density.

Due to the thickness of the patella in both anterior/posterior (AP) direction (about 2.5 cm) and the medial/lateral (ML) direction (about 2 cm), the ultrasound signal could not penetrate the patella specimens even with the maximum intensity that could generated by the PANAMETRICS pulser/receiver being used. So QUS measurement couldn't be done with patella.

6.2.2 Reflection ultrasound measurement

The ultrasound backscattering from the patella samples was assessed via the reflection ultrasound measurement, and characterized by Integrated Reflection Coefficient (IRC) and Apparent Integrated Backscatter (AIB).

For the reflection ultrasound measurement on patella samples, the experiment setup was similar to the one for short bone mimicking phantoms described in previous section. An unfocusing PCT transducer with the central frequency of 5 MHz and the diameter of 0.375" (Panametrics V326, Panametrics Inc., Waltham, MA, USA) was used.

The patella samples were immersed in water holding by a sample holder. The sample holder was controlled with a customized LabVIEW (LabVIEW 7.1, National Instruments, Austin, TX, USA) program to choose the ROIs in the phantoms. Five ROIs were measured for each patella sample. Measurements of the samples were conducted in the water bath maintained in the room temperature.

The AIBs were obtained by processing the data with my customized LabVIEW program. Statistic analysis was done in Microsoft Excel 2002 (Microsoft Corporation, Redmond, WA, USA).

Figure 6-21 shows all the reflected ultrasound signals from the five ROIs of the three patella samples. Because of the uneven surface and inhomogeneous interior of the patella samples, the reflected signals appear quite different for each measurement.

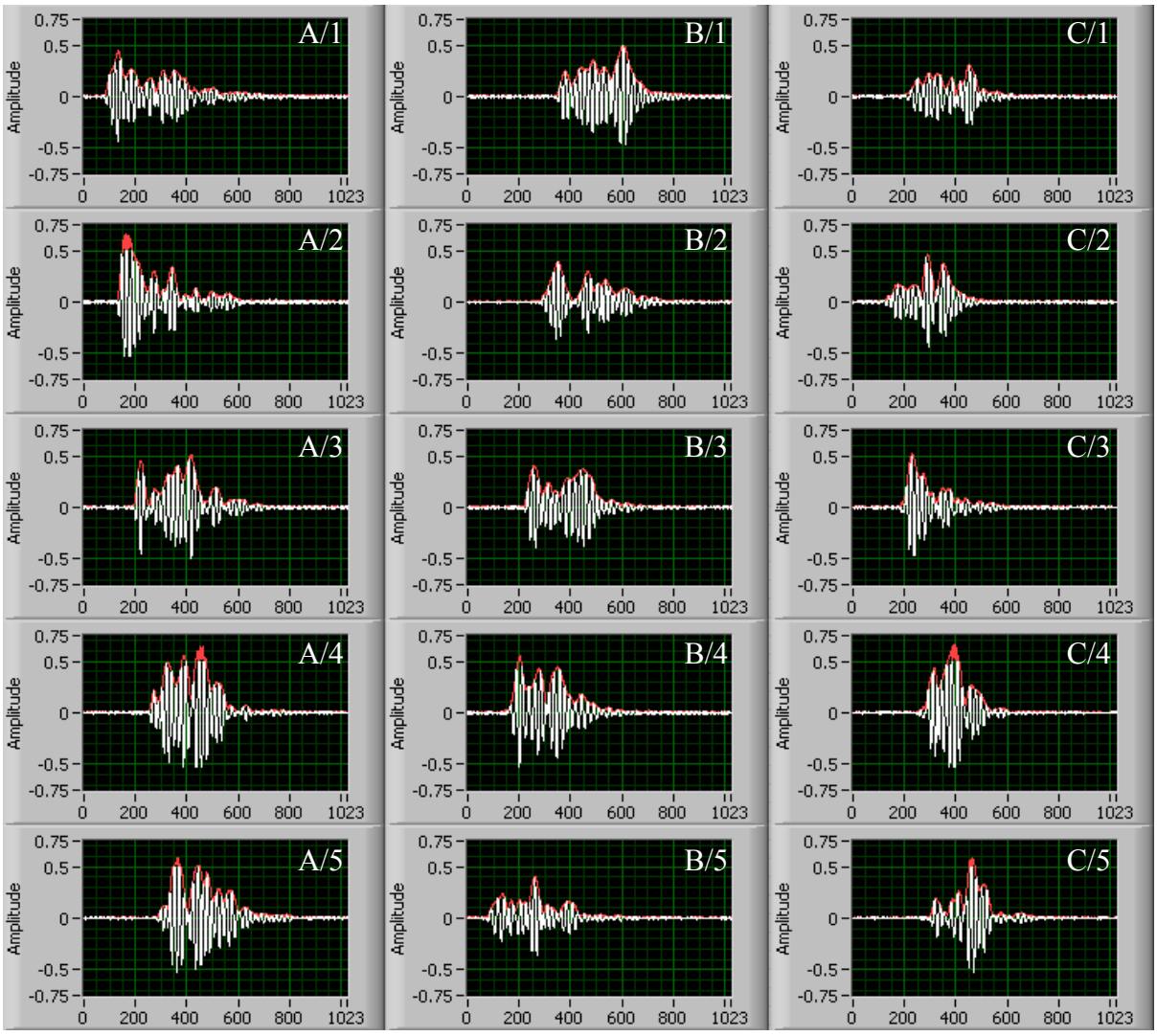

Figure 6-21 Reflected signals from each patella sample.

The backscattering parameters, IRC and AIB, were obtained by the same method as described before (Chapter 2). The results are shown in figure 6-22 and 6-23.

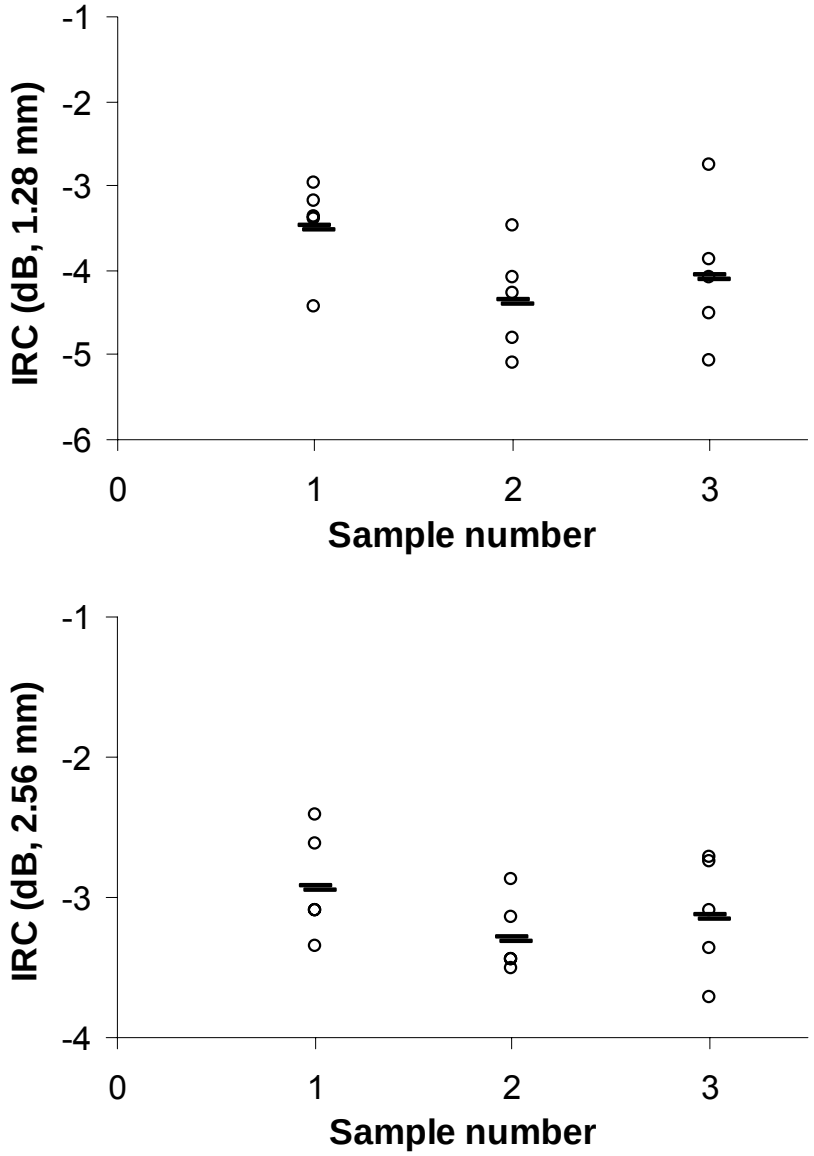

Figure 6-22 IRC of the patella sample measurements. Circles are the IRC for each ROI and the bars are the mean value for each patella sample.

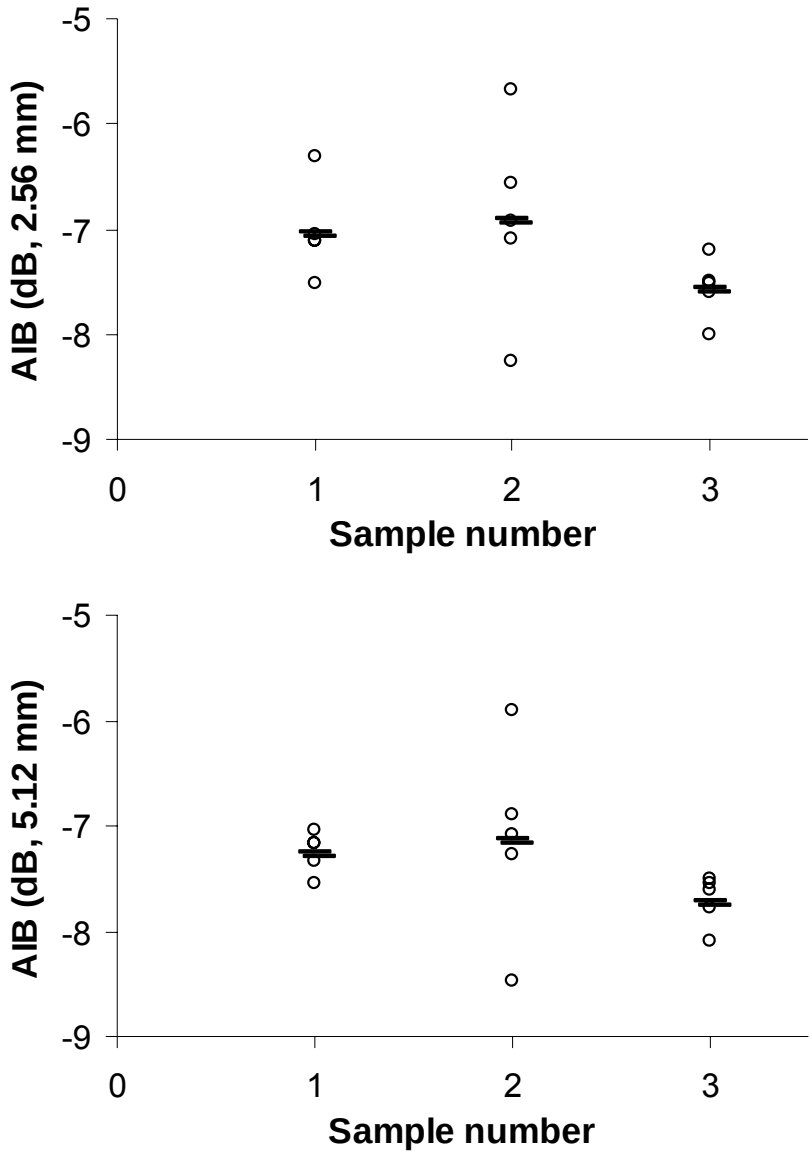

Figure 6-23 AIB of the patella sample measurements. Circles are the AIB for each ROI and the bars are the mean value for each patella sample.

As shown in figure 6-22 and 6-23, the individual calculation results may vary for different window sizes, but the relationship between the mean values of the three patella samples remains the same.

6.2.3 UCR measurement

The patella samples were also measured by the UCR sample machine. The measuring system was the same as the one that had been used for the short bone mimicking phantoms. The measurement was performed in a water tank at room temperature.

The bone sample was fixed by the sample holder of the UCR sample machine, assuming at (0, 0, 0) (Figure 6-24, left). The sample holder was then rotated in the y-z plane and the recorded amplitude vs. angle Φ was shown in figure 6-24 (right). The peaks of the plot represent a flat surface area that is preferred by the UCR method. Since the surface of the patella sample was not flat, multiple peaks presented. The ROIs defined by the Φs corresponding to the peaks were selected (in figure 6-24 are the site 1, 2 and 3, respectively).

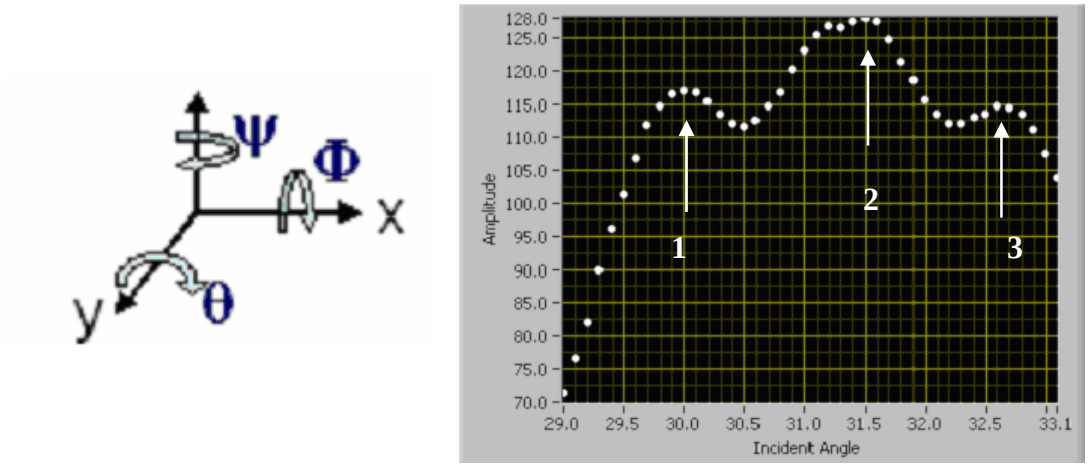

Figure 6-24 Determination of the ROIs of the patella samples. Arrows are the Φs for ROIs.

From the amplitude of the ultrasound signals reflected from the patella samples, the critical angle was determined by the sharp change in the slope of the reflected amplitude spectrum as shown by the arrows in figure 6-25.

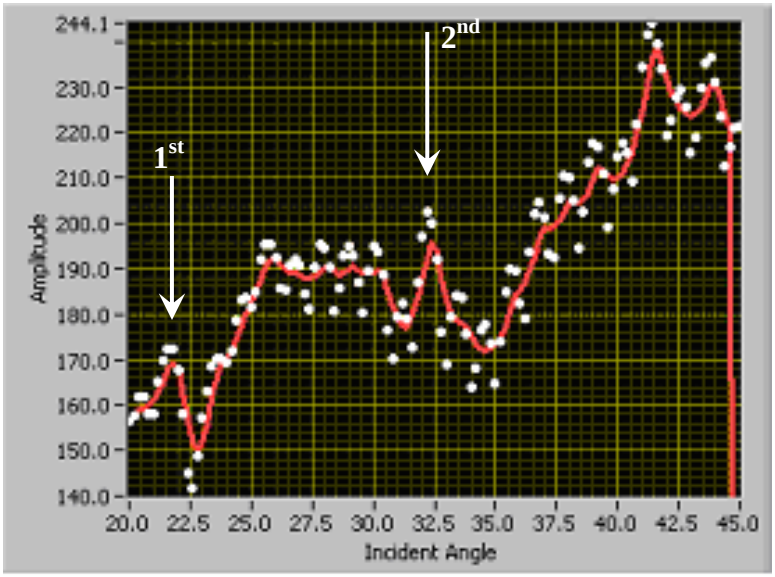

Figure 6-25 Typical response of the reflected amplitude vs incident angle for the porcine patella samples. The red line is the moving average (n = 8) of the raw data (white dots). The arrows indicate the first and second critical angle.

From the obtained critical angle and ultrasound velocity in water (1480 m/s at 20 °C), the ultrasound velocity in the patella was then calculated by Snell's law. And the results are shown in table 6-4.

Table 6-4 Determined critical angles and corresponding ultrasound velocities in the porcine patella samples.

Patella	Site	Critical angle 1	Velocity 1	Critical angle 2	Velocity 2
1	1	21.8	3985.27	32.4	2762.09
2	1	24.6	3555.29	32.6	2746.99
	2	25.2	3475.98	34.2	2633.06
	3	23.2	3756.90	34.4	2619.62
3	1	--	--	32.4	2762.09
	2	--	--	34.2	2633.06
	3	--	--	34.8	2593.24
	4	24.6	3555.29	--	--
Mean			3665.75 ± 206.65		2678.59 ± 74.75

No significant difference between the three samples was found by both the reflection ultrasound method and the UCR method. But this *ex vivo* study showed that these two ultrasonic methods are capable for the assessment of intact patella samples.

6.3 In vivo short bone experiment

After the feasibility of the ultrasonic methods in detecting short bone properties had been demonstrated, an *in vivo* study on human patella was finished. In this study, both the UCR measurement and reflection ultrasound measurement characterized by AIB were performed.

6.3.1 Study Subjects

Ten healthy volunteers were recruited in this study, including five male and five female. None of them has been previously diagnosed with bone diseases or other diseases that would affect bone properties. All of the subjects were young Asian, with a mean age of 30.4 (SD = 5.2) (Table 6-5). Patella of the right knee was measured for each subject.

Table 6-5 Age of the subjects.

	Male	**Female**
1	34	40
2	26	25
3	34	25
4	33	27
5	34	26
mean	32.2 ± 3.5	28.6 ± 6.4
total	30.4 ± 5.2	

6.3.2 Reflection ultrasound measurement

Firstly, the ultrasound backscattering from the patella of the subjects was assessed via the reflection ultrasound measurement, and characterized by the parameter of Apparent Integrated Backscatter (AIB).

The experiment setup was similar to the previous short bone mimicking phantom study and the *ex vivo* porcine patella sample study, as described in previous section. An unfocusing PCT transducer with the central frequency of 5 MHz and the diameter of 0.375" (Panametrics V326, Panametrics Inc., Waltham, MA, USA) was used. The AIBs were calculated by the customized LabVIEW program (LabVIEW 7.1, National Instruments, Austin, TX, USA).

The ultrasound transducer and the knee of the subjects were coupled by the ultrasound gel which works as a conductor between the ultrasound wave and the human body. Multiple (9~10) ROIs were measured for each subject (Figure 6-26). The measurements were conducted at room temperature.

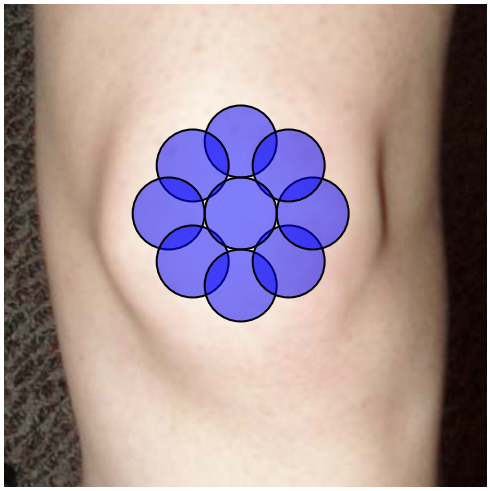

Figure 6-26 ROIs for the *in vivo* patella measurement. Circles represent the ROIs.

The AIBs were calculated according to the method described in Chapter 2. The windowed region of the reflected signal was chosen to exclude that aroused from the interaction between ultrasound wave and the skin, soft tissue, tendon and cortical layer. Two window sizes, 256 and 512 points, were applied, which correspond to a thickness of 3.5 mm and 7 mm, respectively. The results are shown in figure 6-27. A sex-related difference was observed in the average AIB among males and females.

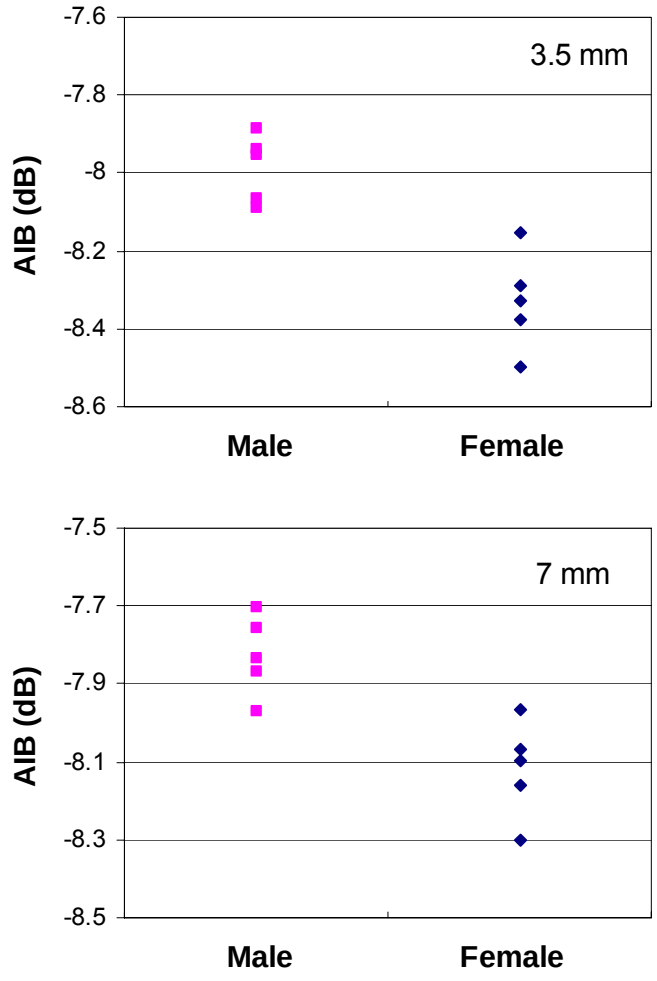

Figure 6-27 Sex-related difference for AIB.

6.3.3 UCR measurement

The *in vivo* UCR machine (Figure 6-28) was self-designed and made in Dr. Antich's lab. Two transducers are moving along an arch-shaped metal head to sweep over different incident angles. The transducer head can do three orthogonal axial movements as well as rotations and tilts. All the movements and data acquisition are controlled by a computer.

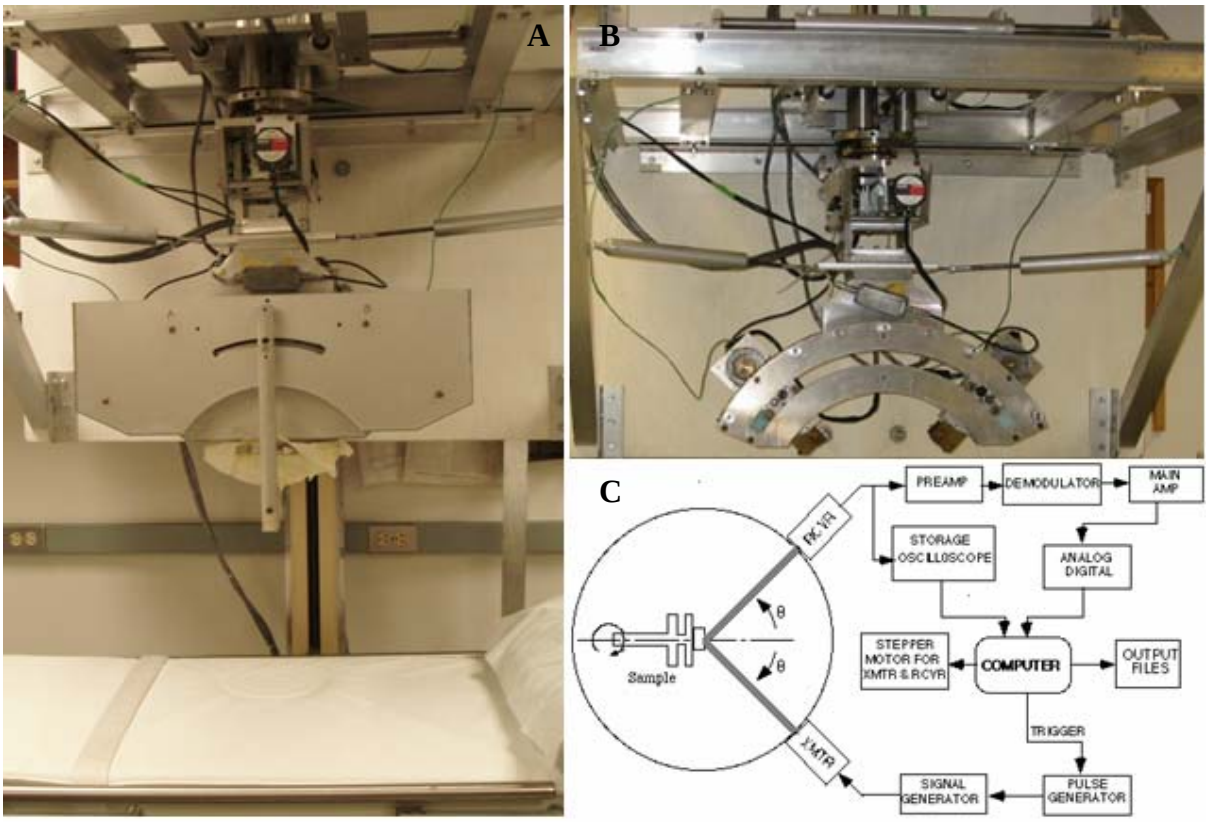

Figure 6-28 *In vivo* UCR machine for the study.

A: Outlook of the machine and experiment setup.
B: Interior view of the head of transducers and motors controlling the movements.
C: Block diagram of the machine.

The targeted position of measurement was determined as the center of the patella as shown in figure 6-29. The transducer head was rotated from 0º to 90º with a step of 15º. The subjects were instructed to lie down and stay still during the measurement. The measurements were performed at room temperature (19.7 ~ 21.8 ºC).

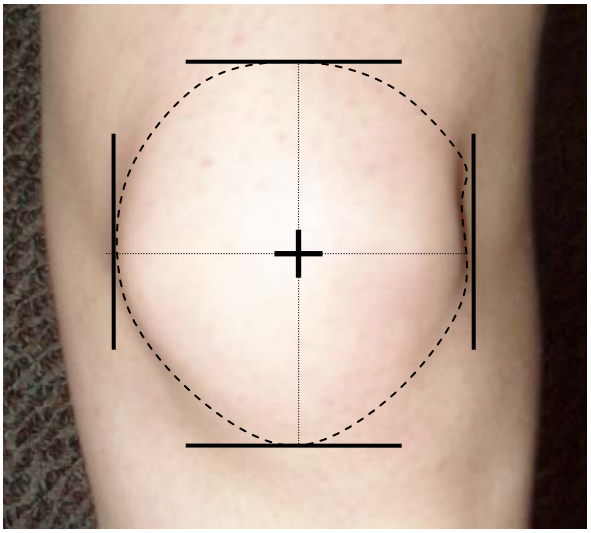

Figure 6-29 Determination of the target position for UCR measurement.

The results were recorded and processed using the data analyzing program written in IGOR Pro (Version 4, WaveMetrics, Inc., Lake Oswego, OR, USA). A sex-related difference was also found among males and females in the average ultrasound velocity in cancellous bone of the patella (Figure 6-30).

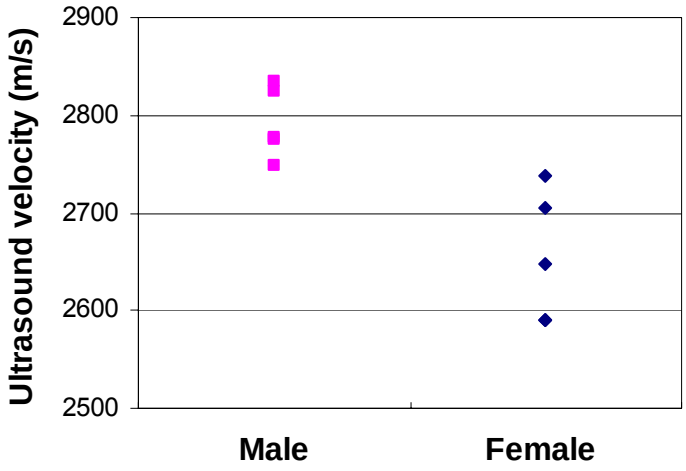

Figure 6-30 Sex-related difference for ultrasound velocity.

6.3.4 Discussion

Figure 6-31 shows the comparison between reflection ultrasound method and UCR method in assessing the human patella *in vivo*. For the plotted data, the correlation between AIB from the reflection ultrasound method and ultrasound velocity from UCR method was very good.

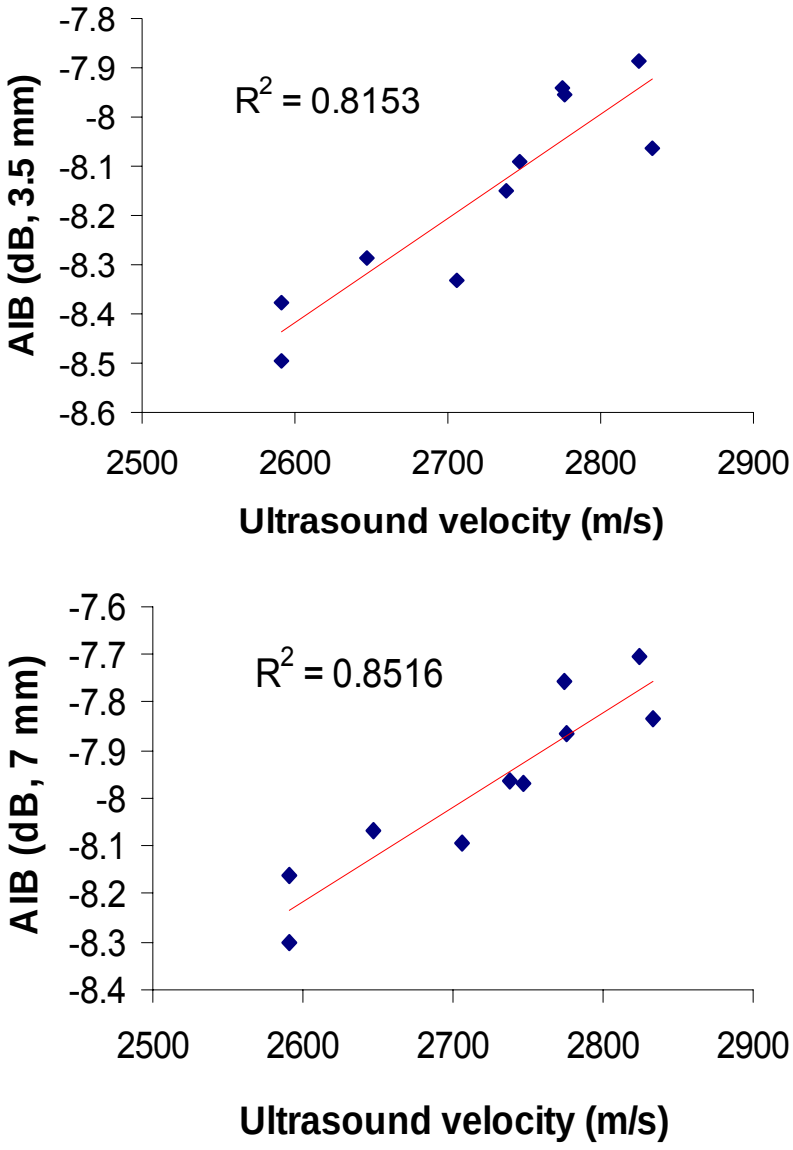

Figure 6-31 Correlation between average values of AIB and ultrasound velocity.

A strong correlation was found between the backscattering parameter (AIB) and ultrasound parameter (velocity) ($R^2 > 0.8$).

In summary of the short bone study, firstly, three ultrasound methods had been used to evaluate the short bone mimic phantoms, and their results were in agreement. The increase of porosity was linearly related to the decrease of bulk velocity and intensity related parameters of the ultrasound signals.

Patella as a typical short bone was evaluated by reflection ultrasound and UCR method for both *ex vivo* and *in vivo* study. The *ex vivo* porcine patella study showed the capability of both ultrasound methods in evaluating intact short bone. The *in vivo* human patella study showed a sex-related difference by both methods. The results of backscattering analysis and UCR measurement were in agreement with each other.

Chapter 7

General Conclusions and Future Directions

Osteoporosis, characterized by low bone density and high fracture risk, is the major bone disease in the world. Bone fracture associated by osteoporosis is one of the most common causes of disability and costs large amount of medical care expenses. Considering its properties such as low cost, high portability and non-ionizing nature, non-invasive ultrasound techniques have been investigated as diagnostic tools for osteoporosis by evaluating bone quality and biomechanical competence.

This dissertation used a reflection ultrasound method to evaluate non-BMD properties of cancellous bone, including porosity and the microstructure of the trabecular network, all of which are directly related to bone morphological change caused by osteoporosis and could result in better prediction of fracture risk.

7.1 Restatement of the objectives

The purpose of this dissertation is to use a non-invasive reflection ultrasound method to evaluate the porosity and microstructure of cancellous bones. To achieve this purpose, three specific aims have been proposed:

- Aim 1: Study of ultrasound backscattering in bone by computer simulation;
- Aim 2: Evaluate cancellous bone porosity by reflection ultrasound;
- Aim 3: Use ultrasound to evaluate short bone.

7.1.1 Aim 1: Ultrasound backscattering in bone by computer simulation

For aim 1, two different cancellous bone models, the cellular model and the wire model, were studied by computer simulations. It is the first computer simulation of the wired model, and also the first time that both the cellular model and wire model were simulated under the same circumstances for comparison purpose: same ultrasound transducers, same ultrasonic field being generated, and same scatter unit.

Both the cellular model and the wire model had proved their usefulness in evaluating the porosity and structural parameters of the porous material such as cancellous bone by analyzing the ultrasound backscattering. When the trabecular orientation was not perpendicular to the incident wave, both models predicted that the increase of porosity could explain about 90% of the variance of backscattering change. In case that the incident wave was normal to the trabecular, the wire model revealed that the trabecular thickness is the one parameter that is responsible for the change in the ultrasound backscattering.

7.1.2 Aim 2: Evaluate cancellous bone porosity by reflection ultrasound

Cancellous bone is a two phase material of the pore walls and the fatty marrow within the pores. To study the relationship between cancellous bone porosity and ultrasound backscattering, a computer simulation was firstly performed to obtain a theoretical prediction. The computer simulation showed that for the ideal case there is a linear

relationship between a material's porosity and the peak amplitude of the reflected ultrasound signal. The experimental results of the cancellous bone-mimicking phantom study agreed with that of the computer simulation. In the *in vitro* bovine cancellous bone measurement, the observed porosity depends upon the face interrogated showing heterogeneity of the porosity. Although the reflected signal from different faces of one single bone sample varies, there is still a good linear relationship between the porosity and the sample averaged parameters of the reflected ultrasound signal

In conclusion, the average porosity is correlated with the density, while the local porosity depends upon the heterogeneity of the cancellous bone. This orientation dependency may be used to monitor the density of cancellous bone and study the effect of the microarchitecture of cancellous bone.

It has been shown in this study that the average porosity of cancellous bone can be directly determined by the parameters of the ultrasound signals reflected from the bone, as there's a linear relationship between them.

7.1.3 Aim 3: Use ultrasound to evaluate short bone

To evaluate the short bones, which mainly composed of cancellous bone, firstly a phantom study was adopted to guide the measurement of bone properties. Three ultrasound methods, transmission ultrasound, reflection ultrasound, and Ultrasound Critical-angle Reflectometry, were utilized to evaluate the short bone mimic phantoms. Their results are in agreement: the increase of porosity is linearly related to the decrease of bulk velocity and intensity related ultrasound parameters.

Then patella as typical short bone, which has a thin layer of compact bone outside of the spongy interior, has been studied. The *ex vivo* evaluation of porcine patella samples showed the capability of both the reflection ultrasound method and the UCR method to assess intact short bone. The *in vivo* human patella study showed a sex-related difference by both methods. The results of the backscattering analysis and UCR measurement were in agreement with each other.

7.2 Conclusions

In this dissertation, non-invasive ultrasound methods have been utilized to evaluate the porosity and microstructure of bone. Three specific aims have been achieved. I have addressed the following conclusions and findings in my study.

- The cellular model of cancellous bone simulates the pores while the wire model simulates the trabeculae of the cancellous bone. These two models predict the ultrasound backscattering change from two different perspectives, but reach the same conclusion. This suggests that the reflection ultrasound method is not sensitive to the shape of a scatterer of wavelength size but to the spacing between scatterers.
- The Ultrasound Critical-angle Reflectometry detects two critical angles. The first critical angle, corresponding to the solid ultrasound velocity is independent of porosity, but its amplitude is strongly related to porosity; the second critical angle, corresponding to bulk ultrasound velocity, is strongly related to porosity, but its amplitude is weakly related to porosity. The choice of UCR parameters for analysis depends upon the purpose of the study.

- Results of the *in vitro* cancellous bone study using the reflection ultrasound method is in agreement with those of the computer simulations and phantom studies. Also, results of the *ex vivo* and *in vivo* short bone studies using the reflection ultrasound method is in agreement with that of the UCR method. This suggests that reflection ultrasound can be an effective tool for assessing bone properties *in vivo*.

7.3 Future Directions

The dissertation has demonstrated the feasibility of a reflection ultrasound method in detecting cancellous bone and short bone properties both *in vitro* and *in vivo*, as well as from the theoretical basis. However, there're still many works that could be done in the future beyond this dissertation.

Computer simulation models are promising in studying the effects of different structural parameters of cancellous bone, as it largely simplifies the complex microarchitecture of cancellous bone. It could be further explored to reveal the individual effects of more structural parameters independently.

Although the reflection ultrasound method has shown its capability in detecting cancellous bone and short bone properties both *in vitro* and *in vivo*, advanced signal processing algorithms for the backscattered ultrasound signals could be developed, and coefficients that are more precise and sensitive to porosity changes could be studied.

As an effective tool for assessing bone properties *in vivo*, the reflection method could be applied to patients with osteoporosis in the future to evaluate its feasibility and effectiveness in regular clinical use.

Bibliography

(1994). Assessment of Fracture Risk and its Application to Screening for Postmenopausal Osteoporosis. Report of a WHO Study Group. Technical Report Series, World Health Organization**:** 1-129.

(2004). Bone Health and Osteoporosis: A Report of the Surgeon General. Services, U. S. d. o. H. a. H., HHS press 186-213.

Antich, P. and Mehta, S. (1997). "Ultrasound critical-angle reflectometry (UCR): a new modality for functional elastometric imaging." Phys Med Biol **42**(9): 1763-77.

Antich, P. P., Anderson, J. A., Ashman, R. B., et al. (1991). "Measurement of mechanical properties of bone material *in vitro* by ultrasound reflection: methodology and comparison with ultrasound transmission." J Bone Miner Res **6**(4): 417-26.

Antich, P. P., Pak, C. Y., Gonzales, J., et al. (1993). "Measurement of intrinsic bone quality *in vivo* by reflection ultrasound: correction of impaired quality with slow-release sodium fluoride and calcium citrate." J Bone Miner Res **8**(3): 301-11.

Attenborough, K. (1982). "Acoustical characteristics of porous materials." Physics Reports **82**(3): 179-227.

Barber, P. W. and Hill, S. S. (1990). Light scattering by particles: Computational methods. Singapore, World Scientific.

Baron, R. (2003). "General Principles of Bone Biology." Primer on the Metabolic BoneDiseases and Disorders of Mineral Metabolism **Chapter 1**: 1-8.

Berryman, J. G. (1980). "Confirmation of Biot's theory." Applied Physics Letters **37**(4): 382-384.

Biot, M. A. (1956). "Theory of Propagation of Elastic Waves in a Fluid-Saturated Porous Solid. I. Low-Frequency Range." The Journal of the Acoustical Society of America **28**(2): 168-178.

Biot, M. A. (1956). "Theory of Propagation of Elastic Waves in a Fluid-Saturated Porous Solid. II. Higher Frequency Range." The Journal of the Acoustical Society of America **28**(2): 179-191.

Boivin, G. and Meunier, P. J. (2002). "The degree of mineralization of bone tissue measured by computerized quantitative contact microradiography." Calcif Tissue Int **70**(6): 503-11.

Bossy, E., Padilla, F., Peyrin, F., et al. (2005). "Three-dimensional simulation of ultrasound propagation through trabecular bone structures measured by synchrotron microtomography." Phys Med Biol **50**(23): 5545-56.

Bouxsein, M. L., Kaufman, J., Tosi, L., et al. (2004). Recommendations for Optimal Care of the Fragility Fracture Patient to Reduce the Risk of Future Fracture. **12:** 385-395.

Brown, J. P. (2003). "Osteoporosis in children: 2002 guidelines do not apply." CMAJ **168**(6): 676-.

Burr, D. B. and Turner, C. H. (2003). Biomechanics of Bone. Primer on the Metabolic Bone Diseases and Disorders of Mineral Metabolism. Favus, M. J. Washington, American Society for Bone and Mineral Research**:** 58-64.

Chaffai, S., Peyrin, F., Berger, G., et al. (1999). Variation of human cancellous bone ultrasonic properties with density and micro-structure.

Chaffai, S., Peyrin, F., Nuzzo, S., et al. (2002). "Ultrasonic characterization of human cancellous bone using transmission and backscatter measurements: relationships to density and microstructure." Bone **30**(1): 229-37.

Chapelon, J. Y., Ribault, M., Birer, A., et al. (1999). "Treatment of localised prostate cancer with transrectal high intensity focused ultrasound." European Journal of Ultrasound **9**(1): 31-38.

Christiansen, J. P. and Lindner, J. R. (2005). "Molecular and cellular imaging with targeted contrast ultrasound." Proceedings of the IEEE **93**(4): 809-818.

Cooper, C. (2003). Epidemiology of Osteoporosis. Primer on the Metabolic Bone Diseases and Disorders of Mineral Metabolism. Favus, M. J. Washington, American Society for Bone and Mineral Research**:** 307-313.

Cortet, B., Boutry, N., Dubois, P., et al. (2004). "Does quantitative ultrasound of bone reflect more bone mineral density than bone microarchitecture?" Calcif Tissue Int **74**(1): 60-7.

Draine, B. T. and Flatau, P. J. (1994). "Discrete-dipole approximation for scattering calculations." J. Opt. Soc. Am. A **11**(4): 1491.

Enns, P., Pavlidis, T., Stahl, J. P., et al. (2004). "Sonographic detection of an isolated cuboid bone fracture not visualized on plain radiographs." J Clin Ultrasound **32**(3): 154-7.

Epstein, D. M., Dalinka, M. K., Kaplan, F. S., et al. (1986). "Observer variation in the detection of osteopenia." Skeletal Radiology **15**(5): 347-349.

Fellah, Z. E., Berger, S., Lauriks, W., et al. (2003). "Measuring the porosity and the tortuosity of porous materials via reflected waves at oblique incidence." J Acoust Soc Am **113**(5): 2424-33.

Fellah, Z. E., Chapelon, J. Y., Berger, S., et al. (2004). "Ultrasonic wave propagation in human cancellous bone: application of Biot theory." J Acoust Soc Am **116**(1): 61-73.

Fellah, Z. E. A., Mitri, F. G., Depollier, C., et al. (2003). "Characterization of porous materials with a rigid frame via reflected waves." Journal of Applied Physics **94**(12): 7914-7922.

Fielding, K. T., Nix, D. A. and Bachrach, L. K. (2003). "Comparison of calcaneus ultrasound and dual X-ray absorptiometry in children at risk of osteopenia." J Clin Densitom **6**(1): 7-15.

Fyhrie, D. P. (2005). "Summary--Measuring "bone quality"." J Musculoskelet Neuronal Interact **5**(4): 318-320.

Gibson, L. J. (1985). "The mechanical behaviour of cancellous bone." J Biomech **18**(5): 317-28.

Glüer, C. C., Wu, C. Y. and Genant, H. K. (1993). "Broadband ultrasound attenuation signals depend on trabecular orientation: An *in vitro* study." Osteoporosis International **3**(4): 185-191.

Goodman, J. W. (1968). Introduction to Fourier Optics. New York, McGraw-Hill.

Haire, T. J. and Langton, C. M. (1999). "Biot theory: a review of its application to ultrasound propagation through cancellous bone." Bone **24**(4): 291-295.

Haire, T. J. and Langton, C. M. (1999). "Biot theory: a review of its application to ultrasound propagation through cancellous bone." Bone **24**(4): 291-5.

Hakulinen, M. A., Day, J. S., Toyras, J., et al. (2005). "Prediction of density and mechanical properties of human trabecular bone *in vitro* by using ultrasound transmission and backscattering measurements at 0.2-6.7 MHz frequency range." Phys Med Biol **50**(8): 1629-42.

Hans, D., Arlot, M. E., Schott, A. M., et al. (1995). "Do ultrasound measurements on the os calcis reflect more the bone microarchitecture than the bone mass?: a two-dimensional histomorphometric study." Bone **16**(3): 295-300.

Hans, D., Wu, C., Njeh, C. F., et al. (1999). "Ultrasound velocity of trabecular cubes reflects mainly bone density and elasticity." Calcif Tissue Int **64**(1): 18-23.

Haupt, G. and Haupt, A. (2003). "*In Vitro* Comparison of 4 Ultrasound Lithotripsy Devices." The Journal of Urology **170**(5): 1731-1733.

Heaney, R. P., Avioli, L. V., Chesnut, C. H., 3rd, et al. (1989). "Osteoporotic bone fragility. Detection by ultrasound transmission velocity." Jama **261**(20): 2986-90.

Hoffmeister, B. K., Jones, C. I., 3rd, Caldwell, G. J., et al. (2006). "Ultrasonic characterization of cancellous bone using apparent integrated backscatter." Phys Med Biol **51**(11): 2715-27.

Hoffmeister, B. K., Whitten, S. A., Kaste, S. C., et al. (2002). "Effect of collagen and mineral content on the high-frequency ultrasonic properties of human cancellous bone." Osteoporos Int **13**(1): 26-32.

Hosokawa, A. and Otani, T. (1997). "Ultrasonic wave propagation in bovine cancellous bone." J Acoust Soc Am **101**(1): 558-62.

Hosokawa, A. and Otani, T. (1998). "Acoustic anisotropy in bovine cancellous bone." J Acoust Soc Am **103**(5 Pt 1): 2718-22.

Hughes, E. R., Leighton, T. G., Petley, G. W., et al. (1999). "Ultrasonic propagation in cancellous bone: a new stratified model." Ultrasound Med Biol **25**(5): 811-21.

Hunerbein, M., Raschke, M., Haas, N. P., et al. (2000). "Three-dimensional ultrasonography: new prospects for ultrasound imaging of bone." The Lancet **355**(9198): 116-117.

Jensen, J. A. and Svendsen, N. B. (1992). "Calculation of pressure fields from arbitrarily shaped, apodized, and excited ultrasound transducers." Ultrasonics, Ferroelectrics and Frequency Control, IEEE Transactions on **39**(2): 262-267.

Jenson, F., Padilla, F., Peyrin, F., et al. (2004). Characterization of human femoral trabecular bone *in vitro* using transmission and backscatter ultrasound measurements.

Kaczmarek, M., Kubik, J. and Pakula, M. (2002). "Short ultrasonic waves in cancellous bone." Ultrasonics **40**(1-8): 95-100.

Katz, J. L. and Meunier, A. (1987). "The elastic anisotropy of bone." J Biomech **20**(11-12): 1063-70.

Lang, S. B. (1969). "Elastic coefficients of animal bone." Science **165**(890): 287-8.

Langton, C. M., Whitehead, M. A., Langton, D. K., et al. (1997). "Development of a cancellous bone structural model by stereolithography for ultrasound characterization of the calcaneus." Med Eng Phys **19**(7): 599-604.

Lee, K. I. and Choi, M. J. (2007). "Phase velocity and normalized broadband ultrasonic attenuation in Polyacetal cuboid bone-mimicking phantoms." J Acoust Soc Am **121**(6): EL263-9.

Lee, K. I., Hughes, E. R., Humphrey, V. F., et al. (2007). "Empirical angle-dependent Biot and MBA models for acoustic anisotropy in cancellous bone." Phys Med Biol **52**(1): 59-73.

Lee, K. I., Humphrey, V. F., Leighton, T. G., et al. (2007). "Predictions of the modified Biot-Attenborough model for the dependence of phase velocity on porosity in cancellous bone." Ultrasonics **46**(4): 323-330.

Lee, K. I., Roh, H. S. and Yoon, S. W. (2003). "Acoustic wave propagation in bovine cancellous bone: application of the Modified Biot-Attenborough model." J Acoust Soc Am **114**(4 Pt 1): 2284-93.

Lee, K. I. and Yoon, S. W. (2006). "Comparison of acoustic characteristics predicted by Biot's theory and the modified Biot-Attenborough model in cancellous bone." J Biomech **39**(2): 364-8.

Lin, W., Qin, Y. X. and Rubin, C. (2001). "Ultrasonic wave propagation in trabecular bone predicted by the stratified model." Ann Biomed Eng **29**(9): 781-90.

Lindsay, R. (1988). Sex steroids in the pathogenesis and prevention of osteoporosis. Osteoporosis: etiology, diagnosis and management. . Riggs BL, M. L. I. New York, Raven Press**:** 333-58.

Magarey, A. M., Boulton, T. J., Chatterton, B. E., et al. (1999). "Familial and environmental influences on bone growth from 11-17 years." Acta Paediatr **88**(11): 1204-10.

Marshall, D., Johnell, O. and Wedel, H. (1996). "Meta-analysis of how well measures of bone mineral density predict occurrence of osteoporotic fractures." BMJ **312**(7041): 1254-1259.

McKelvie, M. L. and Palmer, S. B. (1991). "The interaction of ultrasound with cancellous bone." Phys Med Biol **36**(10): 1331-40.

Mehta, S. and Antich, P. (1997). "Measurement of shear-wave velocity by ultrasound critical-angle reflectometry (UCR)." Ultrasound Med Biol **23**(7): 1123-6.

Mehta, S. S., Antich, P. P., Daphtary, M. M., et al. (2001). "Bone material ultrasound velocity is predictive of whole bone strength." Ultrasound Med Biol **27**(6): 861-7.

Mehta, S. S., Oz, O. K. and Antich, P. P. (1998). "Bone elasticity and ultrasound velocity are affected by subtle changes in the organic matrix." J Bone Miner Res **13**(1): 114-21.

Mohamed, M. M., Shaat, L. T. and Mahmoud, A. N. (2003). "Propagation of ultrasonic waves through demineralized cancellous bone." IEEE Trans Ultrason Ferroelectr Freq Control **50**(3): 279-88.

Mundy, G. R., Chen, D. and Oyajobi, B. O. (2003). Bone Remodeling. Primer on the Metabolic Bone Diseases and Disorders of Mineral Metabolism. Favus, M. J. Washington, American Society for Bone and Mineral Research**:** 46-58.

Nicholson, P. H. and Bouxsein, M. L. (2002). "Bone marrow influences quantitative ultrasound measurements in human cancellous bone." Ultrasound Med Biol **28**(3): 369-75.

Nicholson, P. H., Strelitzki, R., Cleveland, R. O., et al. (2000). "Scattering of ultrasound in cancellous bone: predictions from a theoretical model." J Biomech **33**(4): 503-6.

Nicholson, P. H. F., Haddaway, M. J. and Davie, M. W. J. (1994). "The dependence of ultrasonic properties on orientation in human vertebral bone." Physics in Medicine and Biology **39**(6): 1013-1024.

Njeh, C. F., Boivin, C. M. and Langton, C. M. (1997). "The role of ultrasound in the assessment of osteoporosis: a review." Osteoporos Int **7**(1): 7-22.

Njeh, C. F., Fuerst, T., Diessel, E., et al. (2001). "Is quantitative ultrasound dependent on bone structure? A reflection." Osteoporos Int **12**(1): 1-15.

Njeh, C. F., Hans, D., Fuerst, T., et al. (1999). Quantitative Ultrasound: assessment of osteoporosis and bone status Informa Healthcare.

Norman, M. E. (2003). Juvenile Osteoporosis. Primer on the Metabolic Bone Diseases and Disorders of Mineral Metabolism. Favus, M. J. Washington, American Society for Bone and Mineral Research**:** 382-386.

Padilla, F. and Laugier, P. (2005). "Recent developments in trabecular bone characterization using ultrasound." Curr Osteoporos Rep **3**(2): 64-9.

Parfitt, A. M. (1987). "Trabecular bone architecture in the pathogenesis and prevention of fracture." American Journal of Medicine **82**(1B): 68-72.

Pereira, W. C., Bridal, S. L., Coron, A., et al. (2004). "Singular spectrum analysis applied to backscattered ultrasound signals from *in vitro* human cancellous bone specimens." IEEE Trans Ultrason Ferroelectr Freq Control **51**(3): 302-12.

Prevrhal, S., Fuerst, T., Fan, B., et al. (2001). "Quantitative ultrasound of the tibia depends on both cortical density and thickness." Osteoporos Int **12**(1): 28-34.

Prins, S. H., Jorgensen, H. L., Jorgensen, L. V., et al. (1998). "The role of quantitative ultrasound in the assessment of bone: a review." Clin Physiol **18**(1): 3-17.

Rauch, F., Travers, R., Norman, M. E., et al. (2000). "Deficient bone formation in idiopathic juvenile osteoporosis: a histomorphometric study of cancellous iliac bone." J Bone Miner Res **15**(5): 957-63.

Rico, H., Hernandez, E. R., Paez, E., et al. (2001). "Do ultrasound measurements reflect bone microarchitecture rather than bone mass?: An *in vitro* study of the rat femur with the use of ultrasound, densitometry, and histomorphometry." Invest Radiol **36**(6): 323-6.

Riggs, B. L., Khosla, S. and Melton, L. J. (1998). "A Unitary Model for Involutional Osteoporosis: Estrogen Deficiency Causes Both Type I and Type II Osteoporosis in Postmenopausal Women and Contributes to Bone Loss in Aging Men." Journal of Bone and Mineral Research **13**(5): 763-773.

Roberjot, V., Laugier, P., Droin, P., et al. (1996). Measurement of integrated backscatter coefficient of trabecular bone.

Roh, H. S. and Yoon, S. W. (2004). "Acoustic diagnosis for porous medium with circular cylindrical pores." J Acoust Soc Am **115**(3): 1114-24.

Rosenschein, U., Furman, V., Kerner, E., et al. (2000). Ultrasound Imaging-Guided Noninvasive Ultrasound Thrombolysis : Preclinical Results. **102:** 238-245.

Schlienger, R. G. and Meier, C. R. (2003). "HMG-CoA reductase inhibitors in osteoporosis: do they reduce the risk of fracture?" Drugs & Aging **20**(5): 321-336.

Schoenberg, M. (1984). "Wave propagation in alternating solid and fluid layers." Wave Motion **6**(3): 303-320.

Seeman, E. and Delmas, P. D. (2006). "Bone quality--the material and structural basis of bone strength and fragility." N Engl J Med **354**(21): 2250-61.

Specker, B. L. and Schoenau, E. (2005). "Quantitative bone analysis in children: current methods and recommendations." J Pediatr **146**(6): 726-31.

Speiser, P. W., Clarson, C. L., Eugster, E. A., et al. (2005). "Bisphosphonate treatment of pediatric bone disease." Pediatr Endocrinol Rev **3**(2): 87-96.

Stegman, M. R., Davies, K. M., Heaney, R. P., et al. (1996). "The association of patellar ultrasound transmissions and forearm densitometry with vertebral fracture, number and severity: the Saunders County Bone Quality Study." Osteoporos Int **6**(2): 130-5.

Stegman, M. R., Heaney, R. P. and Recker, R. R. (1995). "Comparison of speed of sound ultrasound with single photon absorptiometry for determining fracture odds ratios." J Bone Miner Res **10**(3): 346-52.

Stegman, M. R., Heaney, R. P., Recker, R. R., et al. (1994). "Velocity of ultrasound and its association with fracture history in a rural population." Am J Epidemiol **139**(10): 1027-34.

Stegman, M. R., Heaney, R. P., Travers-Gustafson, D., et al. (1995). "Cortical ultrasound velocity as an indicator of bone status." Osteoporos Int **5**(5): 349-53.

Stoll, R. D. and Bryan, G. M. (1970). "Wave Attenuation in Saturated Sediments." The Journal of the Acoustical Society of America **47**(5B): 1440-1447.

Swartz, S. M., Parker, A. and Huo, C. (1998). "Theoretical and empirical scaling patterns and topological homology in bone trabeculae." J Exp Biol **201**(Pt 4): 573-90.

Ulrich, D., van Rietbergen, B., Laib, A., et al. (1999). "The ability of three-dimensional structural indices to reflect mechanical aspects of trabecular bone." Bone **25**(1): 55-60.

Vaezy, S., Andrew, M., Kaczkowski, P., et al. (2001). "Image-guided acoustic therapy." Annual Review of Biomedical Engineering **3**(1): 375-390.

Wang, C. L., Shieh, J. Y., Wang, T. G., et al. (1999). "Sonographic detection of occult fractures in the foot and ankle." J Clin Ultrasound **27**(8): 421-5.

Wear, K. A. (2001). "A stratified model to predict dispersion in trabecular bone." IEEE Trans Ultrason Ferroelectr Freq Control **48**(4): 1079-83.

Wear, K. A. (2003). "Characterization of trabecular bone using the backscattered spectral centroid shift." IEEE Trans Ultrason Ferroelectr Freq Control **50**(4): 402-7.

Wear, K. A. (2004). "Measurement of dependence of backscatter coefficient from cylinders on frequency and diameter using focused transducers--with applications in trabecular bone." J Acoust Soc Am **115**(1): 66-72.

Wear, K. A. (2005). "The dependencies of phase velocity and dispersion on trabecular thickness and spacing in trabecular bone-mimicking phantoms." J Acoust Soc Am **118**(2): 1186-92.

Wear, K. A. (2007). "The dependence of time-domain speed-of-sound measurements on center frequency, bandwidth, and transit-time marker in human calcaneus *in vitro*." J Acoust Soc Am **122**(1): 636-44.

Wear, K. A. and Garra, B. S. (1998). "Assessment of bone density using ultrasonic backscatter." Ultrasound Med Biol **24**(5): 689-95.

Wear, K. A., Laib, A., Stuber, A. P., et al. (2005). "Comparison of measurements of phase velocity in human calcaneus to Biot theory." J Acoust Soc Am **117**(5): 3319-24.

Williams, J. L. (1992). "Ultrasonic wave propagation in cancellous and cortical bone: prediction of some experimental results by Biot's theory." J Acoust Soc Am **91**(2): 1106-12.

Wu, C., Gluer, C., Lu, Y., et al. (1998). "Ultrasound characterization of bone demineralization." Calcif Tissue Int **62**(2): 133-9.

Ye, S., Wu, J. and Peach, J. (2000). "Ultrasound shear wave imaging for bone." Ultrasound Med Biol **26**(5): 833-7.

Yi, Z. and Greenleaf, J. F. (1999). "Stable and unbiased flow turbulence estimation from pulse echo ultrasound." Ultrasonics, Ferroelectrics and Frequency Control, IEEE Transactions on **46**(5): 1074-1087.

Zwikker, C. and Kosten, C. W. (1949). Sound Absorbing Materials. New York, Elsevier.

VITAE

Peiying Liu was born in Chengdu, People's Republic of China, on June 4, 1982, the daughter of Ling Huang and Qiao Liu. After completing her high school education at Wenjiang Middle School, Chengdu, P. R. China in 1999, she entered the University of Electronic Science and Technology of China at Chengdu, P. R. China. She received the degree of Bachelor of Science with a major in Communication Engineering from the University of Electronic Science and Technology of China in June, 2003. During the following year she attended St. Cloud State University, St. Cloud, Minnesota. In August, 2004 she entered the Graduate School of Biomedical Sciences at the University of Texas Southwestern Medical Center at Dallas. She spent four years of her education working on this dissertation and other projects, and was awarded the degree of Doctor of Philosophy in May, 2008.

Permanent Address: Mancaoyuan B-4-1, North Fengxidadao, Wenjiang
Chengdu, P. R. China 611130